High-Sensitivity Superconducting Detectors for Far-Infrared Space Astrophysics

Thesis by
Logan Michael Foote

In Partial Fulfillment of the Requirements for the
Degree of
Doctor of Philosophy

CALIFORNIA INSTITUTE OF TECHNOLOGY
Pasadena, California

2026
Defended July 1, 2025

Logan Michael Foote
ORCID: 0000-0002-4162-8609

ACKNOWLEDGEMENTS

The work presented in this thesis would not have been possible without the contributions of many researchers. I am deeply grateful for all who contributed their time, expertise, and support. First, I want to express my gratitude to my advisor Jonas Zmuidzinas, for providing me with the opportunity to push the sensitivity limits of KIDs. I am especially grateful for our countless hours of conversations about my research, and for the numerous occasions where he helped me find the path through seemingly impossible problems. Jonas' high standards taught me to never compromise on the quality of my work, and his intelligence continues to inspire those who work with him.

I was fortunate to be supported by several exceptional mentors at JPL. I want to thank Matt Bradford for inviting me to join the BLISS collaboration when I first came to Caltech, and for serving as my primary mentor at JPL over the last five years. Matt devoted hours each week to meeting with me and discussing my research. I am inspired by his persistence to track down the answer to the most difficult questions. I also want to thank Hien Nguyen, for providing invaluable mentorship through this period. I frequently think back to how lucky I was to spend so many hours in the lab with Matt and Hien during my first two years at Caltech. I learned how to approach problem-solving in the lab and I always enjoyed our long lunch conversations about physics and astronomy. I also appreciate the opportunity Hien provided me to teach astronomical instrumentation during the summer in Vietnam. Designing the course was intellectually rewarding and fun.

I would like to thank everyone who contributed to PRIMA, whose efforts fostered a supportive and highly capable team. I am especially grateful to Pierre Echternach, for always being on call to help debug fridge issues; to Peter Day, for helpful discussions on KID physics and measurement principles; to Byeong Ho Eom, for managing the Day lab test setup and for always being available to lend a hand; to Reinier Janssen and Steve Hailey-Dunsheath, for answering my many questions about KID design and physics; to our excellent fabrication team, and in particular Rick Leduc and Andrew Beyer; to the SRON team, who have performed many critical pioneering measurements on which our work relies; to the Goddard team, whose excellent work on Si microlens arrays and readout was critical to the success of PRIMA; to Elijah Kane and Chris Albert, for their helpful conversations and hard work in the lab; and to the many scientists, postdocs, and graduate students not

mentioned by name who contributed to the work presented in this thesis.

I am also thankful for my mentors, family, and friends in my personal life who have supported me through this process and who inspire me to strive for excellence in both research and life. I want to thank Peter Lloyd, for keeping me focused on what truly matters and for reminding me of the power of discipline. I am grateful for the endless support and encouragement from my father – I hope to live up to the example he sets. Finally, and most of all, I want to thank my partner Anna for her unwavering encouragement and kindness. She continues to inspire everyone lucky enough to know her.

ABSTRACT

The far-IR is a notoriously difficult portion of the electromagnetic spectrum to observe, but offers enormous discovery potential in astrophysics due to the orders-of-magnitude lower dust extinction compared to visible wavelengths. Astronomical background limited observations in the far-IR require a 4 K telescope in space with highly-sensitive detectors. These detectors must have a high multiplex factor and low hardware complexity to be deployed in sufficient numbers in space. Thus, large arrays of high-sensitivity far-IR detectors have been a long sought-after technology for astrophysicists.

Superconducting detectors are the clear choice for far-IR measurements, because semiconducting detectors become band-gap limited – and therefore cannot achieve the required sensitivities – at these wavelengths. Furthermore, far-IR semiconducting detectors are not scalable to large enough arrays. Transition Edge Sensors (TESs) were a potential candidate because, in theory, they could achieve the required sensitivities. However, decades of research on high-sensitivity TESs have not yielded successful results, and TESs also require significant hardware complexity which is difficult to implement in space. Kinetic Inductance Detectors (KIDs) were invented to reduce this hardware complexity, as thousands of KIDs can be read out on a single line with standard commercially available RF electronics. KIDs have surpassed the sensitivity requirement for far-IR space spectroscopy.

This thesis presents the culmination of high-sensitivity far-IR TES development at the Jet Propulsion Laboratory (JPL) and Caltech, followed by the initial development of high-sensitivity far-IR KIDs. These KIDs were able to surpass the sensitivity requirement for far-IR spectroscopy, and offer a definitive path forward for deployment in space. Following this achievement, the Probe Far-Infrared Mission for Astrophysics (PRIMA), a far-IR probe-class space telescope which will deploy these KIDs, was selected by NASA for a phase A study. This thesis describes the development of these KIDs, as well as future demonstrations that must be accomplished for successful deployment on PRIMA.

PUBLISHED CONTENT AND CONTRIBUTIONS

[1] Logan Foote et al. "High-Sensitivity Kinetic Inductance Detector Arrays for the Probe Far-Infrared Mission for Astrophysics". en. In: *Journal of Low Temperature Physics* 214.3-4 (Feb. 2024), pp. 219–229. ISSN: 0022-2291, 1573-7357. DOI: 10.1007/s10909-023-03041-6. URL: https://link.springer.com/10.1007/s10909-023-03041-6 (visited on 04/12/2024).
The main contents of the work has been reprinted here with minimal changes, except one step of the analysis, which is described in the text. L.M.F wrote the manuscript and performed measurements and analysis.

[2] Logan Foote et al. "Highly sensitive far-IR KIDs for PRIMA: optical characterization of a 25-micron array". In: *Millimeter, Submillimeter, and Far-Infrared Detectors and Instrumentation for Astronomy XII*. Ed. by Jonas Zmuidzinas and Jian-Rong Gao. Yokohama, Japan: SPIE, Aug. 2024, p. 27. ISBN: 978-1-5106-7527-8 978-1-5106-7528-5. DOI: 10.1117/12.3020228. URL: https://www.spiedigitallibrary.org/conference-proceedings-of-spie/13102/3020228/Highly-sensitive-far-IR-KIDs-for-PRIMA--optical-characterization/10.1117/12.3020228.full (visited on 04/15/2025).
The main contents of the work has been reprinted here with minimal changes. L.M.F wrote the manuscript and performed measurements and analysis.

[3] Logan Foote et al. "High-sensitivity transition-edge-sensed bolometers: Improved speed and characterization with AC and DC bias". In: *Journal of Applied Physics* 134.9 (Sept. 2023), p. 094503. ISSN: 0021-8979. DOI: 10.1063/5.0157208. URL: https://doi.org/10.1063/5.0157208 (visited on 08/19/2024).
The entire work has been reprinted here with minimal changes. L.M.F wrote the manuscript and performed measurements and analysis.

TABLE OF CONTENTS

Acknowledgements . . . iii
Abstract . . . v
Published Content and Contributions . . . vi
Table of Contents . . . vi
Chapter I: Unveiling Dust-Obscured Galaxies . . . 1
1.1 Dust . . . 2
1.2 Star Formation . . . 4
1.3 Black Hole Accretion . . . 6
1.4 Far-IR Spectroscopy . . . 8
1.5 Technological Challenges of Far-IR Observations . . . 9
1.6 A Brief History of Far-IR Spectroscopy . . . 12
1.7 Far-IR Superconducting Detectors . . . 15
1.8 Thesis Overview . . . 17
Chapter II: High-Sensitivity Far-Infrared Detectors . . . 28
2.1 Photon Noise . . . 28
2.2 Detector Requirements . . . 29
2.3 Transition Edge Sensors: Operation and Noise . . . 31
2.4 Kinetic Inductance Detectors: Operation and Noise . . . 34
Chapter III: Transition Edge Sensors for Far-Infrared Space Astrophysics . . . 63
3.1 Introduction . . . 63
3.2 Array Design and Fabrication . . . 64
3.3 Experimental Setup . . . 66
3.4 AC Measurements . . . 70
3.5 DC Measurements . . . 75
3.6 Summary . . . 79
Chapter IV: Kinetic Inductance Detectors for Far-Infrared Space Astrophysics 83
4.1 Introduction . . . 83
4.2 Design . . . 84
4.3 Challenges of Low-Volume Al . . . 92
4.4 Experimental Setup . . . 95
4.5 Results . . . 98
Chapter V: Summary and Discussion . . . 128
Appendix A: Telescope Sensitivity Calculation . . . 132
Appendix B: Kinetic Inductance Detector Resonators . . . 134
B.1 Fitting . . . 138
Appendix C: Fabrication Optimization . . . 144
Appendix D: Correlated Noise Removal Algorithm . . . 146
Appendix E: Tuning . . . 150
E.1 Tuning at High Absorbed Power . . . 151

Chapter 1

UNVEILING DUST-OBSCURED GALAXIES

Half of the starlight in our universe is shrouded by clouds of gas and dust. Figure 1.1 is a visible and near-infrared (near-IR) composite image of Barnard-68. What appears to be a hollow void is, in reality, a dusty foreground cloud which obscures thousands of Milky Way stars. Barnard-68 is a small, albeit striking, example of a molecular cloud, named for its primary component: molecular hydrogen shielded from photodissociation by dust. Molecular clouds range in size from a few solar masses (Bok globules, such as Barnard-68) to tens of millions of solar masses (giant molecular clouds, or GMCs).[50] Molecular hydrogen does not easily radiate, so alternate tracers such as CO are often used to image molecular clouds.[29] The pervasiveness of molecular clouds in our Milky Way galaxy is demonstrated by the fractal structure of CO emissions in Figure 1.2.

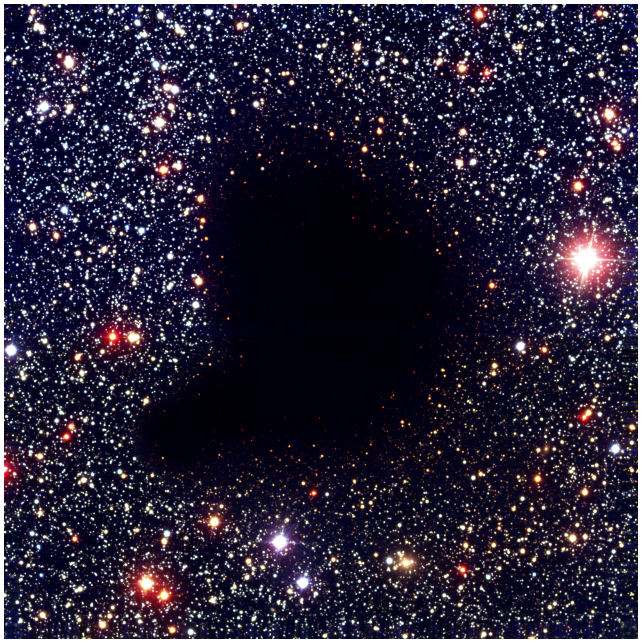

Figure 1.1: A composite visible and near-IR image of Barnard-68, a molecular cloud within the Milky Way galaxy, observed with the 8.2-m VLT ANTU telescope and the multimode FORS1 instrument. Image was released by the European Southern Observatory.[32]

Typical molecular clouds consist of 70% H, 28% He, and 2% heavier elements

by mass, where about half of the heavier elements take the form of dust grains.[35] Although dust is a small percentage of molecular cloud mass, it is responsible for most of the clouds' absorption of nearby starlight.[12] When a portion of a molecular cloud reaches a critical mass, it will collapse under gravity until fusion begins, forming a star. Portions of the cloud will form into protostars, which will eventually turn into stars, and some material will remain in protoplanetary disks surrounding the star to eventually form planets.[54] Measurements of the properties of molecular clouds, star-forming regions, and protoplanetary disks are crucial for unraveling the history of star and planet formation.

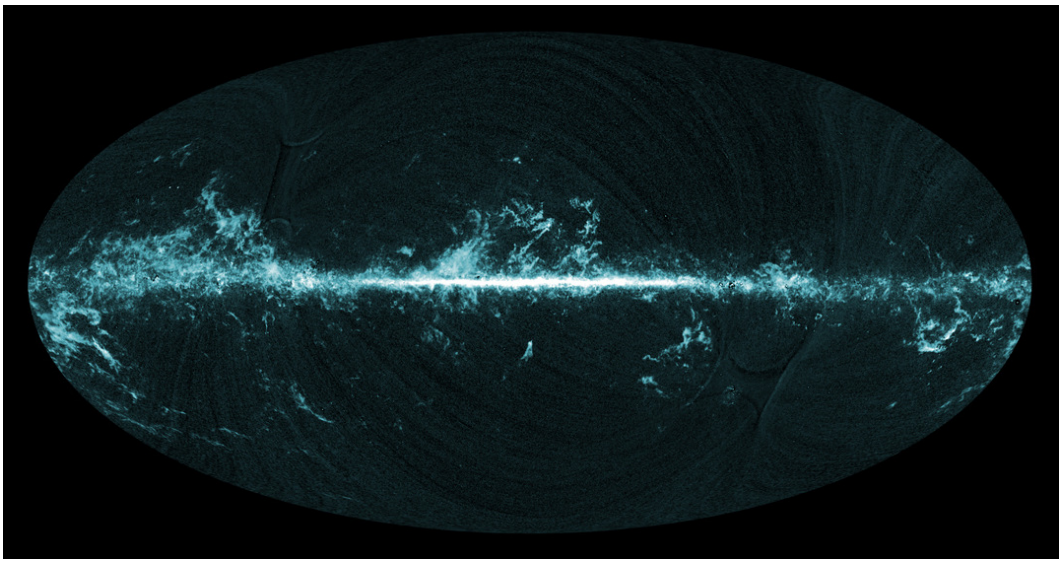

Figure 1.2: All-sky map of CO emissions, as seen by Planck. Image was released by the ESA/NASA/Planck Collaboration.[18]

1.1 Dust

Dust refers to particles of matter with sizes ranging from large molecules containing tens of atoms to µm-scale grains, primarily consisting of amorphous silicate and carbonaceous grains.[14] The universe is filled with highly dust-obscured galaxies.[45] The majority of star formation out to $z \sim 4$ is obscured by dust,[61] and observations from the James Webb Space Telescope (JWST)[75] and the Atacama Large Millimeter Array (ALMA)[65,34] find highly dust-obscured galaxies earlier than a few hundred million years after the Big Bang (z >6). Dust is formed primarily in supernovae and the atmospheres of asymptotic giant branch stars, and subsequently reprocessed in the ISM through a variety processes.[61] Although dust makes up only 1% of the

matter in typical molecular clouds, it plays a significant role in the radiative and chemical environment of galaxies. A key property of extinction due to dust is its wavelength dependence: extinction sharply decreases with increasing wavelength. Figure 1.3 is a plot of the ratio of optical depth τ_λ to the optical depth in the visible band τ_V versus wavelength along diffuse Galactic sightlines. Compared to the visible band, the optical depth is a factor of 5×10^{-3} lower at 50 μm and 3×10^{-4} at 200 μm. The far-IR is thus a powerful tool for observing regions that are obscured by dust at shorter wavelengths.

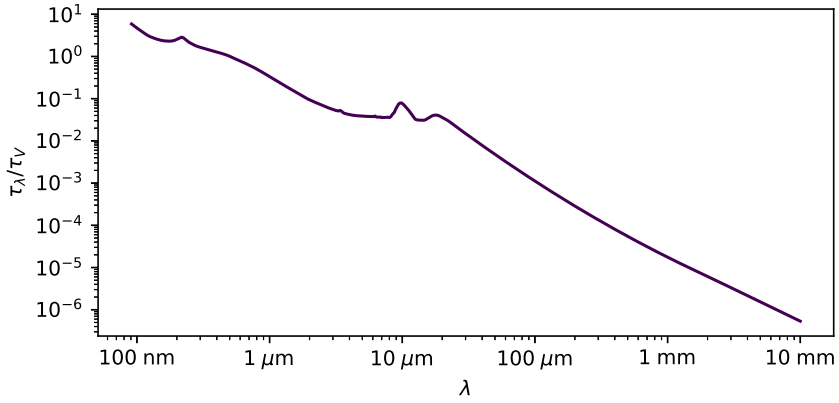

Figure 1.3: Ratio of the optical depth τ_λ to the optical depth in the visible band τ_V versus wavelength along diffuse Galactic sightlines. The data in this plot are compiled in Hensley & Draine 2021.[27]

Most of the energy that is absorbed by dust at near-IR to X-ray wavelengths is re-emitted thermally in the far-IR. In fact, about half of all radiation from stars has been absorbed by dust and re-emitted in the far-IR: the thermal far-IR emissions from dust produce a far-IR cosmic background of the same intensity as the near-IR/optical background from starlight, as shown in Figure 1.4.

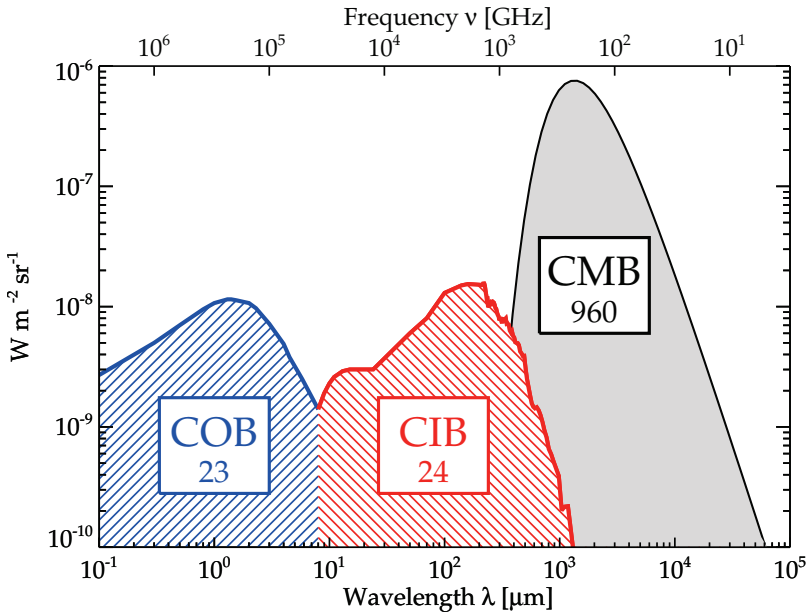

Figure 1.4: Cosmic background intensity versus wavelength, with their approximate brightness in $\mathrm{nWm^{-2}sr^{-1}}$ written in the boxes. The backgrounds are (from left to right): the Cosmic Optical Background (COB), the Cosmic Infrared Background (CIB), and the Cosmic Microwave Background (CMB). From Dole et al. 2006.[12]

Dust formation is an essential component of planet formation: heavy elements ("metals") that are produced by stars and supernovae form dust grains before clumping together in protoplanetary disks to form planets. Far-IR spectroscopy provides two probes of this process. First, ratios of abundances of elements such as N, O, and C are used to determine the metallicity of galaxies. N, O, and C have far-IR fine-structure lines that can be used to probe their abundances. Second, the mass fraction of the smallest dust grains, called polycyclic aromatic hydrocarbons (PAHs), can be traced by comparing PAH spectral features to the dust continuum. These spectral features are bright: PAHs can contribute up to 25% of the IR luminosity of galaxies.[63] The coevolution of metals and dust can be studied by measuring both metallicites and PAH features in the same galaxy samples using far-IR spectroscopy.

1.2 Star Formation

Regions of molecular clouds can collapse to form stars. The collapse may happen naturally due to random fluctuations of density within the cloud, or it may be triggered by an outside influence, such as collisions with other clouds, a supernova, or a shock wave due to outflows from a black hole.[68] In the regions surrounding newly forming stars, gas in the parent cloud is ionized by radiation from the stars.

The region in between the molecular cloud and fully ionized gas is known as the photodissociation region (PDR): molecules are photodissociated and some atomic ions are found. Figure 1.5 is an annotated image of a PDR from JWST. Atomic ions in PDRs produce a variety spectral lines, and the wavelength dependence of dust extinction allows far-IR radiation to escape. The far-IR band therefore offers an excellent opportunity for probing star-forming regions.

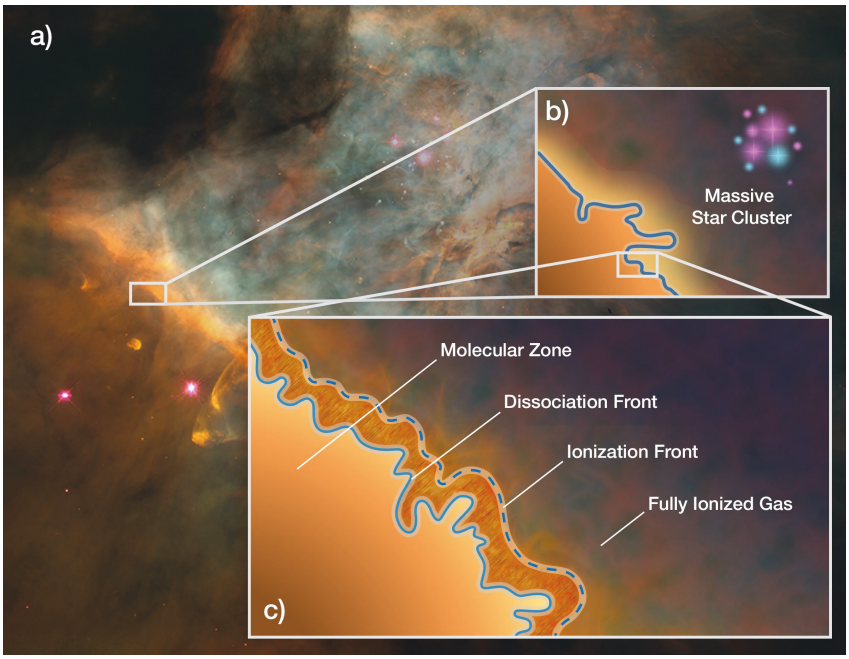

Figure 1.5: Anatomy of a PDR as seen by JWST. (a) image of a PDR within the Orion nebula. (b) diagram depicting the location of the massive cluster of newly forming stars relative to the PDR. (c) annotated diagram of the molecular zone, PDR, and region of fully ionized gas. Image was released by NASA.[1]

The history of star formation over cosmic time is traced by the star formation rate density (SFRD), or the mass of stars formed per time per comoving volume. Observations indicate the SFRD began rising about a billion years after the Big Bang, peaked when the Universe was less than one fourth its current age, and has been declining ever since.[44] A complete understanding of star formation includes the history of the SFRD and its correlation with other important parameters, such as metallicity, stellar mass, and black hole accretion. O and B stars are often used as tracers of star formation because they are short-lived. Integrating UV radiation from individual galaxies of known redshift can be used to measure the SFRD. However, UV radiation is often heavily obscured by the dusty regions surrounding O and B stars. Alternatively, far-IR dust emissions can be used to trace the SFRD. Figure 1.6

is a plot of the SFRD versus redshift using both UV and far-IR observations, without corrections for dust extinction. At $z < 2$, the UV observations recover a lower SFRD than the far-IR data due to extinction. The data show an SFRD that increases after the big bang and peaks around $z = 2$. The far-IR data are not complete at $z > 2$, and are mostly lower bounds.

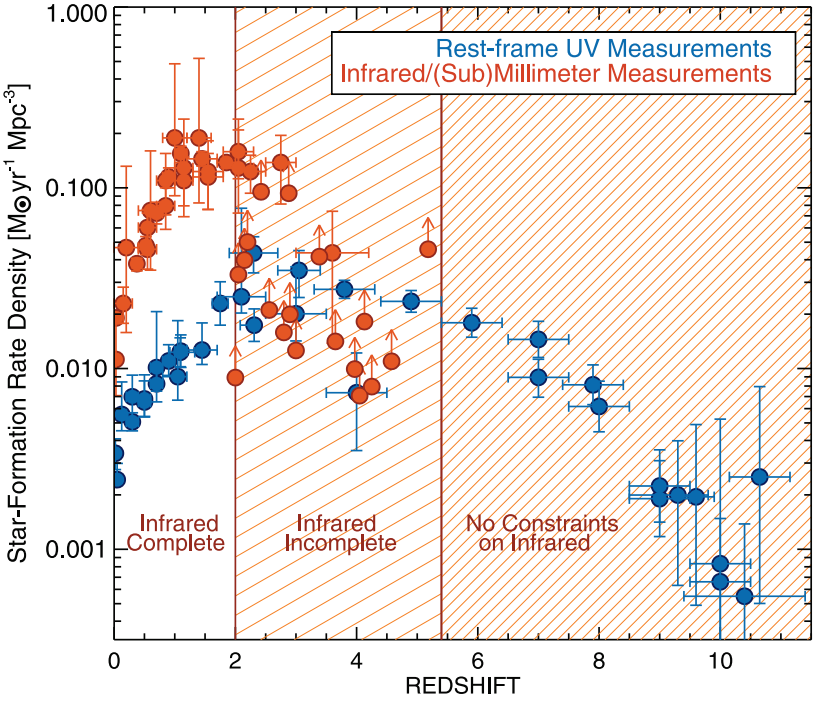

Figure 1.6: Compilation of measurements of the SFRD versus redshift using integrated far-IR and UV radiation. IR measurements are separated into three categories: "Infrared Complete" at low redshifts provide upper and lower bounds on the SFRD, "Infrared Incomplete" at intermediate redshifts provide mostly lower bounds on the SFRD, and "No Constraints on Infrared" have no infrared measurements. From Casey et al. 2018.[5]

1.3 Black Hole Accretion

In addition to star formation, the history of accretion of matter onto supermassive black holes (SMBHs) is a crucial piece of the history of galaxy evolution. Active galactic nuclei (AGN) are SMBHs surrounded by optically-thick accretion disks with a range of temperatures that produce UV and optical thermal emission.[30] The dusty torus surrounding the SMBH provides significant angle-dependent extinction. The history of black hole growth is quantified by the black hole accretion rate density (BHARD), the mass accreted onto a black hole per time per comoving volume. Due to the small size of AGN compared to the host galaxy and the difficulty in

measuring obscured emission, the BHARD has not been measured as definitively as the SFRD.[30]

Many observations of the black hole accretion rate (BHAR) in individual galaxies using X-rays and UV radiation have been performed, generally tracing out a similar history to the star formation rate (SFR).[30] These studies are limited in scope and have significant uncertainty, and there is considerable disagreement between the various observations. Far-IR spectroscopy can measure AGN properties through identification of spectral lines from species that are ionized by UV and X-ray radiation produced by the accretion disk, such as Ne[V], O[IV], Si[IX], and Mg[VIII]. A larger sample of galaxies with the BHARD measured in the far-IR could resolve the UV/X-ray observation disagreements.

In the nearby universe, SMBH mass and galaxy mass are highly correlated.[58] However, black hole growth and star formation occur on vastly different scales, and the correlation between the two is difficult to determine using current observations because the population of galaxies for which the SFR and BHAR are currently measured with UV and X-ray radiation do not overlap significantly. Far-IR spectroscopic measurements can obtain the SFR and BHAR of galaxies to create the large statistical sample that will be required to unravel this history, with the goal of distinguishing between competing galaxy evolution models which show a factor of 10 disagreement in the BHARD / SFRD distribution.[25]

An active area of research is the feedback processes which regulate black hole growth and star formation. AGN-driven outflows are an internal negative-feedback process for star formation suppression which can provide a connection between the SFR and BHAR, but better observations of outflow properties are needed.[73] Far-IR absorption in the blueshifted wings of molecular lines with high dipole moments and emission line wings of fine structure lines of ionized gas can be converted to outflow rates to provide constraints on outflow models.[23] In addition to outflows, AGN produce jets of charged particles at high speeds which shock and heat surrounding gas to temperatures of 500-1,000 K, producing far-IR lines from the rotational transitions of H_2.[23] These far-IR probes of feedback mechanisms will be a valuable addition to our understanding of galaxy evolution.

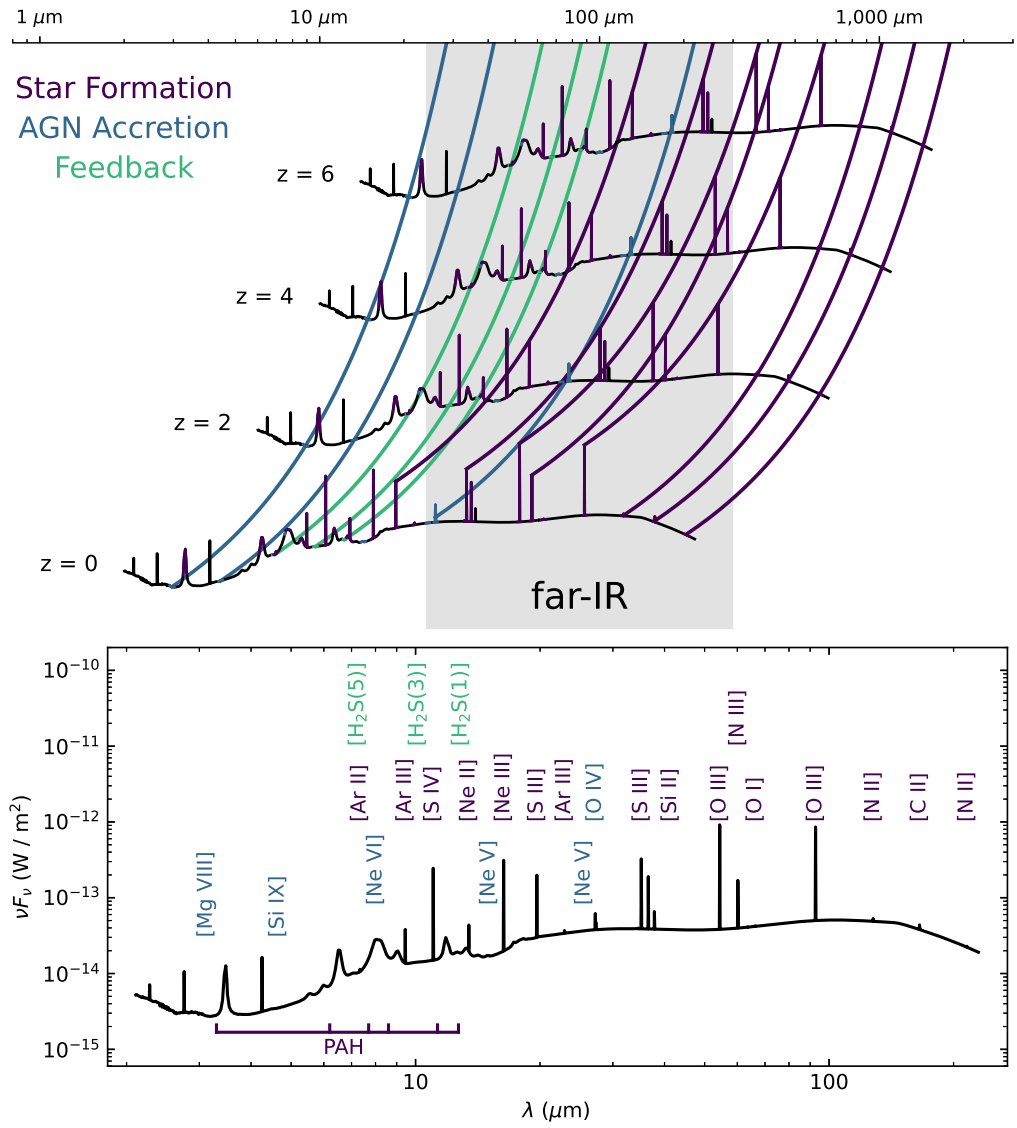

Figure 1.7: (Top) Simulated spectra versus redshift for a galaxy with moderate star forming activity. Some tracers of star formation (purple), AGN accretion (blue), and AGN feedback (green) are available in far-IR band at a wide range of redshifts, but particularly around cosmic noon. (Bottom) Some common far-IR spectral lines. Colors correspond to the same processes as the top plot. Model spectra are provided by PRIMA co-I Denis Burgarella, based on models from the Code Investigating GALaxy Emission (CIGALE).[6]

1.4 Far-IR Spectroscopy

Far-IR spectra can be used to probe the SFR, BHAR, metallicity, dust content, and feedback simultaneously in the same galaxy sample. Additionally, spectroscopy can be used to recover redshifts and spatial confusion is reduced by distinguishing galaxies that are overlapping on the sky (within the angular resolution of the telescope)

but separated in redshift.

The abundances of atomic ions can determine the amount of radiation that is present at ionizing wavelengths. For example, UV and X-ray emission from AGN can ionize atoms with high ionization energies (> 25 eV), UV emission from massive stars can ionize atoms with ionization energies on the order of 10 eV, and ions of atoms with lower ionization energies can be found in PDRs. Many of these ions have far-IR fine-structure lines that can be used to probe the regions in which they are produced. Prominent far-IR spectral lines over a range of redshifts are plotted in Figure 1.7. Within the far-IR band (as observed from Earth), tracers of the SFRD, BHARD, metallicity, dust content, and feedback are present across a wide range of redshifts, and particularly around cosmic noon. Observations of these spectral lines over a range of redshifts will enable enormous discovery in the field of galaxy evolution.

1.5 Technological Challenges of Far-IR Observations

Atmospheric transmission presents a fundamental obstacle for ground-based far-IR observations. Atmospheric transmission from a superior ground-based site with 1 mm precipitable water vapor is plotted in Figure 1.8. ALMA can observe in the transmission windows at mm and sub-mm wavelengths, and achieves high sensitivity and resolution through use of an array of 66 widely-spaced 12 m telescopes with a large total collecting area, which is only practical with a ground-based observatory.[33] Near-IR and mid-IR observations are possible from the ground in select transmission windows, though a large improvement in sensitivity is possible using a space observatory, e.g. JWST. Far-IR spectroscopy is impossible from the ground due to the lack of transmission windows. Far-IR observations have been made using airborne and balloon-borne telescopes, but thermal emission from the atmosphere and telescope sets a limit to the sensitivity.

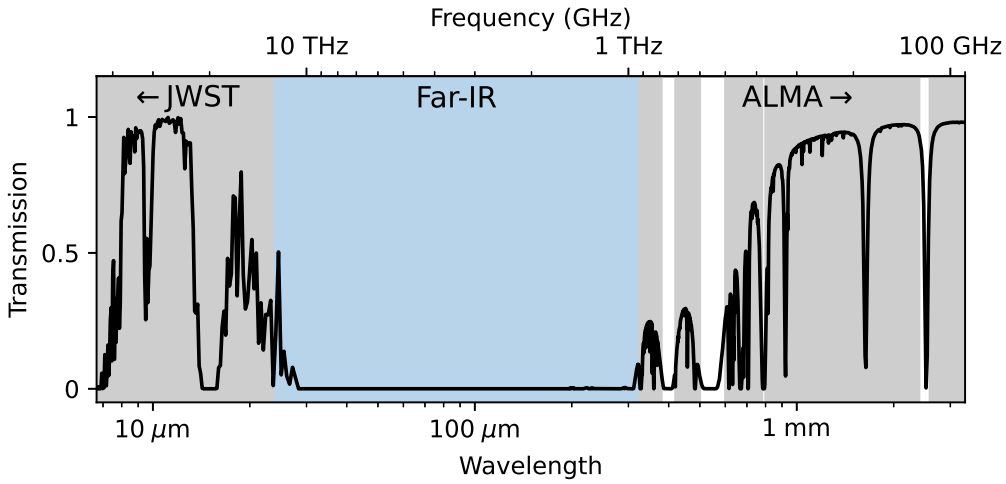

Figure 1.8: Atmospheric transmission versus wavelength from an ALMA-like site with 1 mm precipitable water vapor. The measurement bands for spectroscopy with JWST and ALMA are shaded gray. The far-IR gap is shaded blue, where the atmospheric transmission is near zero. The mm and sub-mm data was generated by Simon Radford using the Atmospheric Transmission at Microwaves model.[53] The mid-IR data was generated using the Reference Forward Model[15] by PRIMA Deputy Project Scientist Klaus Pontoppidan.[55]

Graybody emission spectra from ~10-300 K objects peak in the far-IR. Instrument sensitivity is therefore maximized through use of a cold telescope in space. Figure 1.9 is a plot of the sum of the astronomical and telescope backgrounds for a range of telescope temperatures from 4 K to 270 K. In the far-IR band, only a 4 K telescope allows for background-limited measurements. Shorter wavelength telescopes, such as JWST, can operate at higher temperatures without surpassing the astronomical background.

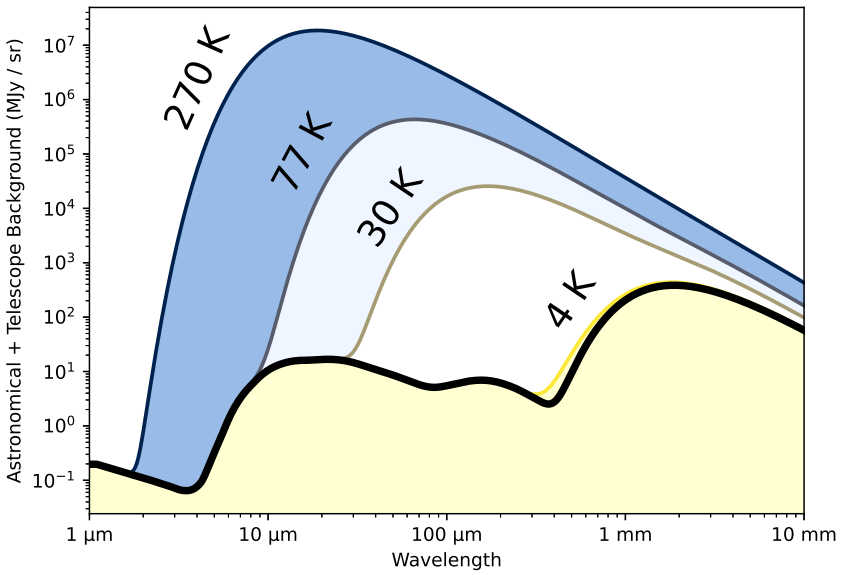

Figure 1.9: Sum of the astronomical and telescope backgrounds versus wavelength for telescope temperatures ranging from 4 K to room temperature with 5% emissivity. The astronomical background measurement corresponds to the annual average background toward the north ecliptic pole as viewed from an Earth-Sun L2 orbit, similar to that in Benford et al. 2004[3] (see Appendix A).

Even with a 4 K telescope in space, far-IR observatories face another major technological challenge: detectors must achieve high sensitivity to take advantage of the low background. Unlike detectors at shorter wavelengths, far-IR detectors have not benefitted from commercial development. Figure 1.10 is a plot of the 5-σ 1-hour line sensitivities for previous, current, and future missions. Typical spectra for a galaxy with moderate star formation at a resolution of $R = \lambda/\Delta\lambda = 100$ are plotted for redshifts of $z = 0.5$ and $z = 3$. JWST is able to achieve high-sensitivity at shorter wavelengths with semiconducting detectors, but semiconductor detector technology is not well-developed at > 25 µm.[19] JWST loses sensitivity as it approaches the longest wavelengths due to the telescope temperature and the detector sensitivity. The sensitivity of the 3.5 m Herschel Space Observatory was limited by its 80 K telescope and the detector technology available at that time. The Spitzer Space Telescope used a 0.85 m telescope cooled to 5 K and performed photometric observations at wavelengths out to 160 µm.[59] ALMA is able to achieve high sensitivity at longer wavelengths using the coherent detection technique with a large collecting area. However, coherent detection loses sensitivity at shorter wavelengths,[78] and the large collecting area is not practical in space. Detector sensitivity is quantified by the Noise Equivalent Power (NEP): the signal power required to achieve a signal-to-

noise ratio of 1 in a 1 Hz bandwidth. The photon NEP (the NEP due to the random arrival rate of photons) corresponding to the 4 K telescope background in Figure 1.9 ranges from $1 - 1.8 \times 10^{-19}$ W/$\sqrt{\text{Hz}}$ for $R = 100$, so the required detector NEP for background-limited far-IR observations is typically set to 1×10^{-19} W/$\sqrt{\text{Hz}}$ or better.

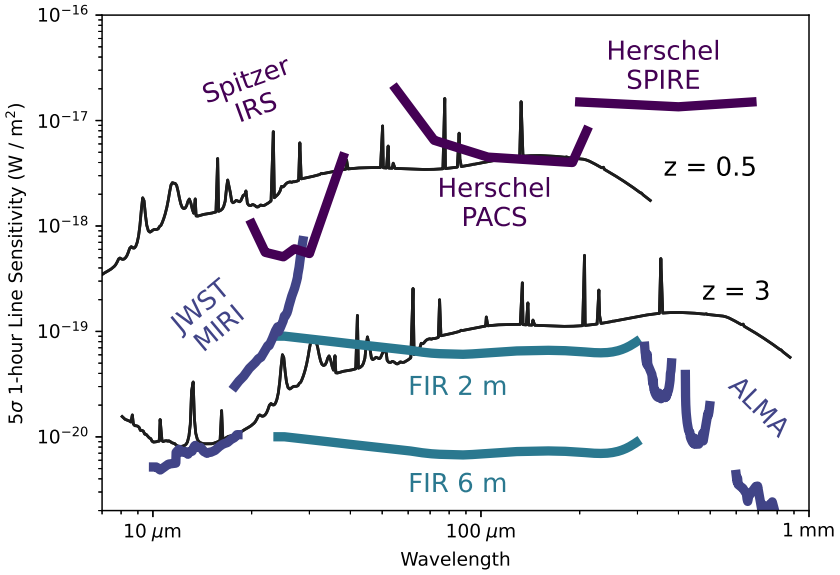

Figure 1.10: 5-sigma 1-hour line sensitivities for previous, current, and future missions. The spectra are simulated for a moderate star-forming galaxy as observed by an R = 100 spectrometer, and correspond to the data in Figure 1.7. The curves labelled "FIR" are sensitivity projections for a 4 K telescope in space with detector NEPs of 1×10^{-19} W/$\sqrt{\text{Hz}}$ and the labelled mirror diameters. The sensitivity calculation is outlined in Appendix A. Instrument sensitivities have been compiled (by C.M. Bradford) from the latest available information for each instrument's as-achieved sensitivity. Sensitivities to line flux assume an R=1,000 (300 km/s) line width where applicable.

1.6 A Brief History of Far-IR Spectroscopy

Far-IR astrophysics has historically suffered from technological difficulties: pioneering practitioners Dirk Muehlner and Rainer Weiss stated "[The far-IR] is a miserable region of the electromagnetic spectrum in which to carry out experiments. The technology of far-IR detection is in a primitive state; furthermore, even if this situation is eventually improved, any background measurements in this region are complicated by the inevitable radiation from sources that are at temperatures considerably higher than 3 K".[49] Hints to the existence and origin of the far-IR background had been present as early as 1930, when Robert Trumpler discussed the role of dust in visible

light obscuration. Trumpler compared the distance to various star clusters using two methods: apparent magnitudes and angular diameters.[72] The apparent magnitude is affected by obscuration, while the angular diameter is not. Trumpler concluded that Rayleigh scattering of radiation by free atoms was not enough to account for the discrepancy, so larger dust particles must play a significant role in obscuration. Thirty years later, the invention of the Germanium (Ge) bolometer by Frank Low enabled the first far-IR observations,[42] which eventually led to the discovery that these dust grains were re-emitting the absorbed energy in the far-IR. The first semiconducting bolometers were not very sensitive, so they were only suitable for the brightest objects. Low and others spent the next decade observing the moon, sun, and bright planets in the far-IR.[21] These early far-IR observations with Ge bolometers led to the prediction of the far-IR background.[43] For the next 40 years, far-IR semiconducting detectors matured and saw light on ground, upper-atmosphere, and space missions. In the 1970s, the Lear Jet Observatory brought Ge bolometers to the upper atmosphere and observed the bright galactic nuclei M82 and NGC 253.[26] At this time, it became clear that the far-IR emission was primarily from dust grains. Shortly after, Muehlner and Weiss set an upper limit on the far-IR background with observations from a balloon.[49]

Far-IR astronomy took a big step forward in the 1990s-2000s with the Infrared Astronomical Satellite (IRAS),[36] the Infrared Space Observatory (ISO),[31] the Cosmic Background Explorer (COBE),[9] and the Herschel Space Observatory.[28] These observations included a full sky survey with IRAS, the conclusive discovery of the far-IR background with COBE, and a large survey of far-IR galaxies with Herschel. IRAS detected 350,000 sources using an array of 62 semiconducting detectors at 12-100 μm.[36] While IRAS detected far-IR radiation from a number of bright galaxies, it was not sensitive enough to measure the far-IR background. Around the same time, COBE was observing the Cosmic Microwave Background (CMB). COBE was sensitive enough down to 100 μm to conclusively measure the far-IR background.[57] While IRAS and COBE made important contributions to our understanding of the far-IR background, it was clear that a dedicated mission with state-of-the-art semiconducting detectors was the next step for astrophysics. Over the next decade, the Herschel space telescope was built and deployed. Herschel deployed state-of-the-art Ge bolometers on its Spectral and Photometric Imaging Receiver (SPIRE) instrument. Herschel's observations showed that the sky is full of galaxies that are bright in the far-IR, mostly at $z = 1-3$, and provided the best photometric measurements of far-IR galaxies to date.[45] In combination with studies at other wavelengths, Herschel

Mission	Platform	Comments
OLIMPO (2018)	• balloon • KIDs • 1.6 K optics	• 580-2,000 µm, spectroscopy • measurements of the Sunyaev-Zeldovich effect • first successful operation of KIDs on a balloon[56]
SOFIA-HAWC+ (2010-2022)	• aircraft • TESs • warm optics	• 50-240 µm, polarimetric imaging[64] • local fine-structure line mapping, magnetic field maps with polarimetry • set a precedent for upper-atmosphere far-IR observations with superconducting detectors
BLAST-TNG (2020)	• balloon • KIDs • warm and 4 K optics	• 250-500 µm, polarimetric imaging[8] • KIDs were read out successfully, but instrument was damaged during flight, so no useful science data was collected
EXCLAIM (future)	• balloon • KIDs • 1.7 K optics	• 420-540 µm, spectroscopy[52] • CO and CII intensity mapping
TIM (future)	• balloon • KIDs • warm optics	• 240-420 µm, spectroscopy[46] • CII, NII, OI, OIII line intensity mapping[74] • KIDs are similar to those that could be used in space, but with higher volume[41,37]

Table 1.1: Past and upcoming upper-atmosphere far-IR missions that use superconducting detectors.

data has contributed substantially our knowledge of the history of galaxy evolution.

Though Herschel was able to survey many galaxies in the far-IR, it suffered from significant source confusion, where multiple galaxies were too closely separated to be distinguished given the angular resolution of the telescope. In the early 2000s, some mission concepts were proposed for far-IR interferometers, which would have high angular resolution to overcome confusion. The Submillimeter Probe of the Evolution of Cosmic Structure (SPECS) was a 1 km interferometer concept that envisioned three formation-flying space telescopes.[40] SPECS would provide angu-

lar resolution at the level of the Hubble Space Telescope, but the technological challenges and cost were far too extravagant for a next far-IR mission. Spectroscopy with a cryogenic telescope was identified as a path for overcoming confusion while simultaneously providing a rich dataset for galaxy evolution. Enthusiasm for far-IR spectroscopy was building since the 2000 decadal survey suggested development of a next-generation far-IR space telescope.[51] The next two decades saw the development of several mission concepts.[77,47,22] One mission received significant attention: the Space Infrared Telescope for Cosmology and Astrophysics (SPICA) was a collaboration between ESA and JAXA that would deploy arrays of superconducting detectors on 2.5 m telescope cooled to 8 K.[66] SPICA was seen as an economical path to significant discovery in the far-IR and was selected as a finalist for the ESA Medium Class-5 mission competition in 2018, but ultimately did not secure funding in 2020. My graduate research work began with high-sensitivity Transition Edge Sensed (TES) bolometer development as an offshoot project from SPICA, as detailed in Chapter 3.

In the 2010s and 2020s, several upper-atmosphere projects were (or will be) deployed to target various science objectives and provide opportunities for important technological development, though they suffer from an atmospheric loading that results in more than a two order-of-magnitude degradation in sensitivity compared to space. Despite this limitation, demonstrations of remote superconducting detector readout and cold optics with far-IR detectors will provide valuable data for an upcoming far-IR space telescope. Past and future far-IR upper-atmosphere projects that use superconducting detectors are outlined in Table 1.1.

1.7 Far-IR Superconducting Detectors

Until recently, the most commonly used far-IR detectors were semiconducting. For nearly 50 years, the far-IR was observed with exponentially improving sensitivity as semiconducting detectors reached maturity.[47] However, multiplexing semiconducting devices is challenging. Virtually all experiments had individually-wired pixels, which sets a practical limit to the array size of few hundred pixels. This technology culminated with the SPIRE instrument on the Herschel spacecraft.[24] The Z-Spec wideband millimeter-wave R~250 spectrometer for mountaintop sites is another example, requiring an NEP of 4×10^{-18} W/$\sqrt{\text{Hz}}$ with 160 pixels.[4]

In the mid 1990s, superconducting devices were developed with improved multiplexing capability and the potential for faster, more sensitive detector pixels. The leading

technology for many years has been voltage-biased TES bolometers. Both time-domain and frequency-domain multiplexing schemes have been developed,[13,48,70,76] and both use superconducting quantum interference devices (SQUIDs) as the first-stage amplifier. TESs are now the workhorse for many cosmology experiments (see Section 2.3), and have separately achieved excellent sensitivities targeting space-borne spectroscopy, as described in Chapter 3. The TES bolometer architecture, however, still requires complicated sub-Kelvin circuitry, multiple wire bonds per pixel, expensive SQUIDs, and ultimately does not support a large multiplex factor (number of pixels per wire pair). The BICEP Array receiver, for example, uses 1,800 wires to read out 12,324 detectors.[60] Additionally, as with all bolometers, TES sensors struggle to achieve sensitivity and speed requirements simultaneously, so devices designed for space-borne spectroscopy are slow.

In 1999, Kinetic Inductance Detectors (KIDs) were proposed as a path to higher multiplex factors and simpler cryogenic integration.[11] KIDs are described in detail in Section 2.4; the fundamental detection method is via photons breaking Cooper pairs in a superconducting film. By using narrowband resonators as detector pixels, frequency-domain multiplexing can be efficient, enabling multiplex factors of order 1,000. By eliminating the photon thermalization of bolometers, KIDs offer additional advantages of a higher operating temperature and insensitivity to photons below the pair-breaking energy. KIDs also offer excellent natural dynamic range. A major challenge for KIDs with respect to other options had been the device sensitivity, but, as described in Chapter 4, the required sensitivity has now been reached.

Another superconducting detector candidate is the Quantum Capacitance Detector (QCD), which also measures the effect of photons breaking Cooper pairs in a superconducting film, but via quasiparticle (QP) tunneling to a capacitive island rather than changes in the inductance. With its single-electron sensitivity, the QCD is exquisitely sensitive, and has demonstrated individual photon counting in the 200 μm range.[16,17,62] However, a fundamental challenge of the QCD is its dynamic range; the saturation of the tunneling rate means that the device loses response at high loadings, so it is difficult to engineer for practical astrophysics applications. A frontier area of research is a detector that combines QCD and KID detection with the same readout. QCD-KID hybrids would combine single-photon sensitivity with high dynamic range.

Table 1.2 is a table of the superconducting detector candidates for far-IR spec-

troscopy. With the sensitivity requirement now surpassed by KIDs, NASA has selected the PRobe far-Infrared Mission for Astrophysics (PRIMA) for a phase A study.[71] PRIMA will enable enormous scientific discovery space by providing the first far-IR spectroscopic observations on a cold telescope in space with highly-sensitive KIDs. The future of far-IR astrophysics is bright!

Name	Detection method	Best far-IR sensitivity
TES	• temperature of island • steep R versus T of film resistor	• 1×10^{-19} W/$\sqrt{\text{Hz}}$ with τ = 30 ms[38] • 8×10^{-19} W/$\sqrt{\text{Hz}}$ with τ = 3 ms[20]
KID	• photo-production of QPs from Cooper pairs • QP density in film sets surface impedance	• 4.6×10^{-20} W/$\sqrt{\text{Hz}}$ • 25 µm single-photon counting[10] • τ = 1 ms
QCD	• photo-production of QPs from Cooper pairs • tunneling of QPs to capacitive island	• 3×10^{-21} W/$\sqrt{\text{Hz}}$ • 200 µm single-photon counting[17]

Table 1.2: Superconducting detector candidates for far-IR spectroscopy with their detection method and best far-IR sensitivity. The reported TES best sensitivities include only devices with full optical characterization. Other high-sensitivity TES projects have reported NEP measurements without time constant measurements[2,67] or electrical NEP measurements without optical characterization.[39,69] A current area of research is the footprint reduction of high-sensitivity far-IR TESs using coherent phonon transport effects to reduce G without the requirement of long support legs.[7]

1.8 Thesis Overview

Following the introduction in Chapter 1, Chapter 2 is an overview of the operation and noise of TESs and KIDs, as well as a discussion on NEP optimization for low-background far-IR applications. Chapter 3 covers work on high-sensitivity far-IR TESs, wherein an attempt to meet the sensitivity and time constant requirements is described. The difficulties in achieving both requirements simultaneously are discussed. The devices achieved a sufficient time constant, but with an unacceptable degradation in sensitivity compared to previous devices with slower time constants. The development of a novel response calibration technique for frequency-domain multiplexed TES bolometers is also described. Chapter 4 covers work on high-sensitivity far-IR KIDs. The challenges of achieving high-sensitivity are discussed, as well as several KID designs that can cover the full PRIMA band. KIDs targeting

the short- and long-wavelength limits of the band were fabricated, and both exceed the sensitivity requirement for PRIMA. The short-wavelength design was also able to detect single 25 µm photons. Kilo-pixel arrays of the KIDs were fabricated, and array-level measurements are presented. Finally, measurements of and future plans to reduce correlated noise in the kilo-pixel arrays are presented. Chapter 5 is a summary and discussion of the future outlook of high-sensitivity far-IR detectors.

References

[1] *Anatomy of a Photodissociation Region*. en. URL: https://webbtelescope.org/contents/media/images/2021/024/01F5KKSNNM6YWR7MNMDJ2NEBCN (visited on 10/13/2024).

[2] Michael D. Audley et al. "Optical performance of an ultra-sensitive horn-coupled transition-edge-sensor bolometer with hemispherical backshort in the far infrared". en. In: *Review of Scientific Instruments* 87.4 (Apr. 2016), p. 043103. ISSN: 0034-6748, 1089-7623. DOI: 10.1063/1.4945302. URL: https://pubs.aip.org/rsi/article/87/4/043103/361191/Optical-performance-of-an-ultra-sensitive-horn (visited on 03/26/2025).

[3] Dominic J. Benford et al. "Mission Concept for the Single Aperture Far-Infrared (SAFIR) Observatory". en. In: *Astrophysics and Space Science* 294.3 (Dec. 2004), pp. 177–212. ISSN: 1572-946X. DOI: 10.1007/s10509-004-5377-4. URL: https://doi.org/10.1007/s10509-004-5377-4 (visited on 03/12/2023).

[4] Charles Matt Bradford et al. "Z-Spec: a broadband millimeter-wave grating spectrometer: design, construction, and first cryogenic measurements". en. In: ed. by Jonas Zmuidzinas, Wayne S. Holland, and Stafford Withington. USA, Oct. 2004, p. 257. DOI: 10.1117/12.552182. URL: http://proceedings.spiedigitallibrary.org/proceeding.aspx?doi=10.1117/12.552182 (visited on 12/14/2024).

[5] Caitlin M. Casey et al. "The Brightest Galaxies in the Dark Ages: Galaxies' Dust Continuum Emission during the Reionization Era". en. In: *The Astrophysical Journal* 862.1 (July 2018), p. 77. ISSN: 1538-4357. DOI: 10.3847/1538-4357/aac82d. URL: https://iopscience.iop.org/article/10.3847/1538-4357/aac82d (visited on 12/01/2023).

[6] *CIGALE – Code Investigating GALaxy Emission*. en-GB. URL: https://cigale.lam.fr/ (visited on 06/12/2025).

[7] Jake Connors et al. "Phononically Isolated TES Detectors for Far-Infrared Spectroscopy". In: 243 (Feb. 2024). Conference Name: American Astronomical Society Meeting Abstracts ADS Bibcode: 2024AAS...24345006C,

p. 450.06. URL: https://ui.adsabs.harvard.edu/abs/2024AAS...24345006C (visited on 03/27/2025).

[8] Gabriele Coppi et al. "The BLAST Observatory: A Sensitivity Study for Far-IR Balloon-borne Polarimeters". en. In: *Publications of the Astronomical Society of the Pacific* 136.3 (Mar. 2024). Publisher: The Astronomical Society of the Pacific, p. 035003. ISSN: 1538-3873. DOI: 10.1088/1538-3873/ad2e11. URL: https://dx.doi.org/10.1088/1538-3873/ad2e11 (visited on 11/16/2024).

[9] *Cosmic Background Explorer*. URL: https://lambda.gsfc.nasa.gov/product/cobe/ (visited on 06/12/2025).

[10] Peter K. Day et al. "A 25-micrometer Single-Photon-Sensitive Kinetic Inductance Detector". In: *Physical Review X* 14.4 (Oct. 2024). Publisher: American Physical Society, p. 041005. DOI: 10.1103/PhysRevX.14.041005. URL: https://link.aps.org/doi/10.1103/PhysRevX.14.041005 (visited on 11/02/2024).

[11] Peter K. Day et al. "A broadband superconducting detector suitable for use in large arrays". en. In: *Nature* 425.6960 (Oct. 2003). Publisher: Nature Publishing Group, pp. 817–821. ISSN: 1476-4687. DOI: 10.1038/nature02037. URL: https://www.nature.com/articles/nature02037 (visited on 11/16/2024).

[12] Herve Dole et al. "The cosmic infrared background resolved by Spitzer - Contributions of mid-infrared galaxies to the far-infrared background". en. In: *Astronomy & Astrophysics* 451.2 (May 2006). Number: 2 Publisher: EDP Sciences, pp. 417–429. ISSN: 0004-6361, 1432-0746. DOI: 10.1051/0004-6361:20054446. URL: https://www.aanda.org/articles/aa/abs/2006/20/aa4446-05/aa4446-05.html (visited on 03/12/2023).

[13] William B. Doriese et al. "Developments in Time-Division Multiplexing of X-ray Transition-Edge Sensors". en. In: *Journal of Low Temperature Physics* 184.1 (July 2016), pp. 389–395. ISSN: 1573-7357. DOI: 10.1007/s10909-015-1373-z. URL: https://doi.org/10.1007/s10909-015-1373-z (visited on 06/12/2025).

[14] Bruce T. Draine. "Interstellar Dust Grains". en. In: *Annual Review of Astronomy and Astrophysics* 41.Volume 41, 2003 (Sept. 2003), pp. 241–289. ISSN: 0066-4146, 1545-4282. DOI: 10.1146/annurev.astro.41.011802.094840. URL: https://www.annualreviews.org/content/journals/10.1146/annurev.astro.41.011802.094840 (visited on 10/13/2024).

[15] Anu Dudhia. "The Reference Forward Model (RFM)". In: *Journal of Quantitative Spectroscopy and Radiative Transfer*. Satellite Remote Sensing and Spectroscopy: Joint ACE-Odin Meeting, October 2015 186 (Jan. 2017), pp. 243–253. ISSN: 0022-4073. DOI: 10.1016/j.jqsrt.2016.06.018.

URL: https://www.sciencedirect.com/science/article/pii/S0022407316301029 (visited on 06/13/2025).

[16] Pierre M. Echternach et al. "Photon shot noise limited detection of terahertz radiation using a quantum capacitance detector". In: *Applied Physics Letters* 103.5 (Aug. 2013), p. 053510. ISSN: 0003-6951. DOI: 10.1063/1.4817585. URL: https://doi.org/10.1063/1.4817585 (visited on 11/16/2024).

[17] Pierre M. Echternach et al. "Single photon detection of 1.5 THz radiation with the quantum capacitance detector". en. In: *Nature Astronomy* 2.1 (Jan. 2018), pp. 90–97. ISSN: 2397-3366. DOI: 10.1038/s41550-017-0294-y. URL: http://www.nature.com/articles/s41550-017-0294-y (visited on 06/02/2021).

[18] ESA/NASA/Planck Collaboration. *Pia15227 All Sky Image Of Molecular Gas And Three Molecular Cloud Complexes Seen By Planck*. en-US. URL: https://www.jpl.nasa.gov/images/pia15227-all-sky-image-of-molecular-gas-and-three-molecular-cloud-complexes-seen-by-planck/ (visited on 03/18/2025).

[19] Duncan Farrah et al. "Review: far-infrared instrumentation and technological development for the next decade". In: *Journal of Astronomical Telescopes, Instruments, and Systems* 5.2 (Apr. 2019). Publisher: SPIE, p. 020901. ISSN: 2329-4124, 2329-4221. DOI: 10.1117/1.JATIS.5.2.020901. URL: https://www.spiedigitallibrary.org/journals/Journal-of-Astronomical-Telescopes-Instruments-and-Systems/volume-5/issue-2/020901/Review--far-infrared-instrumentation-and-technological-development-for-the/10.1117/1.JATIS.5.2.020901.full (visited on 01/30/2025).

[20] Logan Foote et al. "High-sensitivity transition-edge-sensed bolometers: Improved speed and characterization with AC and DC bias". In: *Journal of Applied Physics* 134.9 (Sept. 2023), p. 094503. ISSN: 0021-8979. DOI: 10.1063/5.0157208. URL: https://doi.org/10.1063/5.0157208 (visited on 08/19/2024).

[21] *Frank James Low*. en. June 2021. URL: https://phys-astro.sonoma.edu/brucemedalists/frank-low (visited on 12/10/2024).

[22] Jason Glenn et al. "Galaxy Evolution Probe". In: *Journal of Astronomical Telescopes, Instruments, and Systems* 7, 034004 (July 2021), p. 034004. DOI: 10.1117/1.JATIS.7.3.034004. arXiv: 2109.00614 [astro-ph.GA].

[23] Eduardo González-Alfonso et al. "Feedback and Feeding in the Context of Galaxy Evolution with SPICA: Direct Characterisation of Molecular Outflows and Inflows". In: *Publications of the Astronomical Society of Australia* 34 (Nov. 2017). ADS Bibcode: 2017PASA...34...54G, e054. ISSN: 1323-3580. DOI: 10.1017/pasa.2017.46. URL: https://ui.adsabs.harvard.edu/abs/2017PASA...34...54G (visited on 11/02/2024).

[24] Matt J. Griffin et al. “The Herschel-SPIRE instrument and its in-flight performance”. en. In: *Astronomy & Astrophysics* 518 (July 2010). Publisher: EDP Sciences, p. L3. ISSN: 0004-6361, 1432-0746. DOI: 10.1051/0004-6361/201014519. URL: https://www.aanda.org/articles/aa/abs/2010/10/aa14519-10/aa14519-10.html (visited on 10/07/2021).

[25] Mélanie Habouzit et al. “Supermassive black holes in cosmological simulations I: MBH - $M_\star$ relation and black hole mass function”. In: *Monthly Notices of the Royal Astronomical Society* 503 (May 2021). Publisher: OUP ADS Bibcode: 2021MNRAS.503.1940H, pp. 1940–1975. ISSN: 0035-8711. DOI: 10.1093/mnras/stab496. URL: https://ui.adsabs.harvard.edu/abs/2021MNRAS.503.1940H (visited on 12/09/2024).

[26] David A. Harper Jr. and Frank J. Low. “Far-Infrared Observations of Galactic Nuclei”. In: *The Astrophysical Journal* 182 (June 1973). Publisher: IOP ADS Bibcode: 1973ApJ...182L..89H, p. L89. ISSN: 0004-637X. DOI: 10.1086/181226. URL: https://ui.adsabs.harvard.edu/abs/1973ApJ...182L..89H (visited on 10/19/2024).

[27] Brandon S. Hensley and B. T. Draine. “Observational Constraints on the Physical Properties of Interstellar Dust in the Post-Planck Era”. In: *The Astrophysical Journal* 906.2 (Jan. 2021), p. 73. ISSN: 0004-637X, 1538-4357. DOI: 10.3847/1538-4357/abc8f1. URL: https://iopscience.iop.org/article/10.3847/1538-4357/abc8f1 (visited on 03/17/2025).

[28] *Herschel Space Observatory*. URL: https://www.herschel.caltech.edu/ (visited on 06/12/2025).

[29] Mark Heyer and Tom M. Dame. “Molecular Clouds in the Milky Way”. en. In: *Annual Review of Astronomy and Astrophysics* 53.Volume 53, 2015 (Aug. 2015). Publisher: Annual Reviews, pp. 583–629. ISSN: 0066-4146, 1545-4282. DOI: 10.1146/annurev-astro-082214-122324. URL: https://www.annualreviews.org/content/journals/10.1146/annurev-astro-082214-122324 (visited on 02/27/2025).

[30] Ryan C. Hickox and David M. Alexander. “Obscured Active Galactic Nuclei”. en. In: *Annual Review of Astronomy and Astrophysics* 56.Volume 56, 2018 (Sept. 2018). Publisher: Annual Reviews, pp. 625–671. ISSN: 0066-4146, 1545-4282. DOI: 10.1146/annurev-astro-081817-051803. URL: https://www.annualreviews.org/content/journals/10.1146/annurev-astro-081817-051803 (visited on 10/13/2024).

[31] *Home - ISO - Cosmos*. en-GB. URL: https://www.cosmos.esa.int/web/iso (visited on 06/12/2025).

[32] *How to become a star | ESO*. Jan. 2001. URL: https://www.eso.org/public/images/eso0102a/ (visited on 08/19/2024).

[33] *In search of our cosmic origins | ALMA Observatory*. en-US. URL: https://www.almaobservatory.org/ (visited on 06/12/2025).

[34] Hanae Inami et al. “The ALMA REBELS Survey: dust continuum detections at z > 6.5”. In: *Monthly Notices of the Royal Astronomical Society* 515 (Sept. 2022). Publisher: OUP ADS Bibcode: 2022MNRAS.515.3126I, pp. 3126–3143. ISSN: 0035-8711. DOI: 10.1093/mnras/stac1779. URL: https://ui.adsabs.harvard.edu/abs/2022MNRAS.515.3126I (visited on 11/23/2024).

[35] *Interstellar Medium and Molecular Clouds | Center for Astrophysics | Harvard & Smithsonian*. URL: https://www.cfa.harvard.edu/research/topic/interstellar-medium-and-molecular-clouds (visited on 03/05/2025).

[36] *IRAS Explanatory Supplement*. June 26, 1997. URL: https://irsa.ipac.caltech.edu/IRASdocs/exp.sup/index.html (visited on 10/26/2024).

[37] Reinier M. J. Janssen et al. “Single Pixel Performance of the Kinetic Inductance Detectors for the Terahertz Intensity Mapper”. In: *Journal of Low Temperature Physics* 211 (June 2023). Publisher: Springer ADS Bibcode: 2023JLTP..211..197J, pp. 197–206. ISSN: 1063-777X0022-2291. DOI: 10.1007/s10909-022-02830-9. URL: https://ui.adsabs.harvard.edu/abs/2023JLTP..211..197J (visited on 11/04/2024).

[38] Matthew Kenyon et al. “Toward a Detector/Readout Architecture for the Background-Limited Far-IR/Submm Spectrograph (BLISS)”. In: *J. Low Temp. Phys.* 176.3 (Jan. 2014), pp. 376–382. DOI: 10.1007/s10909-013-1020-5. URL: https://doi.org/10.1007/s10909-013-1020-5.

[39] Pourya Khosropanah et al. “Ultra-low noise TES bolometer arrays for SAFARI instrument on SPICA”. In: ed. by Wayne S. Holland and Jonas Zmuidzinas. Edinburgh, United Kingdom, July 2016, 99140B. DOI: 10.1117/12.2233472. URL: http://proceedings.spiedigitallibrary.org/proceeding.aspx?doi=10.1117/12.2233472 (visited on 03/26/2025).

[40] David T. Leisawitz et al. “SPECS: the kilometer-baseline far-IR interferometer in NASA’s space science roadmap”. en. In: ed. by John C. Mather. USA, Oct. 2004, p. 1527. DOI: 10.1117/12.552150. URL: http://proceedings.spiedigitallibrary.org/proceeding.aspx?doi=10.1117/12.552150 (visited on 11/16/2024).

[41] Lun-Jun Liu et al. “Cosmic Ray Susceptibility of the Terahertz Intensity Mapper Detector Arrays”. en. In: *Journal of Low Temperature Physics* 216.1-2 (July 2024), pp. 195–207. ISSN: 0022-2291, 1573-7357. DOI: 10.1007/s10909-024-03123-z. URL: https://link.springer.com/10.1007/s10909-024-03123-z (visited on 04/19/2025).

[42] Frank J. Low. “Low-Temperature Germanium Bolometer”. EN. In: *JOSA* 51.11 (Nov. 1961). Publisher: Optica Publishing Group, pp. 1300–1304. DOI: 10.1364/JOSA.51.001300. URL: https://opg.optica.org/josa/abstract.cfm?uri=josa-51-11-1300 (visited on 10/19/2024).

[43] Frank J. Low and Wallace H. Tucker. "Contribution of Infrared Galaxies to the Cosmic Background". In: *Physical Review Letters* 21.22 (Nov. 1968). Publisher: American Physical Society, pp. 1538–1541. DOI: 10.1103/PhysRevLett.21.1538. URL: https://link.aps.org/doi/10.1103/PhysRevLett.21.1538 (visited on 10/19/2024).

[44] Piero Madau and Mark Dickinson. "Cosmic Star Formation History". en. In: *Annual Review of Astronomy and Astrophysics* 52.1 (Aug. 2014). arXiv: 1403.0007, pp. 415–486. ISSN: 0066-4146, 1545-4282. DOI: 10.1146/annurev-astro-081811-125615. URL: http://arxiv.org/abs/1403.0007 (visited on 11/29/2020).

[45] Samuel J. Maddox et al. "The Herschel-ATLAS Data Release 2. Paper II. Catalogs of Far-infrared and Submillimeter Sources in the Fields at the South and North Galactic Poles". en. In: *The Astrophysical Journal Supplement Series* 236.2 (May 2018). Publisher: The American Astronomical Society, p. 30. ISSN: 0067-0049. DOI: 10.3847/1538-4365/aab8fc. URL: https://dx.doi.org/10.3847/1538-4365/aab8fc (visited on 03/05/2025).

[46] Daniel P. Marrone et al. "The terahertz intensity mapper: a balloon-borne imaging spectrometer for galaxy evolution". In: 12190 (Aug. 2022). Conference Name: Millimeter, Submillimeter, and Far-Infrared Detectors and Instrumentation for Astronomy XI ADS Bibcode: 2022SPIE12190E..08M, p. 1219008. DOI: 10.1117/12.2630644. URL: https://ui.adsabs.harvard.edu/abs/2022SPIE12190E..08M (visited on 11/04/2024).

[47] Margaret Meixner et al. *Origins Space Telescope Mission Concept Study Report*. 2019. DOI: 10.48550/ARXIV.1912.06213. URL: https://arxiv.org/abs/1912.06213.

[48] Kelsey M. Morgan et al. "Code-division-multiplexed readout of large arrays of TES microcalorimeters". In: *Applied Physics Letters* 109.11 (Sept. 2016), p. 112604. ISSN: 0003-6951. DOI: 10.1063/1.4962636. URL: https://doi.org/10.1063/1.4962636 (visited on 06/12/2025).

[49] Dirk Muehlner and Rainer Weiss. "Balloon Measurements of the Far-Infrared Background Radiation". In: *Physical Review D* 7.2 (Jan. 1973). Publisher: American Physical Society, pp. 326–344. DOI: 10.1103/PhysRevD.7.326. URL: https://link.aps.org/doi/10.1103/PhysRevD.7.326 (visited on 10/25/2024).

[50] Norman Murray. "Star Formation Efficiencies and Lifetimes of Giant Molecular Clouds in the Milky Way". en. In: *The Astrophysical Journal* 729.2 (Feb. 2011). Publisher: The American Astronomical Society, p. 133. ISSN: 0004-637X. DOI: 10.1088/0004-637X/729/2/133. URL: https://dx.doi.org/10.1088/0004-637X/729/2/133 (visited on 03/05/2025).

[51] National Research Council (U.S.), ed. *Astronomy and astrophysics in the new millennium*. Washington, D.C: National Academy Press, 2001. ISBN: 978-0-309-07312-7 978-0-309-07031-7.

[52] Trevor Oxholm et al. "The EXperiment for Large-Aperture Intensity Mapping (EXCLAIM)". In: 236 (June 2020). Conference Name: American Astronomical Society Meeting Abstracts #236 ADS Bibcode: 2020AAS...23624402O, p. 244.02. URL: https://ui.adsabs.harvard.edu/abs/2020AAS...236244020 (visited on 11/16/2024).

[53] Juan R. Pardo, J. Cernicharo, and E. Serabyn. "Atmospheric transmission at microwaves (ATM): an improved model for millimeter/submillimeter applications". In: *IEEE Transactions on Antennas and Propagation* 49.12 (Dec. 2001), pp. 1683–1694. ISSN: 1558-2221. DOI: 10.1109/8.982447. URL: https://ieeexplore.ieee.org/abstract/document/982447 (visited on 06/13/2025).

[54] *Planet Formation | Center for Astrophysics | Harvard & Smithsonian*. URL: https://www.cfa.harvard.edu/research/topic/planet-formation (visited on 03/05/2025).

[55] Klaus Pontoppidan. Personal Communication. Oct. 2024.

[56] G. Presta et al. "The first flight of the OLIMPO experiment: instrument performance". en. In: *Journal of Physics: Conference Series* 1548.1 (May 2020). Publisher: IOP Publishing, p. 012018. ISSN: 1742-6596. DOI: 10.1088/1742-6596/1548/1/012018. URL: https://dx.doi.org/10.1088/1742-6596/1548/1/012018 (visited on 12/17/2024).

[57] Jean-Loup Puget et al. "Tentative detection of a cosmic far-infrared background with COBE." In: *Astronomy and Astrophysics* 308 (Apr. 1996). ADS Bibcode: 1996A&A...308L...5P, p. L5. ISSN: 0004-6361. URL: https://ui.adsabs.harvard.edu/abs/1996A&A...308L...5P (visited on 10/26/2024).

[58] Amy E. Reines and Marta Volonteri. "Relations between Central Black Hole Mass and Total Galaxy Stellar Mass in the Local Universe". In: *The Astrophysical Journal* 813 (Nov. 2015), p. 82. ISSN: 0004-637X. DOI: 10.1088/0004-637X/813/2/82. URL: https://ui.adsabs.harvard.edu/abs/2015ApJ...813...82R (visited on 11/02/2024).

[59] George H. Rieke et al. "The Multiband Imaging Photometer for Spitzer (MIPS)". In: *The Astrophysical Journal Supplement Series* 154 (Sept. 2004). Publisher: IOP ADS Bibcode: 2004ApJS..154...25R, pp. 25–29. ISSN: 0067-0049. DOI: 10.1086/422717. URL: https://ui.adsabs.harvard.edu/abs/2004ApJS..154...25R (visited on 06/12/2025).

[60] Alessandro Schillaci et al. *BICEP Array: 150 GHz detector module development*. en. arXiv:2111.14785 [astro-ph]. Nov. 2021. DOI: 10.48550/arXiv.

2111.14785. URL: http://arxiv.org/abs/2111.14785 (visited on 12/17/2024).

[61] Raffaella Schneider and Roberto Maiolino. "The formation and cosmic evolution of dust in the early Universe: I. Dust sources". en. In: *The Astronomy and Astrophysics Review* 32.1 (Apr. 2024), p. 2. ISSN: 1432-0754. DOI: 10.1007/s00159-024-00151-2. URL: https://doi.org/10.1007/s00159-024-00151-2 (visited on 03/06/2025).

[62] Matthew D. Shaw et al. "The Quantum Capacitance Detector: A concept for a pair-breaking radiation detector based on the single Cooper-pair box". In: *Physical Review B* 79.14 (Apr. 2009). arXiv: 0902.4194, p. 144511. ISSN: 1098-0121, 1550-235X. DOI: 10.1103/PhysRevB.79.144511. URL: http://arxiv.org/abs/0902.4194 (visited on 03/01/2022).

[63] Jonathan D. T. Smith et al. "The Mid-Infrared Spectrum of Star-forming Galaxies: Global Properties of Polycyclic Aromatic Hydrocarbon Emission". In: *The Astrophysical Journal* 656 (Feb. 2007). Publisher: IOP ADS Bibcode: 2007ApJ...656..770S, pp. 770–791. ISSN: 0004-637X. DOI: 10.1086/510549. URL: https://ui.adsabs.harvard.edu/abs/2007ApJ...656..770S (visited on 03/19/2025).

[64] *SOFIA Observatory Overview | SOFIA Science Center*. URL: https://irsa.ipac.caltech.edu/data/SOFIA/docs/about-sofia/sofia-overview/ (visited on 12/10/2024).

[65] Laura Sommovigo et al. "Warm dust in high-z galaxies: origin and implications". In: *Monthly Notices of the Royal Astronomical Society* 497.1 (Sept. 2020), pp. 956–968. ISSN: 0035-8711. DOI: 10.1093/mnras/staa1959. URL: https://doi.org/10.1093/mnras/staa1959 (visited on 10/13/2024).

[66] SPICA Study Team. "SPICA Mission Study Summary Report". en. In: *ESA Unclassified* ESA-SPI-EST-MIS-RP-001.1.1 (July 2021), p. 106. URL: https://sci.esa.int/web/future-missions-department/-/spica-mission-study-summary-report.

[67] Johannes Staguhn et al. "Design of Large Low Noise Transition Edge Sensor Arrays for Future FIR Space Missions". en. In: *Journal of Low Temperature Physics* 215.3-4 (May 2024), pp. 193–200. ISSN: 0022-2291, 1573-7357. DOI: 10.1007/s10909-024-03084-3. URL: https://link.springer.com/10.1007/s10909-024-03084-3 (visited on 03/27/2025).

[68] *Star Formation | Center for Astrophysics | Harvard & Smithsonian*. URL: https://www.cfa.harvard.edu/research/topic/star-formation (visited on 10/13/2024).

[69] T. Suzuki et al. "Development of Ultra-Low-Noise TES Bolometer Arrays". en. In: *Journal of Low Temperature Physics* 184.1-2 (July 2016), pp. 52–59. ISSN: 0022-2291, 1573-7357. DOI: 10.1007/s10909-015-1401-z. URL:

http://link.springer.com/10.1007/s10909-015-1401-z (visited on 03/26/2025).

[70] Emanuele Taralli et al. "Complex impedance of TESs under AC bias using FDM readout system". en. In: *AIP Advances* 9.4 (Apr. 2019), p. 045324. ISSN: 2158-3226. DOI: 10.1063/1.5089739. URL: https://pubs.aip.org/adv/article/9/4/045324/1076692/Complex-impedance-of-TESs-under-AC-bias-using-FDM (visited on 06/12/2025).

[71] *The PRobe far-Infrared Mission for Astrophysics (PRIMA)*. URL: https://prima.ipac.caltech.edu/ (visited on 11/04/2024).

[72] Robert J. Trumpler. "Absorption of Light in the Galactic System". In: *Publications of the Astronomical Society of the Pacific* 42 (Aug. 1930). Publisher: IOP ADS Bibcode: 1930PASP...42..214T, p. 214. ISSN: 0004-6280. DOI: 10.1086/124039. URL: https://ui.adsabs.harvard.edu/abs/1930PASP...42..214T (visited on 10/19/2024).

[73] Sylvain Veilleux et al. "Cool outflows in galaxies and their implications". In: *Astronomy and Astrophysics Review* 28 (Apr. 2020). Publisher: Springer ADS Bibcode: 2020A&ARv..28....2V, p. 2. ISSN: 0935-4956. DOI: 10.1007/s00159-019-0121-9. URL: https://ui.adsabs.harvard.edu/abs/2020A&ARv..28....2V (visited on 11/02/2024).

[74] Joaquin Vieira et al. "The Terahertz Intensity Mapper (TIM): an Imaging Spectrometer for Galaxy Evolution Studies at High-Redshift". en. In: *2019 30th International Symposium on Space Terahertz Technology, ISSTT 2019, Gothenburg, Sweden* (2019).

[75] Joris Witstok et al. "Carbonaceous dust grains seen in the first billion years of cosmic time". en. In: *Nature* 621.7978 (Sept. 2023). Publisher: Nature Publishing Group, pp. 267–270. ISSN: 1476-4687. DOI: 10.1038/s41586-023-06413-w. URL: https://www.nature.com/articles/s41586-023-06413-w (visited on 10/13/2024).

[76] W. Yoon et al. "Toward Large Field-of-View High-Resolution X-ray Imaging Spectrometers: Microwave Multiplexed Readout of 28 TES Microcalorimeters". en. In: *Journal of Low Temperature Physics* 193.3-4 (Nov. 2018), pp. 258–266. ISSN: 0022-2291, 1573-7357. DOI: 10.1007/s10909-018-1917-0. URL: http://link.springer.com/10.1007/s10909-018-1917-0 (visited on 06/12/2025).

[77] Harold W. Yorke et al. "SAFIR, the Single Aperture Far-Infrared Observatory, the next big step beyond SIRTF and Herschel". In: 201 (Dec. 2002). Conference Name: American Astronomical Society Meeting Abstracts ADS Bibcode: 2002AAS...20115104Y, p. 151.04. URL: https://ui.adsabs.harvard.edu/abs/2002AAS...20115104Y (visited on 11/16/2024).

[78] J Zmuidzinas. “The Role of Coherent Detection”. en. In: *New Concepts for FarInfrared and Submillimeter Space Astronomy* NASA CP–2003–212233 (2003), p. 329.

Chapter 2

HIGH-SENSITIVITY FAR-INFRARED DETECTORS

2.1 Photon Noise

Photon detection can be categorized based on the rate of photons Γ_{photon} in relation to the detector time constant τ_{detector}. For $\Gamma_{\text{photon}}\tau_{\text{detector}} \ll 1$, or photon-counting mode, single photons can be detected if the detector is sufficiently sensitive, and the sensitivity can be quantified by the energy threshold, or the minimum energy photon that can be detected. For $\Gamma_{\text{photon}}\tau_{\text{detector}} \gg 1$, or integrating mode, the detector measures the power of the absorbed radiation rather than individual photons, and the sensitivity can be characterized by the noise equivalent power (NEP), which is the absorbed power for which the signal-to-noise is 1 in a 1 Hz measurement bandwidth.

A fundamental limit to measurement sensitivity is noise due to the random arrival of photons, which can be expressed as

$$\text{NEP}_{\text{photon}} = \sqrt{2\Delta\nu N_{\text{modes}}\bar{n}(\bar{n}+1)}\,h\nu_{\text{photon}}, \tag{2.1}$$

where $h\nu_{\text{photon}}$ is the photon energy, $\bar{n}$ is the absorbed photon occupation number, $\Delta\nu$ is the optical bandwidth of the photon stream absorbed by the detector, and N_{modes} is the number of spatial modes.[54] The photon occupation number is the rate of photons per second per Hz of optical bandwidth per photon mode. For a blackbody in thermal equilibrium at temperature T, it is described by the Planck distribution:

$$\bar{n} = \frac{1}{e^{h\nu_{\text{photon}}/k_B T} - 1}. \tag{2.2}$$

The absorbed power in the detector is

$$P_{\text{abs}} = \bar{n} h\nu_{\text{photon}} \Delta\nu N_{\text{modes}}. \tag{2.3}$$

The photon noise can be explored in two regimes. For $\bar{n} \gg 1$ (the "radio regime"), the NEP is dominated by wave noise:

$$\text{NEP}_{\text{photon}}^{\text{radio}} = \sqrt{\frac{2}{\Delta\nu N_{\text{modes}}}}\,P_{\text{abs}}. \tag{2.4}$$

For $\bar{n} \ll 1$ (the "IR/optical regime"), the NEP is dominated by shot noise:

$$\text{NEP}_{\text{photon}}^{\text{IR/optical}} = \sqrt{2P_{\text{abs}}h\nu_{\text{photon}}}. \tag{2.5}$$

PRIMA's low-resolution spectrometer has an occupation number that satisfies $\bar{n} \ll 1$ over its full operating range, so Equation 2.5 will be used for the photon noise in the following sections. This condition is also met for the measurements using a blackbody source in this thesis. $\mathrm{NEP}_{\mathrm{photon}}$ places a fundamental limit on the sensitivity that can be achieved for a particular observation, and thus provides a target for the detector sensitivity. All detectors have intrinsic detector noise $\mathrm{NEP}_{\mathrm{detector}}$, detailed in Sections 2.3 and 2.4 for Transition Edge Sensors (TESs) and Kinetic Inductance Detectors (KIDs), respectively. The signal from a detector must be amplified, and the amplifier will introduce further noise into the signal chain. The total NEP is thus given by

$$\mathrm{NEP}^2_{\mathrm{total}} = \mathrm{NEP}^2_{\mathrm{photon}} + \mathrm{NEP}^2_{\mathrm{detector}} + \mathrm{NEP}^2_{\mathrm{amplifier}},$$

and the fundamental photon noise limit is achieved when

$$\mathrm{NEP}^2_{\mathrm{photon}} \gg \mathrm{NEP}^2_{\mathrm{detector}} + \mathrm{NEP}^2_{\mathrm{amplifier}}.$$

For a given detector, one wishes to reduce amplifier noise such that

$$\mathrm{NEP}^2_{\mathrm{amplifier}} \ll \mathrm{NEP}^2_{\mathrm{detector}}.$$

2.2 Detector Requirements

Many detector and array level characteristics must be optimized when designing an instrument. The detector characteristics for observations in integrating mode and the PRIMA requirements for each are listed in Table 2.1. The detector noise $\mathrm{NEP}_{\mathrm{detector}}$ is a function of the absorbed power P_{abs}. In the following sections, it is assumed that $\mathrm{NEP}_{\mathrm{amplifier}} \ll \mathrm{NEP}_{\mathrm{detector}}$. Then, the detector sensitivity can be characterized by two numbers: $\mathrm{NEP}^0_{\mathrm{abs}}$, or the sensitivity to absorbed power at $P_{\mathrm{abs}} = 0$, and P_{max}, or the maximum power for which the detector remains photon-noise limited. $\mathrm{NEP}^0_{\mathrm{abs}}$ is set such that the photon noise of the natural astrophysical background will dominate the total NEP. P_{max} is set by the brightest sources PRIMA aims to observe. The power absorbed by each detector is modified by instrument-dependent optical efficiencies. For a detailed calculation of the expected photon noise on each detector for a far-IR space telescope, see Appendix A. Here, the optical efficiencies are treated separately from the detector NEP referred to P_{abs}.

The sensitivity must be achieved over a range of frequency ν, which is determined by the types of astronomical sources observed and the signal modulation strategies employed. Recovering large spatial scales with scan mapping, for example, requires

good detector performance and low frequencies. The lowest usable frequency is set by the level of $1/f$ noise in the instrument and detectors, and can be given by $\nu_{\min}$, or the minimum frequency for which the NEP requirement is met. The highest usable frequency is set by the detector time constant $\tau_{\text{detector}} = 1/(2\pi\nu_{\max})$. The requirement on τ_{detector} is set for cosmic ray removal and flexibility in chopping and mapping.

The array size, format, and yield are set by the specifics of the instrument. The array size is constrained by the multiplexing factor for the detector type as well as fabrication practicalities. The array yield can be defined in various ways. In this thesis, "measurement yield" is defined as the number of operational pixels that can be read out simultaneously, "yield" is defined as the pixels within the measurement yield that meet all detector requirements, and "fabrication yield" refers to the number of pixels that were successfully fabricated. Note that pixels that can be read out but do not meet all the other requirements may still be useful for certain observations.

Finally, some fraction of observation time may be lost due to cosmic rays. This effect can be mitigated by removing data where a cosmic ray strike occurs, producing a temporal efficiency ϵ_{CR}.

Parameter	Description	PRIMA requirement
$\text{NEP}^0_{\text{abs}}$	The NEP referred to absorbed power with $P_{\text{abs}} = 0$.	$< 1 \times 10^{-19}$ W/$\sqrt{\text{Hz}}$
$P_{\max}$	The maximum absorbed power for which the detector is photon noise limited.	> 1.2 fW
τ_{detector}	The detector time constant. Sets the upper limit on observation frequencies.	< 3 ms
$\nu_{\min}$	The minimum frequency at which the NEP requirement is met.	No strict requirement, but ideally < 0.1 Hz
Array size	Number of pixels in the spectral and spatial directions. Typically limited by multiplex factor.	63 spatial X 16 spectral per array, 8 arrays
Array yield	Fraction of operational detectors that achieve all other requirements and can be read out simultaneously	> 80%
ϵ_{CR}	Cosmic ray temporal efficiency. The fraction of the data that must be discarded due to cosmic ray hits is $1-\epsilon_{\text{CR}}$.	> 0.9

Table 2.1: General detector array characteristics and PRIMA detector requirements.

The following sections lay out the principals behind the operation of TESs (Section 2.3) and KIDs (Section 2.4). The detection mechanism, response, and noise are discussed for each.

2.3 Transition Edge Sensors: Operation and Noise

Transition-edge sensed (TES) bolometers and their superconducting quantum interference device (SQUID)-based readout systems have been the detectors of choice for many recent ground-based astrophysics and cosmology experiments in the trans-millimeter bands [ACT (2015),[47,51] Bicep2,[4] Bicep3,[3] GISMO,[45] HAWK+,[22] Keck Experiment,[26] PolarBear,[10] SPIDER,[1] SPT,[44] etc.]. TES bolometer arrays have generally demonstrated excellent systematic performance in deep microwave background measurements (BICEP-Keck/SPIDER Collaboration 2015,[2] SPT 2018,[15] BICEP-Keck Collaboration 2022,[3] ACT[51]). They are, thus, a strong candidate for future space missions, which would have lower backgrounds, both in the CMB bands (EPIC,[7] Litebird[9]) and also in the far-infrared (far-IR), where no commercial high-performance detector systems exist.

This section describes the principles behind TES operation. The detection mechanism and response are described in Subsection 2.3.1, TES noise is described in Subsection 2.3.2, and the method for achieving high-sensitivity is discussed in Subsection 2.3.3

2.3.1 Detection Mechanism and Response

A TES is a bolometer that makes use of the steep resistance versus temperature $R(T, I)$ of a superconductor. TESs are typically read out by applying a bias voltage V and measuring the current $I = V/R$ with a SQUID. The TES is fabricated on an island with an absorber, which is connected to the substrate and thermal bath via thin legs. The island has heat capacity C and thermal conductance to the bath G. Changes in the TES resistance R, temperature T, and current I are related through

$$\frac{\delta R}{R} = \alpha \frac{\delta T}{T} + \beta \frac{\delta I}{I}, \tag{2.6}$$

where $\alpha = \partial \log R / \partial \log T \gg 1$ is the logarithmic temperature sensitivity of the superconducting transition and $\beta = \partial \log R / \partial \log I$ is the logarithmic current sensitivity of the superconducting transition. The small-signal power balance equation is

$$C \frac{d\delta T}{dt} = -G\delta T + \delta U + \delta P_{\text{bias}} + \delta P_{\text{abs}}, \tag{2.7}$$

where δU is the phonon noise, δP_{bias} is the change in the bias power, and δP_{abs} is the photon noise. For DC bias, the power is given by $P_{\text{bias}} = IV$, so the bias power fluctuations are

$$\delta P_{\text{bias}} = V\delta I + I\delta V. \tag{2.8}$$

The voltage fluctuations can be written as

$$\delta V = R\delta I + I\delta R - R\delta i_{\text{n}}, \tag{2.9}$$

where δi_{n} is the Johnson noise current. Equations 2.6, 2.7, 2.8, and 2.9 can be solved for the current fluctuations δI assuming δV is known. The electrothermal feedback factor A is defined as

$$A = 1 + \frac{\alpha}{1+\beta}\frac{P_{\text{bias}}}{GT}. \tag{2.10}$$

For the typical case of strong electrothermal feedback ($A \gg 1$), the current fluctuation equation in the frequency domain is

$$\delta I = \frac{1}{1+\beta}\left[1 - \frac{1-A^{-1}}{1+j2\pi\nu\tau'}\right]\delta i_n - \left[\frac{1}{1+j2\pi\nu\tau'}\right]\frac{\delta P_{\text{abs}} + \delta U}{V_{\text{bias}}} \tag{2.11}$$

$$+ \frac{1}{1+\beta}\left[1 - (2+\beta)\frac{1}{1+j2\pi\nu\tau'}\right]\frac{\delta V}{R}, \tag{2.12}$$

where the modified time constant is $\tau' = \tau/A$ and $\tau = C/G$.

The responsivity is then

$$\left|\frac{\partial\delta I(\nu)}{\partial\delta P_{\text{abs}}}\right| = \frac{1}{V}\frac{1}{\sqrt{1+(2\pi\nu\tau')^2}}. \tag{2.13}$$

2.3.2 Noise

Irwin has shown that the PSD of the Johnson noise voltage in a TES — a nonlinear resistor — is given by $S_{\delta i_n} = 4(1+2\beta)k_BT/R$,[25] so the PSD of the resulting noise current flowing through the voltage-biased TES bolometer is given by

$$S_{\text{Johnson}} = \frac{4kT}{R}\frac{(1+2\beta)}{A^2(1+\beta)^2}\frac{1}{1+(2\pi\nu\tau')^2}. \tag{2.14}$$

The phonon noise is analogous to photon noise because thermal phonons behave stochastically. The phonon noise is[25]

$$S_{\text{phonon}} = 4k_BT^2G\frac{1}{1+(2\pi\nu\tau')^2}. \tag{2.15}$$

The total NEP is therefore

$$\mathrm{NEP}_{\mathrm{total}}^2 = \frac{1}{1+(2\pi\nu\tau')^2}\left[\mathrm{NEP}_{\mathrm{photon}}{}^2 + \mathrm{NEP}_{\mathrm{phonon}}^2 + \mathrm{NEP}_{\mathrm{Johnson}}^2\right] + \mathrm{NEP}_{\mathrm{SQUID}}^2, \tag{2.16}$$

where

$$\mathrm{NEP}_{\mathrm{phonon}}^2 = 4k_B T^2 G \tag{2.17}$$

$$\mathrm{NEP}_{\mathrm{Johnson}}^2 = \frac{4k_B T}{R}\frac{1+2\beta}{A^2(1+\beta)^2}, \tag{2.18}$$

$\mathrm{NEP}_{\mathrm{photon}}$ is given in Equation 2.5, and $\mathrm{NEP}_{\mathrm{SQUID}}$ can be calculated by dividing the SQUID current noise by the responsivity. The above equations have been derived under AC bias, and found to obey the same form, with a modest modification to α and β.[30]

2.3.3 NEP Optimization

For a well-designed TES, the phonon noise term will dominate. Thus, achieving higher sensitivity requires lowering the thermal conductance and/or lowering the operating temperature, though the latter may be limited by system resources in space applications. The time constant, modified by the electrothermal feedback factor, is

$$\tau' = \frac{C}{G}\left[1 + \frac{\alpha}{1+\beta}\frac{P_{\mathrm{bias}}}{GT}\right]^{-1}. \tag{2.19}$$

P_{bias}/GT is typically of order unity, so $\tau' \sim [(1+\beta)/(1+\beta+\alpha)]\,C/G$. Thus, the time constant requirement will place a limit on how far G can be lowered. Furthermore, the saturation power of a TES is proportional to G, so low-G TESs will have a restrictive limit on the brightest sources that can be observed. To maintain sufficient speed, the heat capacity can be reduced or α can be raised. However, reducing the heat capacity is not trivial (see Chapter 3), and devices with high α are known to exhibit additional noise not covered here, namely non-equilibrium nonlinear Johnson noise and internal noise from thermal fluctuations.[16] Several groups have attempted to balance these competing design parameters, as detailed in Chapter 3. However, to date, no TES has achieved NEP $< 1\times10^{-19}$ W/$\sqrt{\mathrm{Hz}}$ and $\tau < 3$ ms simultaneously.

2.4 Kinetic Inductance Detectors: Operation and Noise

KIDs detect light through quasiparticle (QP) production in a superconducting film. Changes in the QP density in the film change the surface impedance, which can be measured by embedding it in an LC resonant circuit and measuring the change in the resonator frequency and dissipation. Because KIDs are resonators, they are inherently multiplexable in the frequency domain. KIDs can achieve very high internal quality factors (Typically > 50,000) because the dissipation in a superconductor is small.

KIDs can be categorized by the method used for absorbing photons: (1) antenna-coupled KIDs: radiation is coupled into the KID through an antenna and transmission line. (2) Lumped-Element KIDs (LEKIDs): the inductor absorbs radiation directly. (3) Temperature-sensing KIDs (TKIDs): the radiation is converted into phonons in an absorber which is thermally coupled to the inductor on an isolated island, similar to a bolometer. Antenna-coupled KIDs and LEKIDs detect radiation through the QPs directly produced by radiation. TKIDs detect radiation through the thermal QP density. This section covers the physics governing KIDs and provides derivations of the response and noise for antenna-coupled KIDs and LEKIDs. The response and noise of TKIDs is not covered here, but it can be understood by combining the bolometer framework with the temperature response derived below.[50] The detection mechanism of KIDs is detailed in Subsection 2.4.1, the response of KIDs is detailed in Subsection 2.4.2, and noise in KIDs is detailed in Subsection 2.4.3.

2.4.1 Detection Mechanism

To understand the detection mechanism of a KID, one must derive the relationship between the observable resonant circuit parameters and the QP density n_{QP}, the relationship between n_{QP} and the absorbed power P_{abs}, and the dependence of each of these parameters on other relevant quantities. The relations have been derived in a number of sources.[34,17,13] A schematic of the resonant circuit is drawn in figure 2.1. The LC resonator is depicted by the impedance Z, which typically consists of a capacitor in parallel with the absorber. The imaginary part of the surface impedance of the absorber is dominated by the kinetic inductance and, depending on the geometry of the absorber, the geometric inductance. The real part of the surface impedance of the absorber provides dissipation.

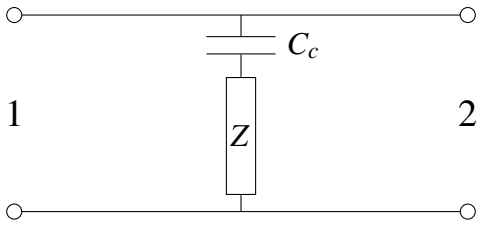

Figure 2.1: Schematic of the KID circuit. The impedance Z typically consists of a capacitor in parallel with the absorber.

The resonance is probed through S_{21}, the complex transmission from port 1 to port 2. The transmission through the KID resonant circuit, as measured through a frequency sweep of a probe tone across the resonance, can be modelled as[17,34,37]

$$S_{21} = 1 - \frac{1}{1 + 2jy} \frac{Q_r}{Q_c \cos\phi} e^{j\phi}. \tag{2.20}$$

This equation is discussed further in Appendix B. The coupling quality factor is Q_c, the internal quality factor is Q_i, and the total quality factor is $Q_r = 1/(1/Q_c + 1/Q_i)$. The quality factors can be calculated from the circuit model if the component values are known. The angle ϕ accounts for the impedance mismatch in the circuit.[27] The resonant frequency is f_r, and takes on the value $f_{r,0}$ at $T = 0$ and $P_{\text{abs}} = 0$, such that the fractional frequency shift is

$$x = \frac{f - f_{r,0}}{f_{r,0}}. \tag{2.21}$$

The kinetic inductance of KIDs is nonlinear, and microwave QP generation can lead to further nonlinearities.[46] Accounting for this nonlinearity, the frequency sweep data can be modelled by introducing y, the spacing between the tone frequency and the resonant frequency, which is calculated from the solution to

$$y - \frac{a_{\text{nl}}}{1 + 4y^2} = y_0 = Q_r x, \tag{2.22}$$

where the nonlinearity parameter a_{nl} is proportional to the microwave power $P_{\mu\text{W}}$. The equation has one real solution for y for $a_{\text{nl}} \leq 4\sqrt{3}/9$. For $a_{\text{nl}} > 4\sqrt{3}/9$, a range of y_0 produces two real and stable solutions, so the resonator is said to have undergone bifurcation. When bifurcated, the tone frequency and the resonant frequency have a hysteretic relationship, so the bifurcation power sets a practical upper limit to the microwave tone power.

The detection mechanism of the KID can be understood by calculating the complex impedance of the absorber as a function of temperature and absorbed power using

the Mattis-Bardeen theory. The complex impedance can then be related to δQ_i^{-1} and x, which are observable through the complex circuit transmission S_{21}. In addition to changes in the complex impedance of the absorber, x and δQ_i^{-1} exhibit an additional temperature dependence due to two-level systems (TLSs) in the capacitor. The detector noise consists of surface impedance fluctuations due to QP noise or capacitance fluctuations due to TLS noise. In general, x and δQ_i^{-1} can be written as

$$x(T, P_{\text{abs}}) = x_{\text{TLS}}(T) + x_{\text{QP}}(T, P_{\text{abs}}) \tag{2.23}$$

$$\delta Q_i^{-1}(T, P_{\text{abs}}) = \delta Q_{\text{TLS}}^{-1}(T) + \delta Q_{\text{QP}}^{-1}(T, P_{\text{abs}}), \tag{2.24}$$

where $x_{\text{TLS}}(T)$ is the fractional frequency shift due to TLSs in the capacitor, $x_{\text{QP}}(T, P_{\text{abs}})$ is the fractional frequency shift due to the QP density in the inductor, $\delta Q_{\text{TLS}}^{-1}(T)$ is the inverse quality factor shift due to TLSs in the capacitor, and $\delta Q_{\text{QP}}^{-1}(T, P_{\text{abs}})$ is the inverse quality factor shift due to the QP density in the inductor. The parameters $x_{\text{QP}}(T, P_{\text{abs}})$, $\delta Q_{\text{QP}}^{-1}(T, P_{\text{abs}})$, $x_{\text{TLS}}(T)$, and $\delta Q_{\text{TLS}}^{-1}(T)$ are derived in this subsection. Subsection 2.4.3 is the derivation of the detector noise due to fluctuations in x and δQ_i^{-1}.

Complex impedance of a KID

The complex conductivity of a KID is calculated in detail in Gao et al. 2008[17] using the Mattis-Bardeen theory. A variation of this derivation is presented here. The complex conductivity $\sigma(\omega)$ is

$$\sigma(\omega) = \sigma_1(\omega) - j\sigma_2(\omega). \tag{2.25}$$

The charge carriers in a superconductor consist of Cooper pairs and QPs. An excess population of QPs can be described by the modified Fermi-Dirac distribution

$$f(E, \mu^*, T) = \frac{1}{e^{(E-\mu^*)/k_B T} + 1}, \tag{2.26}$$

where the effective chemical potential μ^* is introduced to account for QPs created by absorbed radiation. This formulation is valid at low temperatures where phonons with energy less than 2Δ dominate, and therefore the timescale for excess QPs to thermalize with the lattice temperature is much shorter than the recombination time.[17] Note that the QP distribution can also be significantly affected by the absorbed microwave readout power, as described in a series of articles.[21,28,43,48,49] The superconducting gap is denoted by Δ and takes on the value

$$\Delta_0 = 1.76 k_B T_c \tag{2.27}$$

at T = 0.[53] The Mattis-Bardeen theory is used to calculate the ratio of the complex conductivity components to the normal conductivity σ_n.[33] For $\hbar\omega \ll \Delta$, the Mattis-Bardeen integrals are

$$\frac{\sigma_1}{\sigma_n} = \frac{2}{\hbar\omega}\int_{\Delta}^{\infty} dE \frac{E^2+\Delta^2+\hbar\omega E}{\sqrt{E^2-\Delta^2}\sqrt{(E+\hbar\omega)^2-\Delta^2}}\left[f(E)-f(E+\hbar\omega)\right] \tag{2.28}$$

$$\frac{\sigma_2}{\sigma_n} = \frac{1}{\hbar\omega}\int_{\Delta}^{\Delta+\hbar\omega} dE \frac{E^2+\Delta^2-\hbar\omega E}{\sqrt{E^2-\Delta^2}\sqrt{\Delta^2-(E-\hbar\omega)^2}}\left[1-2f(E)\right]. \tag{2.29}$$

The QP density is given by

$$n_{\mathrm{QP}} = 4N_0\int_{\Delta}^{\infty}\frac{Ef(E)}{\sqrt{E^2-\Delta^2}}dE, \tag{2.30}$$

where N_0 is the single-spin density of electron states at the Fermi energy level. The gap energy is given by

$$\frac{\Delta_0-\Delta}{\Delta_0} = 2\int_{\Delta}^{\infty}\frac{f(E)}{\sqrt{E^2-\Delta^2}}dE. \tag{2.31}$$

Equations 2.28, 2.29, 2.30, and 2.31 can be calculated numerically. However, most KIDs will obey the operational conditions that $k_BT \ll \Delta$ and $e^{-(E-\mu^*)/K_BT} \ll 1$, for which the integrals can be approximated. For KIDs operating at temperatures below T_c, $k_BT \ll \Delta$ is satisfied. The change in QP density from a pair-breaking photon can be estimated by $\Delta n_{\mathrm{QP}} \approx \eta_{\mathrm{pb}} h\nu_{\mathrm{photon}}/\Delta_0 V$. For low-volume (~20 µm^3) Al KIDs operating at wavelengths as short as 25 µm at $T > 1$ mK, $e^{(E-\mu^*)/k_BT} < 4\times10^{-5}$. Therefore, all three conditions for the approximation are met for the KIDs studied in this thesis, and the following equations, calculated in Gao 2008,[17] describe the QP behavior:

$$n_{\mathrm{QP}} = 2N_0\sqrt{2\pi k_BT\Delta}e^{-(\Delta-\mu^*)/k_BT} \tag{2.32}$$

$$\frac{\Delta}{\Delta_0} = 1-\frac{n_{\mathrm{QP}}}{2N_0\Delta} \tag{2.33}$$

$$\frac{\sigma_1}{\sigma_n} = \frac{4\Delta}{\hbar\omega}e^{-(\Delta-\mu^*)/k_BT}\sinh(\xi)K_0(\xi) \tag{2.34}$$

$$\frac{\sigma_2}{\sigma_n} = \frac{\pi\Delta}{\hbar\omega}\left[1-2e^{-(\Delta-\mu^*)/k_BT}e^{-\xi}I_0(\xi)\right], \tag{2.35}$$

where $\xi = \hbar\omega/2k_BT$. Using Equations 2.32 and 2.33 to suppress the explicit dependence on Δ and μ^* and keeping only first-order terms, the complex conductivity becomes

$$\frac{\sigma_1}{\sigma_n} = \frac{\pi n_{\mathrm{QP}}(T)}{2\hbar\omega N_0}S_1(T) \tag{2.36}$$

$$\frac{\sigma_2}{\sigma_n} = \frac{\pi\Delta_0}{2\hbar\omega}\left[1-\frac{n_{\mathrm{QP}}(T)}{2N_0\Delta_0}S_2(T)\right], \tag{2.37}$$

where $S_1(T)$ and $S_2(T)$ are

$$S_1(T) = \frac{2}{\pi}\sqrt{\frac{2\Delta_0}{\pi k_B T}}\sinh(\xi)K_0(\xi) \tag{2.38}$$

$$S_2(T) = 1 + \sqrt{\frac{2\Delta_0}{\pi k_B T}}e^{-\xi}I_0(\xi) \tag{2.39}$$

and I_n and K_n are the nth-order modified Bessel functions of the first and second kind, respectively.

Changes in the surface impedance of the superconducting film $Z_s(\omega, T, P_{\text{abs}}) = R_s + jX_s$ are related to changes in the complex conductivity through[17]

$$\frac{\delta Z_s}{Z_s} = \gamma\frac{\delta\sigma}{\sigma}, \gamma = \begin{cases} -1/2 & \text{thick film, local limit} \\ -1/3 & \text{thick film, extreme anomalous limit} \\ 1 & \text{thin film, local limit.} \end{cases} \tag{2.40}$$

In the limit where $T = 0$ and $P_{\text{abs}} = 0$, $R_s = 0$ and $\sigma_1 = 0$, so the relation becomes

$$\frac{\delta Z_s}{Z_s} = \frac{\delta R_s + jX_s}{jX_s(T = 0, P_{\text{abs}} = 0)} = \gamma\frac{\delta\sigma_1 - j\delta\sigma_2}{-\sigma_2(T = 0, P_{\text{abs}} = 0)}. \tag{2.41}$$

It follows that the frequency fractional frequency shift $x(T, P_{\text{abs}})$ is

$$x(T, P_{\text{abs}}) = -\frac{\gamma\alpha}{2}\frac{\sigma_2(T, \mu^*) - \sigma_2(T = 0, \mu^* = 0)}{\sigma_2(T = 0, \mu^* = 0)} \tag{2.42}$$

and the inverse quality factor shift $\delta Q_i^{-1}(T, P_{\text{abs}})$ is

$$\delta Q_i^{-1}(T, P_{\text{abs}}) = \gamma\alpha\frac{\sigma_1(T, \mu^*) - \sigma_1(T = 0, \mu^* = 0)}{\sigma_2(T = 0, \mu^* = 0)}, \tag{2.43}$$

where $\alpha = L_k/L$ is the kinetic inductance fraction, L_k is the kinetic inductance, and L is the total inductance. Combining Equations 2.36 and 2.37 with 2.42 and 2.43 yields

$$x_{\text{QP}}(T, P_{\text{abs}}) = -\frac{\gamma\alpha}{4N_0\Delta_0}S_2(T)n_{\text{QP}}(T, P_{\text{abs}}) \tag{2.44}$$

$$\delta Q_{\text{QP}}^{-1}(T, P_{\text{abs}}) = -\frac{\gamma\alpha}{2N_0\Delta_0}S_1(T)n_{\text{QP}}(T, P_{\text{abs}}). \tag{2.45}$$

The number of QPs N_{QP} evolves according to

$$\frac{\partial N_{\text{QP}}}{\partial t} = \Gamma_g^{\text{th}} + \Gamma_g^{\text{opt}} + \Gamma_g^{\mu\text{w}} - \Gamma_r, \tag{2.46}$$

where Γ_g^{th} is the thermal QP generation rate, Γ_g^{opt} is the absorbed power QP generation rate, $\Gamma_g^{\mu\text{W}}$ is the microwave power generation rate, and Γ_r is the recombination rate. The optical power that is absorbed in the detector is

$$\eta_{\text{pb}} P_{\text{abs}} = \Gamma_g^{\text{opt}} \Delta_0, \tag{2.47}$$

where η_{pb} is the pair-breaking efficiency, or the fraction of the absorbed power which is converted into QPs. Similarly, the microwave power that is absorbed is

$$\eta_{\mu\text{W}} P_{\mu\text{W}} = \Gamma_g^{\mu\text{W}} \Delta_0, \tag{2.48}$$

where $\eta_{\mu\text{W}}$ is the efficiency with which absorbed microwave power produces QPs. Empirically, the recombination time of equilibrium QPs τ_r can be written as[6]

$$\frac{1}{\tau_r} = \frac{1}{\tau_{\text{max}}} + 2R n_{\text{QP}}, \tag{2.49}$$

where R is the recombination constant given by

$$R = \left(\frac{2\Delta}{k_B T_c} \right)^3 \frac{1}{4 N_0 \Delta \tau_0}. \tag{2.50}$$

Equation 2.50 was derived in Kaplan et al. 1976, where the material-dependent constant τ_0 was calculated to be 438 ns for Al.[24] Fitting τ_{QP} versus temperature with no absorbed power is often the best way to determine R and τ_0.[11] τ_{max} is an experimentally measured saturation lifetime that is not fully understood, though it has been suggested that it may be due to QP trapping.[41] For small perturbations from equilibrium, non-equilibrium QPs recombine according to an exponential law with time constant

$$\tau_{\text{QP}} = \frac{\tau_{\text{max}}}{1 + n_0/n^*}, \tag{2.51}$$

where $n^* = 1/(4R\tau_{\text{max}})$ and n_0 is the equilibrium QP density. The recombination rate can then be written as

$$\Gamma_r = \frac{n_{\text{QP}} V}{\tau_{\text{max}}} \left(1 + \frac{n_{\text{QP}}}{2n^*} \right). \tag{2.52}$$

The thermal QP distribution in equilibrium with no absorbed power is defined as $n_{\text{th}} = n_{\text{QP}}(P_{\text{abs}} = 0)$, and can be calculated from Equation 2.32 with $\mu = 0$. In the common operational condition where $T \ll T_c$, Δ can be approximated by Δ_0. The thermal generation rate is

$$\Gamma_g^{\text{th}} = \frac{n_{\text{th}} V}{\tau_{\text{max}}} \left(1 + \frac{n_{\text{th}}}{2n^*} \right) \tag{2.53}$$

and thus the time derivative of the QP density is

$$\frac{\partial n_{\mathrm{QP}}}{\partial t} = -\frac{V}{2\tau_{\mathrm{max}} n^*}\Bigg[n_{\mathrm{th}}\left(2n^* + n_{\mathrm{th}}\right) - n_{\mathrm{QP}}\left(2n^* + n_{\mathrm{QP}}\right) + \frac{2n^*\tau_{\mathrm{max}}}{\Delta_0 V}\left(\eta_{\mathrm{pb}} P_{\mathrm{abs}} + \eta_{\mu\mathrm{W}} P_{\mu\mathrm{W}}\right)\Bigg]. \tag{2.54}$$

In equilibrium, the QP density rate equation yields

$$n_{\mathrm{QP}} = -n^* + \sqrt{(n^* + n_{\mathrm{th}})^2 + \frac{2\tau_{\mathrm{max}}}{\Delta_0 V}\left(\eta_{\mathrm{pb}} P_{\mathrm{abs}} + \eta_{\mu\mathrm{W}} P_{\mu\mathrm{W}}\right)}. \tag{2.55}$$

Two-level systems in KIDs

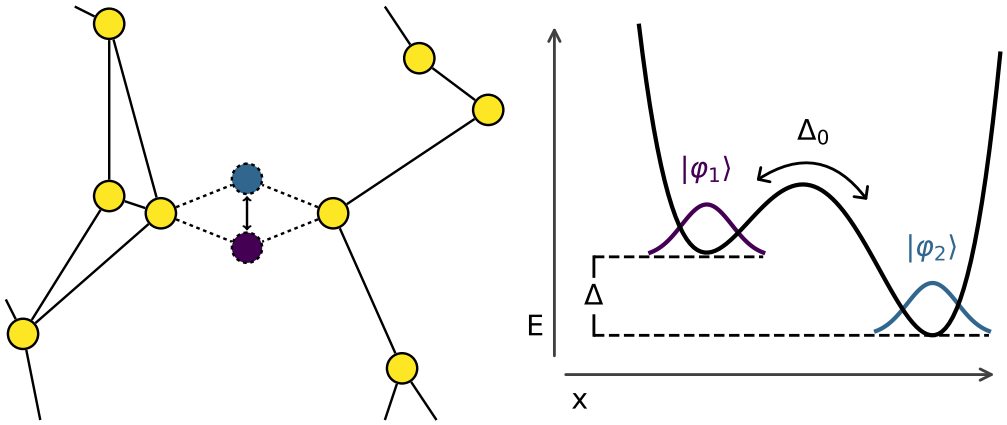

Figure 2.2: (Left) Illustration of a single-atom TLS in an amorphous material structure. The yellow circles represent atoms that have only minor perturbations to their positions in the structure, and the purple and blue circles represent the positions of a single atom with two nearly degenerate energy configurations, corresponding to the potentials in the plot on the right. (Right) Diagram of the TLS potential and wavefunctions. The black curve is the potential, with the two minima representing the two energy levels of the TLS. The energy asymmetry between the levels is Δ and the tunnel splitting is Δ_0.

Amorphous materials contain TLSs: atoms or groups of atoms that have two nearly degenerate states. A depiction of a single-atom TLS is shown in Figure 2.2 (left). A distribution of TLSs that couple to the electric field of a resonator produce 1/f-type fluctuations in the resonant frequency. TLS noise has been observed in KIDs since early experiments.[12,20] TLSs are also a dominant source of decoherence in

superconducting qubits.[32] In addition to noise, TLSs also produce a temperature-dependent dielectric loss and frequency shift in superconducting microresonators.

Most KIDs use capacitor architectures that do not require deposited amorphous materials. However, TLSs are also present in native oxides or other amorphous materials present on the substrates of the device.[19] This subsection details the fractional frequency shift and dielectric loss due to TLSs, following work in the 1970s and 1980s exploring the low-temperature properties of glasses.[5,40] Though much progress on a theory of TLS noise has been made since the first observations, several aspects of the theory are still unresolved. TLS noise models will be discussed in Subsection 2.4.3.

A TLS can be modelled as two harmonic potentials with an intervening barrier, as shown in Figure 2.2 (right). The effective Hamiltonian considers only the lowest-energy states $|\varphi_1\rangle$ and $|\varphi_2\rangle$ at each of the minima and is given by[40]

$$\mathcal{H} = -\frac{1}{2}\Delta\hat{\sigma}_z + \frac{1}{2}\Delta_0\hat{\sigma}_x, \tag{2.56}$$

where $\hat{\sigma}_x$ and $\hat{\sigma}_z$ are the Pauli matrices, Δ is the difference in the potential minima, and Δ_0 is the tunneling splitting, corresponding to the tunneling rate $\Delta_0/\hbar$, which is exponentially sensitive to the barrier height. The TLS will couple to the electric field $\vec{\mathcal{E}}$ through the dipole moment $\vec{p}_{\mathrm{TLS}}$ and to the strain tensor. The coupling to the strain provides a means for absorption or emission of phonons, and the coupling to the electric field provides a means for the TLS to influence the resonator. These couplings result in a modification to the tunnelling rate, while the energy difference of the potential minima is generally not affected.[40] The eigenstates of the TLS Hamiltonian are expressed in terms of $|\varphi_1\rangle$ and $|\varphi_2\rangle$ as

$$|\psi_+\rangle = \sin(\theta)\,|\varphi_1\rangle + \cos(\theta)\,|\varphi_2\rangle \tag{2.57}$$

$$|\psi_-\rangle = \cos(\theta)\,|\varphi_1\rangle - \sin(\theta)\,|\varphi_2\rangle\,, \tag{2.58}$$

where the mixing angle θ is given by

$$\tan(2\theta) = \frac{\Delta_0}{\Delta} \tag{2.59}$$

and the eigenvalues are

$$E_\pm = \pm\frac{1}{2}\sqrt{\Delta^2 + \Delta_0^2}. \tag{2.60}$$

The transition frequency ω_{TLS} is calculated from the energy difference between the two eigenstates, $E_+ - E_-$, to be

$$\hbar\omega_{\mathrm{TLS}} = \sqrt{\Delta^2 + \Delta_0^2}. \tag{2.61}$$

If TLSs are excited to their upper state, they will relax with an average rate $\Gamma_1(T)$ due to phonon interactions. Additionally, the phase coherence of the TLSs will decay due to random fluctuations in the electric field and the strain, e.g., produced by nearby fluctuating TLSs. The total coherence decay Γ_2 is

$$\Gamma_2(T) = \frac{1}{2}\Gamma_1(T) + \Gamma_\phi(T). \tag{2.62}$$

The rate of TLS excitation will increase with increasing electric field, increasing the population of the upper state, until a critical field $|\vec{\vec{\mathcal{E}}}_{\mathrm{crit}}|$ is reached. Considering relaxation processes, Gao shows that the ensemble average of the spin operators evolves with a form that can be described by the Bloch equations, which can be solved and integrated over the TLS asymmetry, tunnel splitting, and dipole orientation to yield a dielectric loss tangent for $|\vec{E}| \ll |\vec{\vec{\mathcal{E}}}_{\mathrm{crit}}|$ of[17]

$$\delta_{\mathrm{TLS}} = \delta_0 \tanh(\xi), \tag{2.63}$$

where $\xi = \hbar\omega/2k_BT$, $\delta_0 = \pi P_0 d/3\epsilon$ is the dielectric loss tangent, P_0 is the TLS spectral and spatial density, d is the mean dipole moment, and ϵ is the dielectric constant of the TLS host material. The hyperbolic tangent can be recognized to arise from the thermal occupation probabilities of the two quantum states. The critical field is given by[32]

$$|\vec{\mathcal{E}}_{\mathrm{crit}}| = \frac{\sqrt{3}\hbar}{2d}\sqrt{\Gamma_1(T)\Gamma_2(T)}, \tag{2.64}$$

such that the critical power scales as

$$P_{\mathrm{crit}}(T) \propto \Gamma_1(T)\Gamma_2(T). \tag{2.65}$$

Thus, the dielectric loss, accounting for saturation, is

$$\boxed{\delta_{\mathrm{TLS}} = \frac{\delta_0 \tanh(\xi)}{\sqrt{1 + \frac{P_{\mu\mathrm{W}}}{P_{\mathrm{crit}}(T)}}}.} \tag{2.66}$$

The temperature dependence of $\Gamma_1(T)$ and $\Gamma_2(T)$ will be discussed in Subsection 2.4.3.

Assume that the TLS are uniformly distributed in a host material of volume V_h with dielectric constant ϵ_h, and the total resonator volume is V with dielectric constant ϵ. The ratio of electrical energy stored in the TLS (E_{TLS}) to the total electrical energy stored in the resonator (E_{total}), referred to as the filling factor F, is[19]

$$F = \frac{E_{\text{TLS}}}{E_{\text{total}}} = \frac{\int_{V_h} \epsilon_h \vec{\mathcal{E}}(\vec{r})^2 d\vec{r}}{\int_V \epsilon \vec{\mathcal{E}}(\vec{r})^2 d\vec{r}}. \tag{2.67}$$

For an ideal parallel-plate capacitor, the dielectric fills the entire volume of the electric field and the electric field is constant with $\vec{r}$, so the filling factor is 1. For an interdigitated (IDC) capacitor, the filling factor is geometry dependent and typically scales as $F \propto 1/w$, where w is the line thickness.[19] The effect of the TLSs on the quality factor is

$$Q_{\text{TLS}}^{-1}(T) = F\delta_{\text{TLS}}(T). \tag{2.68}$$

The fractional frequency shift from the TLSs is also calculated from the Bloch equations to be[17]

$$x_{\text{TLS}}(T) = \frac{1}{\pi} F\delta_0 \,\text{Re}\left\{\Psi\left(\frac{1}{2} + \frac{j\xi}{\pi}\right) - \ln\left(\frac{\xi}{\pi}\right)\right\}, \tag{2.69}$$

where Ψ is the complex digamma function. The tails of the TLS reactive response drop off more slowly with frequency than the dissipative response, so in general the fractional frequency shift is caused by a distribution of TLS that extend further in frequency than TLS that contribute to the dielectric loss. Therefore, microwave power saturation of TLSs has a significant effect on the dielectric loss, but a minimal effect on fractional frequency shift. The power dependence of Equation 2.69 is calculated in Gao et al. 2008,[17] but omitted here because it is negligible for the data presented in this thesis.

The fractional frequency shift of a superconducting resonator as a function of temperature is dominated by the TLSs at low temperatures, and the Mattis-Bardeen variation of σ_2 at high temperatures. The crossover of these two effects for the KIDs studied in this thesis occurs at their typical operating temperature ($\sim 100-150$ mK), so they are, to first order, insensitive to temperature fluctuations.

2.4.2 Response

The resonance parameters x and δQ^{-1} respond to absorbed power through changes in the QP density. The derivatives of Equations 2.44 and 2.45 with respect to P_{abs} are

$$\frac{\partial x_{\mathrm{QP}}(T, P_{\mathrm{abs}})}{\partial P_{\mathrm{abs}}} = -\frac{\gamma\alpha}{4N_0\Delta_0} S_2(T) \frac{\partial n_{\mathrm{QP}}(T, P_{\mathrm{abs}})}{\partial P_{\mathrm{abs}}} \tag{2.70}$$

$$\frac{\partial \delta Q_{\mathrm{QP}}^{-1}(T, P_{\mathrm{abs}})}{\partial P_{\mathrm{abs}}} = -\frac{\gamma\alpha}{2N_0\Delta_0} S_1(T) \frac{\partial n_{\mathrm{QP}}(T, P_{\mathrm{abs}})}{\partial P_{\mathrm{abs}}}, \tag{2.71}$$

where the derivative of the QP density with respect to P_{abs} is

$$\frac{\partial n_{\mathrm{QP}}}{\partial P_{\mathrm{abs}}}(\nu = 0) = \frac{n^*\tau_{\mathrm{max}}}{\Delta_0 V}\left[(n^* + n_{\mathrm{th}})^2 + \frac{2n^*\tau_{\mathrm{max}}}{\Delta_0 V}\left(\eta_{\mathrm{pb}} P_{\mathrm{abs}} + \eta_{\mu\mathrm{W}} P_{\mu\mathrm{W}}\right)\right]^{-\frac{1}{2}}. \tag{2.72}$$

Note that, in addition to the rolloff due to the QP lifetime, the measured resonator response (e.g., the forward complex transmission S_{21}) is further modified by the resonator ring-down time. For the arrays measured in this thesis, the rolloff due to the resonator ring-down occurs at much higher frequencies than the rolloff due to the QP lifetime. The effect of an AC perturbation at frequency ν in the absorbed optical power P_{abs} leads to changes in the resonant frequency and quality factor given by

$$\frac{\partial x_{\mathrm{QP}}(T, P_{\mathrm{abs}}, \nu)}{\partial P_{\mathrm{abs}}} = S_2(T) \frac{-R_0(T)/2}{\sqrt{1 + \eta_{\mathrm{pb}} P_{\mathrm{abs}}/P_0(T)}} \frac{1}{\sqrt{1 + (2\pi\nu\tau_{\mathrm{QP}})^2}} \tag{2.73}$$

$$\frac{\partial \delta Q_{\mathrm{QP}}^{-1}(T, P_{\mathrm{abs}}, \nu)}{\partial P_{\mathrm{abs}}} = S_1(T) \frac{-R_0(T)}{\sqrt{1 + \eta_{\mathrm{pb}} P_{\mathrm{abs}}/P_0(T)}} \frac{1}{\sqrt{1 + (2\pi\nu\tau_{\mathrm{QP}})^2}}, \tag{2.74}$$

where

$$R_0(T) = \frac{\gamma\alpha}{2N_0\Delta_0}\sqrt{\frac{n^*\tau_{\mathrm{max}}}{2\Delta_0 V P_0}} \tag{2.75}$$

$$P_0(T) = \frac{\Delta_0 V}{2\tau_{\mathrm{max}}} \frac{(n^* + n_{\mathrm{th}}(T))^2}{n^*} + \eta_{\mu\mathrm{W}} P_{\mu\mathrm{W}}. \tag{2.76}$$

2.4.3 Noise

Noise arises in both the inductor and the capacitor of the KID resonant circuit. In the inductor, the primary noise source is fluctuations in the QP population, where QPs can be excited thermally, by absorbed light, or by absorbed microwave power.

In the capacitor, the primary noise source is dielectric permittivity fluctuations due to TLSs.

Up to this point, the instantaneous fractional frequency shift $x = (f - f_r)/f_r$ and inverse quality factor $A = \delta Q_i^{-1}$ have been the primary quantities of interest. In practice, these quantities will be probed through the transmission S_{21}, so the fluctuations in the measurement can be written as

$$\delta x_{\text{inferred}} = \delta S_{21} \left(\frac{\partial S_{21}}{\partial x} \right)^{-1} \tag{2.77}$$

$$\delta A_{\text{inferred}} = \delta S_{21} \left(\frac{\partial S_{21}}{\partial A} \right)^{-1}, \tag{2.78}$$

where $\delta x_{\text{inferred}}$ is the fluctuation in the inferred fractional frequency shift x_{inferred}, $\delta A_{\text{inferred}}$ is the fluctuation in the inferred inverse quality factor $A_{\text{inferred}} = \delta Q^{-1}_{i,\text{inferred}}$, and δS_{21} is the fluctuation in S_{21}. Therefore, the measured noise and response of the inferred quantities will be filtered through the resonator by a transfer function, which generally depends on the detuning of the probe tone from the resonant frequency. For zero detuning (a typical observing condition for KIDs, see Appendix E), the transfer function is a single-pole low-pass filter with time constant $\tau_{\text{rd}} = Q_r/\pi f_r$, referred to as the resonator ring-down time. For the KIDs studied in this thesis $\tau_{\text{rd}} \ll \tau_{\text{QP}}$. Hereafter, the subscript in x_{inferred} and A_{inferred} will be dropped, noting that the resonator ring-down must be accounted for unless $2\pi\nu \ll 1/\tau_{\text{rd}}$. The PSD of fluctuations in the fractional frequency shift can be written as

$$S_{xx}(\nu) = \left| \frac{\partial S_{21}}{\partial x} \right|^{-2} S^{\text{amp}}(\nu) + \frac{1}{1 + (2\pi\nu\tau_{\text{rd}})^2} \left[S_{xx}^{\text{TLS}}(\nu) + S_{xx}^{\text{QP}}(\nu) \right], \tag{2.79}$$

where $S^{\text{amp}}(\nu)$ is the PSD of the amplifier noise, $S_{xx}^{\text{TLS}}(\nu)$ is the PSD of TLS noise, and $S_{xx}^{\text{QP}}(\nu)$ is the PSD of QP noise. Similarly, the dissipative noise S_{aa} is

$$S_{aa}(\nu) = \left| \frac{\partial S_{21}}{\partial \delta Q_i^{-1}} \right|^{-2} S^{\text{amp}}(\nu) + \frac{1}{1 + (2\pi\nu\tau_{\text{rd}})^2} S_{aa}^{\text{QP}}(\nu), \tag{2.80}$$

where the TLS term is dropped because TLS noise is only observed in the fractional frequency direction. The PSDs of the amplifier, TLS, and QP noise are derived in the following subsections.

Amplifier noise

Amplifier noise affects the measurement of the resonator complex forward transmission S_{21}. The PSD of the noise added to each of the quadratures is given by

$$S^{\text{amp}}(\nu) = \frac{k_B T_n}{P_{\mu\text{W}}}, \tag{2.81}$$

where $P_{\mu\text{W}}$ is the microwave readout power at the input to the resonator and T_n is the amplifier noise temperature referred to the resonator output, which accounts for any losses or thermal noise due to the intervening cabling.

QP noise

The time-dependent QP equation is

$$\frac{\partial N_{\text{QP}}}{\partial t} = \Gamma_g(t) - \Gamma_r(n_{\text{QP}}(t), t). \tag{2.82}$$

For small deviations, the generation and recombination rates are

$$\Gamma_g(t) = \Gamma_g(0) + \delta\Gamma_g(t) \tag{2.83}$$

$$\Gamma_r(t) = \Gamma_r(0) + \delta\Gamma_r(t) + \frac{\partial \Gamma_r}{\partial N_{\text{QP}}}\delta N_{\text{QP}}(t), \tag{2.84}$$

and the QP equation becomes

$$\frac{\partial \delta N_{\text{QP}}}{\partial t} = \delta\Gamma_g(t) - \delta\Gamma_r(t) - \frac{\partial \Gamma_r}{\partial N_{\text{QP}}}\delta N_{\text{QP}}(t) = \tag{2.85}$$

$$= \delta\Gamma_g(t) - \delta\Gamma_r(t) - \frac{\delta N_{\text{QP}}(t)}{\tau_{\text{QP}}}, \tag{2.86}$$

where $\partial\Gamma_r/\partial N_{\text{QP}}$ is calculated from Equation 2.52. The Fourier transform of this equation is

$$\delta\widetilde{N}_{\text{QP}}(\nu) = \frac{\tau_{\text{QP}}}{1 + j2\pi\nu\tau_{\text{QP}}}\left[\delta\Gamma_g(\nu) - \delta\Gamma_r(\nu)\right]. \tag{2.87}$$

From Equations 2.44 and 2.45, the perturbations in x and Q_i^{-1} are

$$\delta x(T, P_{\text{abs}}, \nu) = -\frac{\gamma\alpha}{4N_0\Delta_0 V} S_2(T) \frac{\tau_{\text{QP}}}{1 + j2\pi\nu\tau_{\text{QP}}}\left[\delta\Gamma_g(\nu) - \delta\Gamma_r(\nu)\right] \tag{2.88}$$

$$\delta Q_i^{-1}(T, P_{\text{abs}}, \nu) = -\frac{\gamma\alpha}{2N_0\Delta_0 V} S_1(T) \frac{\tau_{\text{QP}}}{1 + j2\pi\nu\tau_{\text{QP}}}\left[\delta\Gamma_g(\nu) - \delta\Gamma_r(\nu)\right] \tag{2.89}$$

and the PSDs are

$$S_{xx}^{\mathrm{QP}}(\nu) = \left[\frac{\gamma\alpha}{4N_0\Delta_0 V}S_2(T)\right]^2 \frac{\tau_{\mathrm{QP}}^2}{1+(2\pi\nu\tau_{\mathrm{QP}})^2}\left[S_g(\nu)+S_r(\nu)\right] \tag{2.90}$$

$$S_{aa}^{\mathrm{QP}}(\nu) = \left[\frac{\gamma\alpha}{2N_0\Delta_0 V}S_1(T)\right]^2 \frac{\tau_{\mathrm{QP}}^2}{1+(2\pi\nu\tau_{\mathrm{QP}})^2}\left[S_g(\nu)+S_r(\nu)\right], \tag{2.91}$$

where $S_g(\nu)$ is the PSD of $\delta\Gamma_g(\nu)$ and $S_r(\nu)$ is the PSD of $\delta\Gamma_r(\nu)$. The thermal and photon-induced recombination noise terms can be treated simultaneously, but it is convenient to separate generation noise into the thermal generation PSD $S_g^{\mathrm{th}}(\nu)$ and the scaled photon-induced generation PSD $S_g^{\mathrm{photon}}(\nu)$, such that the PSDs become

$$S_{xx}^{\mathrm{QP}}(\nu) = \frac{1}{1+(2\pi\nu\tau_{\mathrm{QP}})^2}\left\{\left[\frac{\gamma\alpha\tau_{\mathrm{QP}}}{4N_0\Delta_0 V}S_2(T)\right]^2\left[S_g^{\mathrm{th}}(\nu)+S_r(\nu)\right]+S_g^{\mathrm{photon}}(\nu)\right\} \tag{2.92}$$

$$S_{aa}^{\mathrm{QP}}(\nu) = \frac{1}{1+(2\pi\nu\tau_{\mathrm{QP}})^2}\left\{\left[\frac{\gamma\alpha\tau_{\mathrm{QP}}}{2N_0\Delta_0 V}S_1(T)\right]^2\left[S_g^{\mathrm{th}}(\nu)+S_r(\nu)\right]+S_g^{\mathrm{photon}}(\nu)\right\}. \tag{2.93}$$

Recombination is a Poissonian process, and thus has a PSD given by

$$S_r(\nu) = 4\left(\Gamma_r^2\delta(\nu)+\Gamma_r\right), \tag{2.94}$$

where one factor of 2 is introduced to convert to the unilateral PSD and a second factor of 2 accounts for the fact that two QPs combine in each recombination event. Then, from Equation 2.52,

$$S_r(\nu) = \frac{4n_{\mathrm{QP}}V}{\tau_{\mathrm{max}}}\left(1+\frac{n_{\mathrm{QP}}}{2n^*}\right) \tag{2.95}$$

for $\nu > 0$. The thermal QP generation PSD can be calculated in the same way as the recombination PSD using Equation 2.53, and is thus

$$S_g^{\mathrm{th}}(\nu) = \frac{4n_{\mathrm{th}}V}{\tau_{\mathrm{max}}}\left(1+\frac{n_{\mathrm{th}}}{2n^*}\right) \tag{2.96}$$

for $\nu > 0$.

The photon noise can be expressed as in Equation 2.96, where the thermal QP density n_{th} is replaced by the absorbed power dependent QP density $n_{\mathrm{QP}}^{\mathrm{opt}}$. Because the calculation of $n_{\mathrm{QP}}^{\mathrm{opt}}$ is not trivial, the photon noise term can instead be derived from the photon NEP. Using Equation 2.5,

$$S_g^{\mathrm{photon}}(\nu) = R(T,P_{\mathrm{abs}},\nu)^2\mathrm{NEP}_{\mathrm{photon}}^2 = \tag{2.97}$$

$$= R(T,P_{\mathrm{abs}},\nu)^2 2h\nu_{\mathrm{photon}}P_{\mathrm{abs}}, \tag{2.98}$$

where $R(T, P_{\mathrm{abs}}, \nu) = \partial x_{\mathrm{QP}}/\partial P_{\mathrm{abs}}(T, P_{\mathrm{abs}}, \nu)$ for fractional frequency noise and $R(T, P_{\mathrm{abs}}, \nu) = \partial \delta Q_{\mathrm{QP}}^{-1}/\partial P_{\mathrm{abs}}(T, P_{\mathrm{abs}}, \nu)$ for dissipation noise. The responsivities are given in Equations 2.73 and 2.74. The QP noise is thus

$$S_{xx}^{\mathrm{QP}}(\nu, P_{\mathrm{abs}}, T) = \left[\frac{\gamma\alpha}{4N_0\Delta_0}S_2(T)\right]^2 \frac{2\tau_{\mathrm{max}}n^*}{V} \times \frac{\left[n_{\mathrm{QP}}(P_{\mathrm{abs}}, T) + 2n^*\right] n_{\mathrm{QP}}(P_{\mathrm{abs}}, T) + \left[n_{\mathrm{th}}(T) + 2n^*\right] n_{\mathrm{th}}(T)}{\left[n_{\mathrm{QP}}(P_{\mathrm{abs}}, T) + n^*\right]^2} + \left[\frac{\partial x_{\mathrm{QP}}(T, P_{\mathrm{abs}}, \nu)}{\partial P_{\mathrm{abs}}}\right]^2 2h\nu_{\mathrm{photon}}P_{\mathrm{abs}} \tag{2.99}$$

$$S_{aa}^{\mathrm{QP}}(\nu, P_{\mathrm{abs}}, T) = \left[\frac{\gamma\alpha}{2N_0\Delta_0}S_1(T)\right]^2 \frac{2\tau_{\mathrm{max}}n^*}{V} \times \frac{\left[n_{\mathrm{QP}}(P_{\mathrm{abs}}, T) + 2n^*\right] n_{\mathrm{QP}}(P_{\mathrm{abs}}, T) + \left[n_{\mathrm{th}}(T) + 2n^*\right] n_{\mathrm{th}}(T)}{\left[n_{\mathrm{QP}}(P_{\mathrm{abs}}, T) + n^*\right]^2} + \left[\frac{\partial \delta Q_{\mathrm{QP}}^{-1}(T, P_{\mathrm{abs}}, \nu)}{\partial P_{\mathrm{abs}}}\right]^2 2h\nu_{\mathrm{photon}}P_{\mathrm{abs}}. \tag{2.100}$$

For $P_{\mathrm{abs}} = 0$, the QP noise becomes

$$S_{xx}^{\mathrm{QP}}(\nu, P_{\mathrm{abs}} = 0, T) = \left[\frac{\gamma\alpha}{4N_0\Delta_0}S_2(T)\right]^2 \frac{4\tau_{\mathrm{max}}}{V} n_{\mathrm{th}}(T)n^* \frac{n_{\mathrm{th}}(T) + 2n^*}{\left[n_{\mathrm{th}}(T) + n^*\right]^2} \tag{2.101}$$

$$S_{aa}^{\mathrm{QP}}(\nu, P_{\mathrm{abs}} = 0, T) = \left[\frac{\gamma\alpha}{2N_0\Delta_0}S_1(T)\right]^2 \frac{4\tau_{\mathrm{max}}}{V} n_{\mathrm{th}}(T)n^* \frac{n_{\mathrm{th}}(T) + 2n^*}{\left[n_{\mathrm{th}}(T) + n^*\right]^2}. \tag{2.102}$$

In the regime where the microwave-induced QP population is negligible compared to the thermal QP density, Equations 2.101 and 2.102 are referred to as the "thermal QP noise". Note that QP noise is sometimes called "generation-recombination noise" ("GR noise").

TLS noise

In addition to the temperature-dependent dielectric loss and fractional frequency shift produced by TLSs (discussed in Subsection 2.4.1), TLSs inject noise into the resonator through two processes: switching between the lower and upper states of the TLS and shifts in the energy levels of the TLS. Switching between states can be caused by emission or absorption of phonons. Shifts in the energy levels of the TLS can be caused by fluctuations in the strain, which are can be created by state switching in spatially neighboring TLSs, or dipole-dipole interactions between TLSs.

While the physical model of TLS noise is unresolved, its dependence on parameters of interest can be modelled empirically. The TLS noise can be written as

$$S_{xx}^{\mathrm{TLS}}(\nu, P_{\mu\mathrm{W}}, T) = \kappa_{\mathrm{geom}}\kappa_{\mathrm{dielectric}}\kappa_{\nu}(\nu)\kappa_{PT}(P_{\mu\mathrm{W}}, T), \tag{2.103}$$

where κ_{geom} is the geometry dependence, $\kappa_{\mathrm{dielectric}}$ is the dielectric material dependence, $\kappa_{\nu}(\nu)$ is the frequency dependence, and $\kappa_{PT}(P_{\mu\mathrm{W}}, T)$ is the microwave power and temperature dependence.

Geometry and Material: The empirically-modelled geometry dependence is

$$\kappa_{\mathrm{geom}} = \frac{\int_{V_h} |\vec{\mathcal{E}}(\vec{r})|^4 \left(|\vec{\mathcal{E}}(\vec{r})|^2 + |\mathcal{E}_{\mathrm{crit}}(T)|^2\right)^{-1/2} d\vec{r}}{4\left(\int_V \epsilon |\vec{\mathcal{E}}(\vec{r})|^2 d\vec{r}\right)^2}, \tag{2.104}$$

where V_h is the volume containing TLSs, V is the total resonator volume, $|\vec{\mathcal{E}}|$ is the electric field, and ϵ is the dielectric constant.[18]

This relation can be explored for the simplest case of a parallel-plate capacitor (PPC). For PPCs, the fringing fields are small, so $V = V_h$. Holding the energy stored in the capacitor constant, κ_{geom} is proportional to

$$\kappa_{\mathrm{geom}} \propto \begin{cases} \frac{1}{\sqrt{V}} & \mathrm{if} |\vec{\mathcal{E}}| \gg |\vec{\mathcal{E}_{\mathrm{crit}}}| \\ \frac{1}{V} & \mathrm{if} |\vec{\mathcal{E}}| \ll |\vec{\mathcal{E}}_{\mathrm{crit}}| \end{cases}. \tag{2.105}$$

Larger capacitors of a given architecture and capacitance exhibit lower TLS noise.

For coplanar waveguide (CPW) resonators, the combination of this model with experimental results are consistent with surface layer TLSs, and the TLS noise decreases rapidly with center strip width.[18] Motivated by this model, the switch to large geometry IDCs resulted in significant reductions in noise compared to CPWs.[38] PPCs have been historically avoided due to the high density of TLSs in common dielectrics, but recent research into dielectrics with low TLS density has reopened the possibility of using PPCs with KIDs.[39,14] For PPCs, the TLS noise is independent of the superconductor used for the capacitor plates, but depends on the TLS density in the dielectric. For IDCs, the TLSs are concentrated in surface layer oxides. Most elemental superconductors oxidize quickly in air, so TiN or NbTiN are often used due to their lower oxidation rates.[36]

Frequency ν: Because TLS switching is stochastic, their individual noise spectra are Lorentzian. Assume a distribution of TLS transition time constants given by

$$\rho(\tau) \propto \tau^{-\beta} \tag{2.106}$$

with individual spectra

$$S(\nu,\tau) = \frac{1}{1+(2\pi\tau\nu)^2}. \tag{2.107}$$

Superposing Lorentzians gives a total noise spectrum of[35,52]

$$S(\nu) = \int_{\tau_{\min}}^{\tau_{\max}} \rho(\tau) S(\nu,\tau) d\tau \propto \int_{\tau_{\min}}^{\tau_{\max}} \frac{\tau^{-\beta}}{1+(2\pi\tau\nu)^2} d\tau, \tag{2.108}$$

where $\tau_{\min}$ and $\tau_{\max}$ are the minimum and maximum TLS transition time constants, respectively. For frequencies well in the range of the minimum and maximum TLS transition time (valid for all practical KID applications[35]), and with the substitution $y = 2\pi\nu\tau$, the integral can be approximated as

$$S(\nu) \propto (2\pi\nu)^{-(\beta+1)} \int_0^{\infty} \frac{y^{-\beta}}{1+y^2} dy \propto \nu^{-(\beta+1)}. \tag{2.109}$$

The TLS fractional frequency PSD is therefore proportional to $\kappa_\nu(\nu)$, where

$$\kappa_\nu(\nu) = \nu^{-\alpha_\nu} \tag{2.110}$$

and $\alpha_\nu = \beta + 1$. Figure 2.3 is an illustration of how the Lorentzian noise spectra add to produce this behavior.

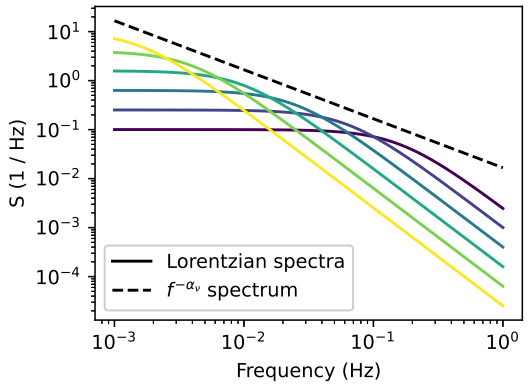

Figure 2.3: Distribution of Lorentzian noise spectra and their sum.

Power and temperature $P_{\mu W}$ and T: The power and temperature dependence of TLS noise has been measured for a number of geometries, and several models have been introduced to explain the measurements. Gao's original semiempirical model makes the ansatz that the noise scales similarly to the dielectric loss

$$\kappa_{PT}(P_{\mu W}, T) = \frac{\kappa_T(T)}{\sqrt{1+P_{\mu W}/P_{\text{crit}}(T)}}, \tag{2.111}$$

where the temperature dependence of $P_{\mathrm{crit}}(T)$ is determined by the temperature dependence of $\Gamma_1(T)$ and $\Gamma_2(T)$ through Equation 2.65 and $\kappa_T(T)$ is an additional temperature dependence. In the model which excludes interacting TLSs, referred to as the Standard Tunnelling Model (STM), the noise is expected to decrease at low temperatures as the TLSs in the energy range of $\hbar\omega$ freeze out, contrary to the observation that TLS noise increases with decreasing temperature down to $\sim$ 100 mK and only begins decreasing with decreasing temperature at very low temperatures.[31] More recent work calculates the temperature dependence of $\Gamma_1(T)$ and $\Gamma_2(T)$ while considering interactions between TLSs with energies of order $\hbar\omega$ and TLSs with much lower energy, referred to as two-level fluctuators (TLFs). Because the TLFs have lower energies, they can remain active down to much lower temperatures and interact with TLSs, which in turn couple to the resonator. This model is referred to as the General Tunnelling model (GTM), and it produces the temperature dependences $\Gamma_1(T) \propto T^{1+\mu}$, $\Gamma_2(T) \propto T^{1+\mu}$, and $\kappa_T(T) \propto 1/\Gamma_2(T)$ at low temperatures ($<$ 200 mK), where μ is a parameter related to the density of states of the TLSs $\rho(E) \propto E^{\mu}$ and E is the TLS energy splitting.[8] The GTM is a promising description of TLS noise at low temperatures in that it connects the temperature and power dependence to the TLS energy distribution, but it is difficult to distinguish from separate power laws in microwave power and temperature. For example, data from Kumar et al. 2008,[29] which covers a factor of 250 in power and 10 in temperature, can be described by either the GTM or power laws at temperatures below about 200 mK, but maintains a strong dependence on power at higher temperatures.

For the low-volume Al inductors studied in this thesis, the available power and temperature range over which noise can be measured is small, so simple power laws for the power and temperature dependence of TLS noise are sufficient to explain the observed data:

$$\kappa_{PT}(P_{\mu\mathrm{W}}, T) = T^{-\alpha_T} P_{\mu\mathrm{W}}^{-\alpha_P}, \tag{2.112}$$

where α_T and α_P are positive for the temperatures studied in this thesis.

Noise summary

In summary, the total PSDs are given by

$$S_{xx}(\nu) = S_{xx}^{\text{amp}} + \frac{1}{1+(2\pi\nu\tau_{\text{rd}})^2}\left[S_{xx}^{\text{TLS}}(\nu) + \frac{1}{1+(2\pi\nu\tau_{\text{QP}})^2} S_{xx}^{\text{QP}}\right] \tag{2.113}$$

$$S_{aa}(\nu) = S_{aa}^{\text{amp}} + \frac{1}{1+(2\pi\nu\tau_{\text{rd}})^2}\frac{1}{1+(2\pi\nu\tau_{\text{QP}})^2} S_{aa}^{\text{QP}}, \tag{2.114}$$

where

$$S_{xx}^{\text{amp}} = \left|\frac{\partial S_{21}}{\partial x}\right|^{-2} \frac{k_B T_n}{P_{\mu\text{W}}} \tag{2.115}$$

$$S_{aa}^{\text{amp}} = \left|\frac{\partial S_{21}}{\partial \delta Q_i^{-1}}\right|^{-2} \frac{k_B T_n}{P_{\mu\text{W}}} \tag{2.116}$$

$$S_{xx}^{\text{TLS}} = \kappa_{\text{material}}\kappa_{\text{geom}}\nu^{-\alpha_\nu}T^{-\alpha_T}P_{\mu\text{W}}^{-\alpha_P} \tag{2.117}$$

$$S_{xx}^{\text{QP}} = \left[\frac{\gamma\alpha}{4N_0\Delta_0}S_2\right]^2 \frac{2\tau_{\text{max}}n^*}{V}\frac{\left(n_{\text{QP}}+2n^*\right)n_{\text{QP}} + \left(n_{\text{th}}+2n^*\right)n_{\text{th}}}{\left(n_{\text{QP}}+n^*\right)^2} + \left[\frac{\partial x_{\text{QP}}}{\partial P_{\text{abs}}}\right]^2 2h\nu_{\text{photon}}P_{\text{abs}} \tag{2.118}$$

$$S_{aa}^{\text{QP}} = \left[\frac{\gamma\alpha}{2N_0\Delta_0}S_1\right]^2 \frac{2\tau_{\text{max}}n^*}{V}\frac{\left(n_{\text{QP}}+2n^*\right)n_{\text{QP}} + \left(n_{\text{th}}+2n^*\right)n_{\text{th}}}{\left(n_{\text{QP}}+n^*\right)^2} + \left[\frac{\partial \delta Q_{\text{QP}}^{-1}}{\partial P_{\text{abs}}}\right]^2 2h\nu_{\text{photon}}P_{\text{abs}}. \tag{2.119}$$

The NEPs for frequency readout (NEP_x) and amplitude readout (NEP_a) are given by

$$\text{NEP}_{\text{x}} = \left(\frac{\partial x}{\partial P_{\text{abs}}}\right)^{-1}\sqrt{S_{xx}} \tag{2.120}$$

$$\text{NEP}_a = \left(\frac{\partial \delta Q_i^{-1}}{\partial P_{\text{abs}}}\right)^{-1}\sqrt{S_{aa}}, \tag{2.121}$$

where the responsivities are given in Equations 2.73 and 2.74.

The QP fractional frequency shift PSD is often more useful in the alternate form in which Equation 2.51 is used to replace QP density terms with lifetimes, which can

be measured through fits to the PSD rolloff or single-photon events:

$$S_{xx}^{\mathrm{QP}} = \left[\frac{\gamma\alpha}{4N_0\Delta_0}S_2\right]^2 \frac{1}{2RV}\tau_{\mathrm{QP}}^2\left(\tau_{\mathrm{QP}}^{-2} + \tau_{\mathrm{th}}^{-2} - 2\tau_{\mathrm{max}}^{-2}\right) + \left(\frac{\partial x_{\mathrm{QP}}}{\partial P_{\mathrm{abs}}}\right)^2 2h\nu_{\mathrm{photon}}P_{\mathrm{abs}}. \tag{2.122}$$

NEP optimization

Far-IR spectroscopy from space requires very low NEPs ($< 1\times10^{-19}$ W/$\sqrt{\mathrm{Hz}}$). With no absorbed power, the fractional frequency and amplitude NEPs are equivalent. However, the electrical amplitude noise is filtered through the resonator and any additional loss in front of the first-stage amplifier, placing significantly more stringent requirements on amplification. Therefore, frequency readout is typically used for KIDs. The total NEP can be written as

$$\mathrm{NEP}^2 = \mathrm{NEP}_{\mathrm{QP}}^2 + \mathrm{NEP}_{\mathrm{TLS}}^2 + \mathrm{NEP}_{\mathrm{amp}}^2, \tag{2.123}$$

where, for $P_{\mathrm{abs}} = 0$, $2\pi\nu \ll 1/\tau_{\mathrm{QP}}$, and $2\pi\nu \ll 1/\tau_{\mathrm{rd}}$, the QP noise is

$$\mathrm{NEP}_{\mathrm{QP}}(P_{\mathrm{abs}} = 0, \nu \to 0) = \Delta_0\sqrt{2n^*V\frac{\tau_{\mathrm{max}}}{\tau_{\mathrm{th}}}\left(\tau_{\mathrm{th}}^{-2} - \tau_{\mathrm{max}}^{-2}\right)}, \tag{2.124}$$

the TLS noise is

$$\mathrm{NEP}_{\mathrm{TLS}}(P_{\mathrm{abs}} = 0, \nu \to 0) = \frac{4N_0\Delta_0^2V}{\alpha\gamma S_2\tau_{\mathrm{th}}}\sqrt{\kappa_{\mathrm{material}}\kappa_{\mathrm{geom}}\nu^{-\alpha_\nu}T^{-\alpha_T}P_{\mu\mathrm{W}}^{-\alpha_P}}, \tag{2.125}$$

and the amplifier noise is

$$\mathrm{NEP}_{\mathrm{amp}}(P_{\mathrm{abs}} = 0, \nu \to 0) = \left|\frac{\partial S_{21}}{\partial x}\right|^{-1}\sqrt{\frac{k_BT_n}{P_{\mu\mathrm{W}}}}\frac{4N_0\Delta_0^2V}{\gamma\alpha\tau_{\mathrm{th}}S_2}. \tag{2.126}$$

The following relationships are useful for optimizing the NEP.

1. **Temperature:** Flight qualified continuous adiabatic demagnetization refrigerators (CADRs) are capable of reaching $\sim$ 50 mK, setting a lower limit for the operating temperature.[23] The QP noise increases with temperature (through a decrease in τ_{th}) and the TLS noise decreases with temperature (above $\sim$ 100 mK), so an intermediate temperature exists where the NEP is optimized. This optimal temperature also depends on ν. For the KIDs studied in this thesis, the optimal temperature is 100 – 150 mK.

2. **Inductor material:** All three NEP terms increase with $\Delta_0 \propto T_c$, so low-T_c materials are desirable. However, the instrument base temperature sets a lower limit on T_c to ensure $T \ll T_c$. Additionally, all three NEP terms decrease with increasing QP lifetime, and QP noise decreases with increasing recombination constant. Therefore, the ideal material will minimize T_c (up to the limit set by the fridge operating temperature) and have a long QP lifetime and high recombination constant. For a 100 mK operating temperature, Al ($T_c \sim 1.2$ K) is often the material of choice. For instruments with a higher operating temperature, a higher T_c material must be used, such as NbTiN ($T_c \sim 13$ K) or Nb ($T_c \sim 9.3$ K). Modern DRs are readily capable of achieving < 20 mK, so some ground-based KID observatories use lower T_c materials, such as Hf ($T_c \sim 170$ mK).[55]

3. **Capacitor materials:** The capacitor consists of superconducting plates (for low dissipation) and a low loss dielectric (for lower TLS noise). For PPCs, amorphous silicon (a-Si) is commonly used. For IDCs, the TLSs are mostly present in surface oxides, so a material with a low oxidation rate is desirable, such as NbN or NbTiN.

4. **Capacitor geometry:** In general, larger capacitors of a given architecture and capacitance will exhibit less TLS noise, depending on the details of the scaling. See Subsection 2.4.3 for more details.

5. **Inductor volume:** Lowering the inductor volume is the most straightforward method for achieving a better NEP, because $\mathrm{NEP_{QP}}(P_{\mathrm{abs}}, \nu \to 0) \propto \sqrt{V}$, $\mathrm{NEP_{TLS}}(P_{\mathrm{abs}}, \nu \to 0) \propto V$, and $\mathrm{NEP_{amp}}(P_{\mathrm{abs}}, \nu \to 0) \propto V$. However, the inductor design for a LEKID must also be optimized to absorb light of the desired wavelength efficiently and achieve a sufficient kinetic inductance, which places a constraint on the minimum volume.

6. **QP lifetime:** Increasing both the maximum and operational QP lifetime will decrease the NEP, because $\mathrm{NEP_{QP}}(P_{\mathrm{abs}}, \nu \to 0) \propto \sqrt{\frac{\tau_{\mathrm{max}}}{\tau_{\mathrm{th}}}\left(\tau_{\mathrm{th}}^{-2} - \tau_{\mathrm{max}}^{-2}\right)}$, $\mathrm{NEP_{TLS}}(P_{\mathrm{abs}}, \nu \to 0) \propto \frac{1}{\tau_{\mathrm{th}}}$, and $\mathrm{NEP_{amp}}(P_{\mathrm{abs}}, \nu \to 0) \propto \frac{1}{\tau_{\mathrm{th}}}$. The upper limit on the QP lifetime for current far-IR telescope proposals is 3 ms, so Al ($\tau_{\mathrm{max}} \sim 1$ ms) is an ideal material. However, τ_{max} is highly sensitive to Al film quality, so care must be taken in design and fabrication. The challenges of achieving high QP lifetimes in Al are discussed in Subsection 4.3.1.

7. **Tone frequency and power:** Tuning a KID consists of choosing the optimal tone frequency and power. Tuning is discussed in detail in Appendix E. The two NEP terms that depend on the tone power are the amplifier noise ($\mathrm{NEP}_{\mathrm{amp}} \propto P_{\mu\mathrm{W}}^{-1/2}$) and the TLS noise ($\mathrm{NEP}_{\mathrm{TLS}} \propto P_{\mu\mathrm{W}}^{-\alpha_P/2}$). Thus, higher tone power will lead to a decreased NEP. However, the KID will eventually reach bifurcation, which sets an upper limit on the practical tone power. KIDs could potentially be read out above bifurcation: a measurement of TiN KIDs found the NEP to decrease by a factor of 10 at a bias power of 18 dB above bifurcation.[46] This measurement requires sweeping of the tone towards the resonator from high frequency in order to overcome the hysteretic nature of the resonance. Due to readout constraints, this method has never been fielded, leaving bifurcation as the conventional upper limit on the tone power. However, recent advances in readout systems may warrant further investigation into bifurcated KID readout. More advanced schemes such as tone power feedback are also in development, which may allow for higher-power operation while simultaneously locking the resonance in place, thereby improving crosstalk.[42]

   A tone frequency sweep over S_{21} is performed to obtain $\{f, z\}$, where f is the frequency data and z is the complex S_{21} data. The data can be fit following the procedure in Appendix B to extract a_{nl}. The sweep and fit are repeated over a range of tone powers, and the tone power corresponding to $a_{\mathrm{nl}} \sim 0.5$ is typically chosen to maximize the power while staying under bifurcation.

   After the tone power is optimized, the tone frequency is chosen to correspond to the maximum of $|z_1 - z_2|$, where z_1 and z_2 are sequential points in z. Practical considerations for tuning are discussed in Appendix E.

   In addition to bifurcation, QP excitations from microwave power will eventually cause the NEP to increase. This effect is more likely to occur in materials with low T_c,[49] so it may set a more stringent upper limit on tone power for Al KIDs compared to the high power used with TiN KIDs in Swenson et al. 2013.[46]

References

[1] Peter A. R. Ade et al. “A Constraint on Primordial B-modes from the First Flight of the Spider Balloon-borne Telescope”. In: *The Astrophysical Journal* 927.2 (Mar. 2022), p. 174. ISSN: 0004-637X, 1538-4357. DOI: 10.3847/

1538-4357/ac20df. URL: https://iopscience.iop.org/article/10.3847/1538-4357/ac20df (visited on 03/09/2023).

[2] Peter A. R. Ade et al. "ANTENNA-COUPLED TES BOLOMETERS USED IN BICEP2, *Keck Array* , AND SPIDER". In: *The Astrophysical Journal* 812.2 (Oct. 2015), p. 176. ISSN: 1538-4357. DOI: 10.1088/0004-637X/812/2/176. URL: https://iopscience.iop.org/article/10.1088/0004-637X/812/2/176 (visited on 03/09/2023).

[3] Peter A. R. Ade et al. "Bicep/Keck XV: The Bicep3 Cosmic Microwave Background Polarimeter and the First Three-year Data Set". In: *The Astrophysical Journal* 927.1 (Mar. 2022), p. 77. ISSN: 0004-637X, 1538-4357. DOI: 10.3847/1538-4357/ac4886. URL: https://iopscience.iop.org/article/10.3847/1538-4357/ac4886 (visited on 03/09/2023).

[4] Peter A. R. Ade et al. "Bicep2. II. EXPERIMENT AND THREE-YEAR DATA SET". In: *The Astrophysical Journal* 792.1 (Aug. 2014). Publisher: The American Astronomical Society, p. 62. ISSN: 0004-637X. DOI: 10.1088/0004-637X/792/1/62. URL: https://dx.doi.org/10.1088/0004-637X/792/1/62 (visited on 03/10/2023).

[5] Phillip W. Anderson, Bertrand I. Halperin, and Chandra M. Varma. "Anomalous low-temperature thermal properties of glasses and spin glasses". en. In: *Philosophical Magazine* 25.1 (Jan. 1972), pp. 1–9. ISSN: 0031-8086. DOI: 10.1080/14786437208229210. URL: http://www.tandfonline.com/doi/abs/10.1080/14786437208229210 (visited on 01/17/2025).

[6] Rami Barends et al. "Enhancement of quasiparticle recombination in Ta and Al superconductors by implantation of magnetic and nonmagnetic atoms". In: *Physical Review B* 79.2 (Jan. 2009). Publisher: American Physical Society, p. 020509. DOI: 10.1103/PhysRevB.79.020509. URL: https://link.aps.org/doi/10.1103/PhysRevB.79.020509 (visited on 10/01/2023).

[7] James Bock et al. *Study of the Experimental Probe of Inflationary Cosmology (EPIC)-Intemediate Mission for NASA's Einstein Inflation Probe*. arXiv:0906.1188 [astro-ph]. June 2009. DOI: 10.48550/arXiv.0906.1188. URL: http://arxiv.org/abs/0906.1188 (visited on 04/26/2023).

[8] Jonathan Burnett et al. "Evidence for interacting two-level systems from the 1/f noise of a superconducting resonator". en. In: *Nature Communications* 5.1 (June 2014). Number: 1 Publisher: Nature Publishing Group, p. 4119. ISSN: 2041-1723. DOI: 10.1038/ncomms5119. URL: https://www.nature.com/articles/ncomms5119 (visited on 10/29/2023).

[9] LiteBIRD Collaboration et al. "Probing Cosmic Inflation with the LiteBIRD Cosmic Microwave Background Polarization Survey". In: *Progress of Theoretical and Experimental Physics* 2023.4 (Apr. 2023). arXiv:2202.02773 [astro-ph], 042F01. ISSN: 2050-3911. DOI: 10.1093/ptep/ptac150. URL: http://arxiv.org/abs/2202.02773 (visited on 04/26/2023).

[10] The Polarbear Collaboration et al. “A Measurement of the Degree-scale CMB B-mode Angular Power Spectrum with Polarbear”. In: *The Astrophysical Journal* 897.1 (July 2020). Publisher: The American Astronomical Society, p. 55. ISSN: 0004-637X. DOI: 10.3847/1538-4357/ab8f24. URL: https://dx.doi.org/10.3847/1538-4357/ab8f24 (visited on 03/10/2023).

[11] Peter K. Day et al. “A 25-micrometer Single-Photon-Sensitive Kinetic Inductance Detector”. In: *Physical Review X* 14.4 (Oct. 2024). Publisher: American Physical Society, p. 041005. DOI: 10.1103/PhysRevX.14.041005. URL: https://link.aps.org/doi/10.1103/PhysRevX.14.041005 (visited on 11/02/2024).

[12] Peter K. Day et al. “A broadband superconducting detector suitable for use in large arrays”. en. In: *Nature* 425.6960 (Oct. 2003). Publisher: Nature Publishing Group, pp. 817–821. ISSN: 1476-4687. DOI: 10.1038/nature02037. URL: https://www.nature.com/articles/nature02037 (visited on 11/16/2024).

[13] P.J. De Visser. “Quasiparticle dynamics in aluminium superconducting microwave resonators”. PhD thesis. Delft University of Technology, 2014. DOI: 10.4233/UUID:EAE4C9FC-F90D-4C12-A878-8428EE4ADB4C. URL: http://resolver.tudelft.nl/uuid:eae4c9fc-f90d-4c12-a878-8428ee4adb4c (visited on 06/21/2025).

[14] Fabien Defrance et al. “Characterization of the low electric field and zero-temperature two-level-system loss in hydrogenated amorphous silicon”. en. In: *Physical Review Materials* 8.3 (Mar. 2024), p. 035602. ISSN: 2475-9953. DOI: 10.1103/PhysRevMaterials.8.035602. URL: https://link.aps.org/doi/10.1103/PhysRevMaterials.8.035602 (visited on 04/26/2025).

[15] Wendeline Everett et al. “Design and Bolometer Characterization of the SPT-3G First-Year Focal Plane”. In: *J. Low Temp. Phys.* 193.5-6 (Dec. 2018), pp. 1085–1093. ISSN: 0022-2291, 1573-7357. DOI: 10.1007/s10909-018-2057-2. URL: http://link.springer.com/10.1007/s10909-018-2057-2 (visited on 03/09/2023).

[16] Massimiliano Galeazzi. “Fundamental Noise Processes in TES Devices”. In: *IEEE Transactions on Applied Superconductivity* 21.3 (June 2011), pp. 267–271. ISSN: 1051-8223, 1558-2515. DOI: 10.1109/TASC.2010.2091243. URL: http://ieeexplore.ieee.org/document/5643118/ (visited on 03/27/2025).

[17] Jiansong Gao. “The Physics of Superconducting Microwave Resonators”. en. phd. California Institute of Technology, 2008. DOI: 10.7907/RAT0-VM75. URL: https://resolver.caltech.edu/CaltechETD:etd-06092008-235549 (visited on 12/02/2024).

[18] Jiansong Gao et al. “A semiempirical model for two-level system noise in superconducting microresonators”. en. In: *Applied Physics Letters* 92.21 (May 2008), p. 212504. ISSN: 0003-6951, 1077-3118. DOI: 10.1063/1.2937855. URL: https://pubs.aip.org/apl/article/92/21/212504/851718/A-semiempirical-model-for-two-level-system-noise (visited on 11/03/2023).

[19] Jiansong Gao et al. “Experimental evidence for a surface distribution of two-level systems in superconducting lithographed microwave resonators”. In: *Applied Physics Letters* 92.15 (Apr. 2008), p. 152505. ISSN: 0003-6951. DOI: 10.1063/1.2906373. URL: https://doi.org/10.1063/1.2906373 (visited on 01/25/2025).

[20] Jiansong Gao et al. “Noise properties of superconducting coplanar waveguide microwave resonators”. en. In: *Applied Physics Letters* 90.10 (Mar. 2007), p. 102507. ISSN: 0003-6951, 1077-3118. DOI: 10.1063/1.2711770. URL: https://pubs.aip.org/apl/article/90/10/102507/332953/Noise-properties-of-superconducting-coplanar (visited on 11/03/2023).

[21] David J. Goldie and Stafford Withington. “Non-equilibrium superconductivity in quantum-sensing superconducting resonators”. In: *Superconductor Science Technology* 26 (Jan. 2013), p. 015004. ISSN: 0953-2048. DOI: 10.1088/0953-2048/26/1/015004. URL: https://ui.adsabs.harvard.edu/abs/2013SuScT..26a5004G (visited on 01/30/2025).

[22] Doyal A. Harper et al. “HAWC+, the Far-Infrared Camera and Polarimeter for SOFIA”. In: *J. Astron. Instrum.* 07.04 (Dec. 2018), p. 1840008. ISSN: 2251-1717, 2251-1725. DOI: 10.1142/S2251171718400081. URL: https://www.worldscientific.com/doi/10.1142/S2251171718400081 (visited on 03/09/2023).

[23] Amir E. Jahromi and Peter J. Shirron. “Compact and efficient continuous adiabatic demagnetization refrigerator for line emission mapper”. In: *Journal of Astronomical Telescopes, Instruments, and Systems* 9.04 (Oct. 2023). ISSN: 2329-4124. DOI: 10.1117/1.JATIS.9.4.041003. URL: https://www.spiedigitallibrary.org/journals/Journal-of-Astronomical-Telescopes-Instruments-and-Systems/volume-9/issue-04/041003/Compact-and-efficient-continuous-adiabatic-demagnetization-refrigerator-for-line-emission/10.1117/1.JATIS.9.4.041003.full (visited on 04/28/2025).

[24] Steven B. Kaplan et al. “Quasiparticle and phonon lifetimes in superconductors”. en. In: *Physical Review B* 14.11 (Dec. 1976), pp. 4854–4873. ISSN: 0556-2805. DOI: 10.1103/PhysRevB.14.4854. URL: https://link.aps.org/doi/10.1103/PhysRevB.14.4854 (visited on 04/25/2025).

[25] Kent D. Irwin and G. C. Hilton. “Transition-Edge Sensors”. In: *Cryogenic Particle Detection*. Topics in applied physics 99 (2005). OCLC: ocm60800561, pp. 63–149. DOI: 10.1007/10933596_3.

[26] Sarah Kernasovskiy et al. “Optimization and sensitivity of the Keck array”. In: ed. by Wayne S. Holland. Amsterdam, Netherlands, Sept. 2012, 84521B. DOI: 10.1117/12.926934. URL: http://proceedings.spiedigitallibrary.org/proceeding.aspx?doi=10.1117/12.926934 (visited on 03/10/2023).

[27] Moe S. Khalil et al. “An analysis method for asymmetric resonator transmission applied to superconducting devices”. In: *Journal of Applied Physics* 111.5 (Mar. 2012), p. 054510. ISSN: 0021-8979. DOI: 10.1063/1.3692073. URL: https://doi.org/10.1063/1.3692073 (visited on 03/04/2024).

[28] Takayuki Kubo. “Significant contributions of the Higgs mode and impurity-scattering self-energy corrections to the low-frequency complex conductivity in dc-biased superconducting devices”. en. In: *Physical Review Applied* 22.4 (Oct. 2024), p. 044042. ISSN: 2331-7019. DOI: 10.1103/PhysRevApplied.22.044042. URL: https://link.aps.org/doi/10.1103/PhysRevApplied.22.044042 (visited on 01/30/2025).

[29] Shwetank Kumar et al. “Temperature dependence of the frequency and noise of superconducting coplanar waveguide resonators”. en. In: *Applied Physics Letters* 92.12 (Mar. 2008), p. 123503. ISSN: 0003-6951, 1077-3118. DOI: 10.1063/1.2894584. URL: https://pubs.aip.org/apl/article/92/12/123503/334498/Temperature-dependence-of-the-frequency-and-noise (visited on 11/03/2023).

[30] Jan van der Kuur et al. “Small-Signal Behavior of a TES Under AC Bias”. In: *IEEE Trans. Appl. Supercond.* 21.3 (June 2011), pp. 281–284. ISSN: 1051-8223, 1558-2515. DOI: 10.1109/TASC.2010.2099092. URL: http://ieeexplore.ieee.org/document/5692866/ (visited on 11/14/2022).

[31] Marijn Lucas et al. “Quantum bath suppression in a superconducting circuit by immersion cooling”. en. In: *Nature Communications* 14.1 (June 2023), p. 3522. ISSN: 2041-1723. DOI: 10.1038/s41467-023-39249-z. URL: https://www.nature.com/articles/s41467-023-39249-z (visited on 02/05/2025).

[32] John M. Martinis et al. “Decoherence in Josephson Qubits from Dielectric Loss”. In: *Physical Review Letters* 95.21 (Nov. 2005). Publisher: American Physical Society, p. 210503. DOI: 10.1103/PhysRevLett.95.210503. URL: https://link.aps.org/doi/10.1103/PhysRevLett.95.210503 (visited on 12/05/2023).

[33] Daniel C. Mattis and John Bardeen. “Theory of the Anomalous Skin Effect in Normal and Superconducting Metals”. In: *Physical Review* 111.2 (July 1958). Publisher: American Physical Society, pp. 412–417. DOI: 10.1103/PhysRev.111.412. URL: https://link.aps.org/doi/10.1103/PhysRev.111.412 (visited on 01/15/2025).

[34] Benjamin A. Mazin. "Microwave Kinetic Inductance Detectors". en. phd. California Institute of Technology, 2005. DOI: 10.7907/GZ72-V784. URL: https://resolver.caltech.edu/CaltechETD:etd-10042004-120707 (visited on 12/02/2024).

[35] Edoardo Milotti. *1/f noise: a pedagogical review*. arXiv:physics/0204033. Apr. 2002. DOI: 10.48550/arXiv.physics/0204033. URL: http://arxiv.org/abs/physics/0204033 (visited on 01/17/2025).

[36] Clemens Müller, Jared H Cole, and Jürgen Lisenfeld. "Towards understanding two-level-systems in amorphous solids: insights from quantum circuits". In: *Reports on Progress in Physics* 82.12 (Dec. 2019), p. 124501. ISSN: 0034-4885, 1361-6633. DOI: 10.1088/1361-6633/ab3a7e. URL: https://iopscience.iop.org/article/10.1088/1361-6633/ab3a7e (visited on 07/28/2025).

[37] Omid Noroozian. "Superconducting Microwave Resonator Arrays for Submillimeter / Far-infrared Imaging". en. phd. California Institute of Technology, 2012. DOI: 10.7907/8MG2-NB23. URL: https://resolver.caltech.edu/CaltechTHESIS:06122012-091920562 (visited on 12/02/2024).

[38] Omid Noroozian et al. "Two-level system noise reduction for Microwave Kinetic Inductance Detectors". en. In: Stanford (California), 2009, pp. 148–151. DOI: 10.1063/1.3292302. URL: https://pubs.aip.org/aip/acp/article/1185/1/148-151/692603 (visited on 11/03/2023).

[39] Aaron D. O'Connell et al. "Microwave dielectric loss at single photon energies and millikelvin temperatures". en. In: *Applied Physics Letters* 92.11 (Mar. 2008), p. 112903. ISSN: 0003-6951, 1077-3118. DOI: 10.1063/1.2898887. URL: https://pubs.aip.org/apl/article/92/11/112903/326064/Microwave-dielectric-loss-at-single-photon (visited on 04/26/2025).

[40] W A Phillips. "Two-level states in glasses". en. In: *Reports on Progress in Physics* 50.12 (Dec. 1987), pp. 1657–1708. ISSN: 0034-4885, 1361-6633. DOI: 10.1088/0034-4885/50/12/003. URL: https://iopscience.iop.org/article/10.1088/0034-4885/50/12/003 (visited on 04/01/2024).

[41] Steven A. H. de Rooij et al. "Strong reduction of quasiparticle fluctuations in a superconductor due to decoupling of the quasiparticle number and lifetime". In: *Physical Review B* 104.18 (Nov. 2021). Publisher: American Physical Society, p. L180506. DOI: 10.1103/PhysRevB.104.L180506. URL: https://link.aps.org/doi/10.1103/PhysRevB.104.L180506 (visited on 06/29/2025).

[42] Maclean Rouble et al. *A first demonstration of active feedback control and multi-frequency imaging techniques for kinetic inductance detectors*. Version Number: 1. 2024. DOI: 10.48550/ARXIV.2406.17175. URL: https://arxiv.org/abs/2406.17175 (visited on 04/02/2025).

[43] A. V. Semenov et al. “Coherent Excited States in Superconductors due to a Microwave Field”. In: *Physical Review Letters* 117.4 (July 2016). Publisher: American Physical Society, p. 047002. DOI: 10.1103/PhysRevLett.117.047002. URL: https://link.aps.org/doi/10.1103/PhysRevLett.117.047002 (visited on 01/30/2025).

[44] Joshua A. Sobrin et al. “The Design and Integrated Performance of SPT-3G”. In: *The Astrophysical Journal Supplement Series* 258.2 (Feb. 2022), p. 42. ISSN: 0067-0049, 1538-4365. DOI: 10.3847/1538-4365/ac374f. URL: https://iopscience.iop.org/article/10.3847/1538-4365/ac374f (visited on 03/09/2023).

[45] Johannes G. Staguhn et al. “THE GISMO TWO-MILLIMETER DEEP FIELD IN GOODS-N”. In: *The Astrophysical Journal* 790.1 (July 2014). Publisher: The American Astronomical Society, p. 77. ISSN: 0004-637X. DOI: 10.1088/0004-637X/790/1/77. URL: https://dx.doi.org/10.1088/0004-637X/790/1/77 (visited on 03/21/2023).

[46] Loren J. Swenson et al. “Operation of a titanium nitride superconducting microresonator detector in the nonlinear regime”. In: *Journal of Applied Physics* 113.10 (Mar. 2013), p. 104501. ISSN: 0021-8979. DOI: 10.1063/1.4794808. URL: https://doi.org/10.1063/1.4794808 (visited on 12/01/2024).

[47] Robert J. Thornton et al. “THE ATACAMA COSMOLOGY TELESCOPE: THE POLARIZATION-SENSITIVE ACTPol INSTRUMENT”. In: *The Astrophysical Journal Supplement Series* 227.2 (Dec. 2016), p. 21. ISSN: 1538-4365. DOI: 10.3847/1538-4365/227/2/21. URL: https://iopscience.iop.org/article/10.3847/1538-4365/227/2/21 (visited on 03/09/2023).

[48] Konstantin S. Tikhonov, M. A. Skvortsov, and T. M. Klapwijk. “Superconductivity in the presence of microwaves: Full phase diagram”. en. In: *Physical Review B* 97.18 (May 2018), p. 184516. ISSN: 2469-9950, 2469-9969. DOI: 10.1103/PhysRevB.97.184516. URL: https://link.aps.org/doi/10.1103/PhysRevB.97.184516 (visited on 01/30/2025).

[49] Peter J. de Visser et al. “Evidence of a Nonequilibrium Distribution of Quasiparticles in the Microwave Response of a Superconducting Aluminum Resonator”. In: *Physical Review Letters* 112.4 (Jan. 2014). Publisher: American Physical Society, p. 047004. DOI: 10.1103/PhysRevLett.112.047004. URL: https://link.aps.org/doi/10.1103/PhysRevLett.112.047004 (visited on 01/30/2025).

[50] Albert Kamau Wandui. “Thermal Kinetic Inductance Detectors (TKIDs) for Cosmic Microwave Background (CMB) Polarimetry”. en. Medium: PDF Version Number: Final. PhD thesis. California Institute of Technology, Sept. 2024. DOI: 10.7907/HW92-QD36. URL: https://resolver.caltech.edu/CaltechTHESIS:05232024-191504825 (visited on 06/20/2025).

[51] Jonathan T. Ward et al. “Mechanical designs and development of TES bolometer detector arrays for the Advanced ACTPol experiment”. In: ed. by Wayne S. Holland and Jonas Zmuidzinas. Edinburgh, United Kingdom, July 2016, p. 991437. DOI: 10.1117/12.2233746. URL: http://proceedings.spiedigitallibrary.org/proceeding.aspx?doi=10.1117/12.2233746 (visited on 03/09/2023).

[52] Michael B. Weissman. “1 f noise and other slow, nonexponential kinetics in condensed matter”. en. In: *Reviews of Modern Physics* 60.2 (Apr. 1988), pp. 537–571. ISSN: 0034-6861. DOI: 10.1103/RevModPhys.60.537. URL: https://link.aps.org/doi/10.1103/RevModPhys.60.537 (visited on 07/28/2025).

[53] Jonas Zmuidzinas. “Superconducting Microresonators: Physics and Applications”. en. In: *Annual Review of Condensed Matter Physics* 3.1 (Mar. 2012), pp. 169–214. ISSN: 1947-5454, 1947-5462. DOI: 10.1146/annurev-conmatphys-020911-125022. URL: https://www.annualreviews.org/doi/10.1146/annurev-conmatphys-020911-125022 (visited on 09/06/2023).

[54] Jonas Zmuidzinas. “Thermal noise and correlations in photon detection”. In: *Appl. Opt.* 42.25 (Sept. 2003), p. 4989. ISSN: 0003-6935, 1539-4522. DOI: 10.1364/AO.42.004989. URL: https://opg.optica.org/abstract.cfm?URI=ao-42-25-4989 (visited on 08/23/2022).

[55] Nicholas Zobrist et al. “Design and performance of hafnium optical and near-IR kinetic inductance detectors”. en. In: *Applied Physics Letters* 115.21 (Nov. 2019), p. 213503. ISSN: 0003-6951, 1077-3118. DOI: 10.1063/1.5127768. URL: https://pubs.aip.org/apl/article/115/21/213503/37595/Design-and-performance-of-hafnium-optical-and-near (visited on 04/28/2025).

Chapter 3

TRANSITION EDGE SENSORS FOR FAR-INFRARED SPACE ASTROPHYSICS

[1] Logan Foote et al. "High-sensitivity transition-edge-sensed bolometers: Improved speed and characterization with AC and DC bias". In: *Journal of Applied Physics* 134.9 (Sept. 2023), p. 094503. ISSN: 0021-8979. DOI: 10.1063/5.0157208. URL: https://doi.org/10.1063/5.0157208 (visited on 08/19/2024).

3.1 Introduction

This chapter outlines efforts to create high-sensitivity far-IR Transition Edge Sensed (TES) bolometers. This work was originally published in Foote et al. 2023.[6] The TES detection mechanism and noise are described in Section 2.3. The low-noise requirement poses challenges for TES design and fabrication. The devices must have low thermal conductance (G) in the suspension, while maintaining sufficient speed. Therefore, fabrication techniques must maintain low heat capacity in the released devices. Additionally, characterization is challenging at the very low loadings (of order 1 aW or less), since bolometers are susceptible to all forms of radiation; both the electronics and the thermal radiation must be heavily filtered. Early pioneering work in low-G far-IR TES bolometers was made at the Jet Propulsion Laboratory (JPL),[10] where NEPs of $2-3\times10^{-19}$ W/Hz$^{1/2}$ were demonstrated with DC voltage bias, albeit with the speed of response of 2-5 ms. In this chapter, this work is extended through the development of a low-heat-capacity wet-release process for fabricating low-G far-IR TES bolometers. The devices are characterized with both AC and DC biasing schemes, and detector responsivities are calibrated with a novel absolute power calibration technique using near-IR (1550 nm) shot noise, which overcomes uncertainties in the electrical transfer through the system. The device speeds are improved by a factor of 2-4 times relative to our previous dry-release devices, but thermal conductances and associated noise-equivalent powers are 5-10 times higher than the previously published results of devices with similar geometries.[10]

This chapter is organized as follows: following the introduction in Section 3.1 is the array design and fabrication in Section 3.2. Section 3.3 describes the experimental setup, which covers both the DC and AC setup, and the setup for the measurement

of the noise using the near-IR laser. Sections 3.4 and 3.5 describe the AC and DC measurements, respectively. These measurements include time constants, optical responsivity, and noise. Section 3.6 is the summary.

3.2 Array Design and Fabrication

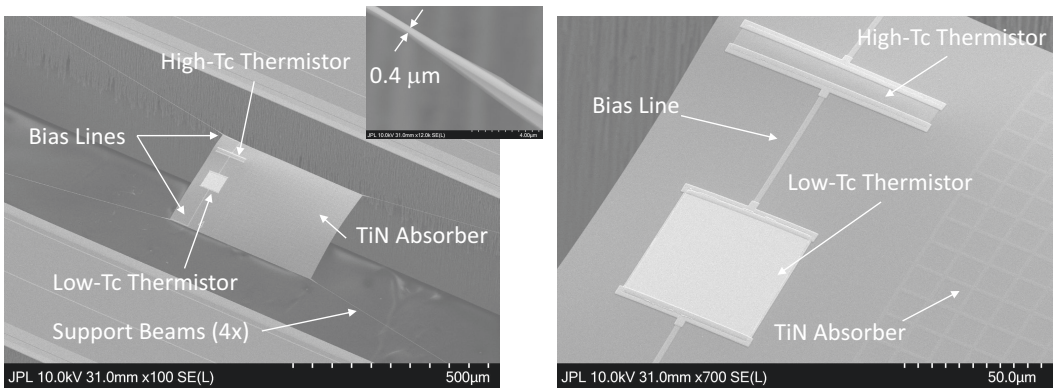

Figure 3.1: (Left) Micrograph of a single pixel. Each pixel is a suspended LSN structure consisting of an absorber and four LSN support beams (see the inset) that connect the absorber to the substrate. (Right) A dual-T_c thermistor consisting of 50 nm Ti/150 nm Au and 50 nm Ti is patterned on the absorber and electrically connected to niobium bias lines running along the support beams. A TiN absorber is patterned next to the thermistors.

Each TES sensor consists of a freestanding low-stress SiN (LSN) membrane (0.25 x 400 x 300 µm^3) which connects to the substrate through four 0.25 µm thick by 1000 µm long by 0.4 µm wide LSN support beams. Niobium wires (30 nm thick) run along two of the support beams and electrically connect to an 80 x 8 µm^2 high-T_c Ti thermistor (100 nm) in series with a 50 x 50 µm^2 low-T_c bilayer consisting of Ti (50 nm) and gold (150 nm). A grid of TiN wires (1.5 µm wide x 12 µm long x 30 nm thick) with a T_c of $\sim$ 1 K define the optical absorber, which has an effective sheet resistance of $\sim$ 400 Ω/sq. Each TES sensor is arranged in an array with a format size of 5 x 12 with a column and row spacing of 3.73 and 0.99 mm, respectively. Micrographs of a single pixel are presented in Figure 3.1.

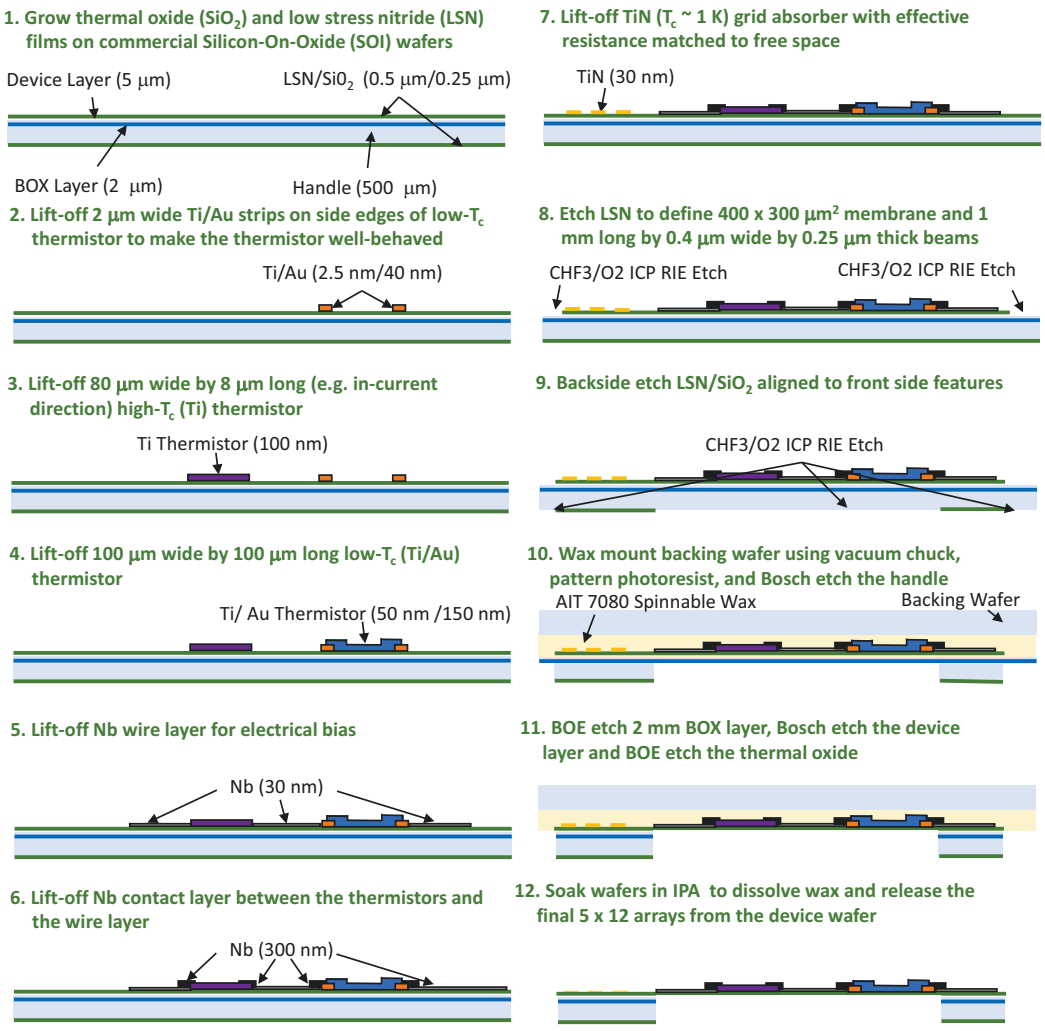

Figure 3.2: Diagram of the fabrication processes.

Based on prior measurements, it was determined that dry etching the LSN membrane causes surface roughness on the membrane, which manifests as excess heat capacity.[2] This excess heat capacity slows the response time of the TES sensor beyond the requirement. Therefore, a fabrication process was developed that does not require any dry etch steps that etch the top and bottom surface of the LSN. Key details of this process are presented in Figure 3.2 and described as follows: (1) 500 nm thermal oxide and 250 nm low pressure, chemical vapor deposition SiN (LPCVD) (-200 MPa compressive stress) were grown on bare 100 mm silicon-on-insulator (SOI) wafers (500 µm handle, 2 µm buffered oxide layer (BOX), 5 µm device) at the Jet Propulsion Laboratory's (JPL) Microdevices Laboratory. (2) Ti

(2.5 nm)/Au (40 nm) strips (2 µm wide) were patterned to passivate the edges of the low-T_c thermistor so that its overall properties are well-behaved. (3) A thermistor consisting of Ti (100 nm) was patterned via DC sputtering and a lift-off technique. (4) A thermistor consisting of a bilayer of Ti (50 nm)/Au (150 nm) was patterned via DC sputtering and a lift-off technique. (5) Nb wires (30 nm) to bias the two thermistors were defined using DC sputtering and a lift-off technique. (6) A Nb contact layer (300 nm) was sputtered on the edges of the thermistors to ensure good electrical contact between the bias lines and the thermistors. (7) A TiN absorber (30 nm) was patterned via DC sputtering with $T_c \sim 1$ K. (8) The LSN membrane was patterned using a dry CHF3/O2 ICP RIE process into a 400 x 300 μm^2 membrane and four 1 mm long x 0.4 µm wide x 0.25 µm thick support beams. (9) The backside LSN/SiO_2 was etched using a dry CHF_3/O_3 ICP RIE process aligned to the front side membrane and support beams. (10) The device wafer was wax mounted to a 150 mm backing wafer using AIT 7080 spinnable wax and a vacuum mounting technique. The handle of the SOI wafer was removed using a Bosch process and a photoresist to define openings underneath the suspended membrane and support beams. (11) The BOX layer was removed using a buffered oxide etch (BOE). The device layer was removed using a Bosch process. The thermal oxide underneath the LSN membrane was removed using buffered BOE; (12) The arrays were removed by soaking the device wafer and a 150 mm backing wafer in IPA using a fixture, which allowed the 12 x 5 arrays to separate from the backing wafer.

3.3 Experimental Setup

The TESs were tested in a BlueFors Dilution Refrigerator (DR). The temperature is controlled using a PID loop, with the thermometer and heater mounted on the mixing chamber plate near the TES sample box. The temperatures presented in this paper are measured using the PID loop thermometer. The TESs are biased with an arbitrary function generator. The bias voltage is reduced with a voltage divider before entering the cryostat. The bias and readout lines in the cryostat are phosphor-bronze shielded twisted pairs. The cabling connects to the TES housing box shown in Figure 3.3 using a 37-pin micro-D connector. The TES housing box and the mixing chamber plate are gold-plated copper, and the fasteners are brass to ensure good thermal contact while cold. The bias lines pass through a 20 MHz RC low-pass filter on a printed circuit board and are wirebonded into a chip containing a Magnicon 2-stage SQUID.[8] The output of the SQUID electronics is recorded with an oscilloscope. The bias and readout system is set up in either a DC or an AC mode

depending on the measurement. The AC setup is described in Section 3.3.1 and the DC setup is described in Section 3.3.2.

3.3.1 AC Setup

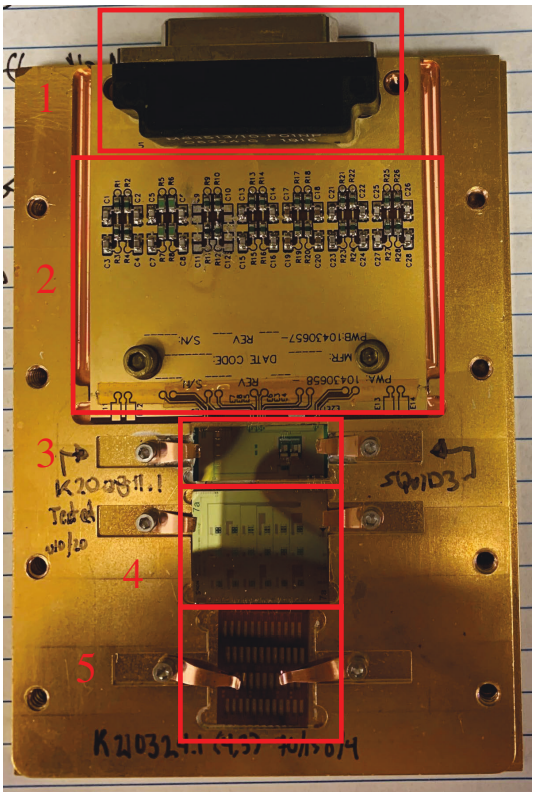

Figure 3.3: Photo of the TES housing box with the lid removed. The components are as follows: 1. 37-pin Micro-D connector, 2. RC filter circuit board, 3. Magnicon SQUID chip, 4. 18-channel LC filter chip, and 5. 60-pixel TES subarray (5 columns x 12 rows).

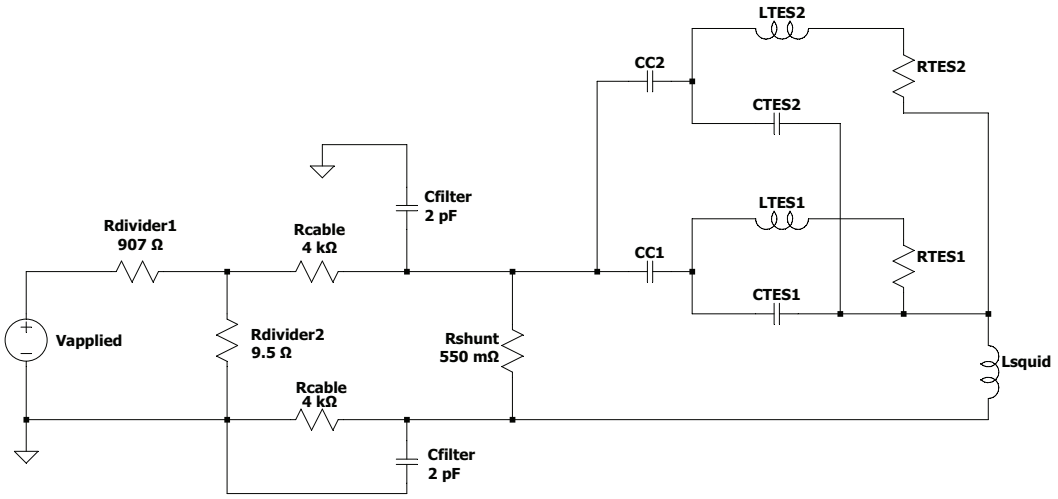

Figure 3.4: Spice model of the AC setup circuit. The components are as follows: the function generator (Vapplied), voltage divider resistors (Rdivider1 and Rdivider2), cables with added resistors (Rcable), filter capacitors (Cfilter), a shunt resistor (Rshunt), an LC chip (CC, CTES, and LTES), TESs (RTES), and the SQUID (Lsquid). Only 2 of the 18 LC channels are included in the circuit diagram.

The AC setup uses a cryogenic LC resonant filter array designed and fabricated at SRON, developed as part of their AC multiplexing scheme,[14] which has successfully supported 160 far-IR TES pixels in a single circuit.[7] Our work used an 18-channel test chip with resonant frequencies between 1 and 5 MHz (component 4 in Figure 3.3). A circuit model of the AC system is presented in Figure 3.4. Each TES is wirebonded into one of the LC resonant circuits. The 18-channels are connected to two TESs without absorbers, two TESs with absorbers, four thermistors, and ten shorts.

The MHz band of the AC bias circuit is beyond the closed-loop bandwidth of the SQUID and commercial electronics; therefore, the SQUID is operated in an open-loop mode for the AC setup.

The SQUID is operated in the regime where the current to voltage conversion is linear to within 5%. The current scale is calibrated by measuring the voltage response of a single flux quantum, and using the reported input coil coupling for the SQUID from the Magnicon datasheet (measured at 320 mK). Measurements that use the AC setup are presented in Section 3.4.

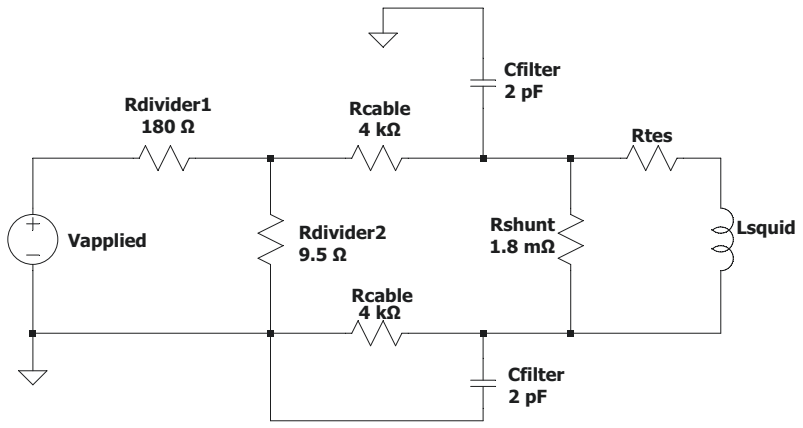

Figure 3.5: Spice model of the DC setup circuit. The components are as follows: the function generator (Vapplied), voltage divider resistors (Rdivider1 and Rdivider2), cables with added resistors (Rcable), filter capacitors (Cfilter), a shunt resistor (Rshunt), the TES (RTES), and the SQUID (Lsquid).

3.3.2 DC Setup

The AC measurements are complemented with with DC measurements, in which the LC chip is bypassed to measure a single TES with a more traditional DC bias. The DC measurements provided an independent check on the absolute power scale for the device without the uncertainties in the AC measurement, validating our photon-noise calibration approach presented in Section 3.4.1. The circuit model for the DC system is shown in Figure 3.5. The readout and function generator are the same in the DC and AC setup. The SQUID is operated with feedback for the DC measurements. Measurements using the DC setup are presented in Section 3.5.

3.3.3 Near-IR Laser Setup

To overcome the uncertainties in the electrical power calibration of low-G TESs, we developed a near-IR photon-noise calibration technique. For this measurement, six 0.5-mm diameter holes are drilled in the cover of the TES housing box over the detector array. The holes are drilled in an array of three (with 4 mm spacing) by two (with 5 mm spacing). The hole array is located above the four detectors that were tested with the AC setup. A fiber-optic cable with standard fiber connectors (FC connectors) is positioned about 1.3 cm in front of the holes, and the opening of the holes is 9 mm above the detector wafer. The FC connector is allowed to spray photons freely over the holes in the TES housing box. A CAD model of the laser setup is shown in Figure 3.6.

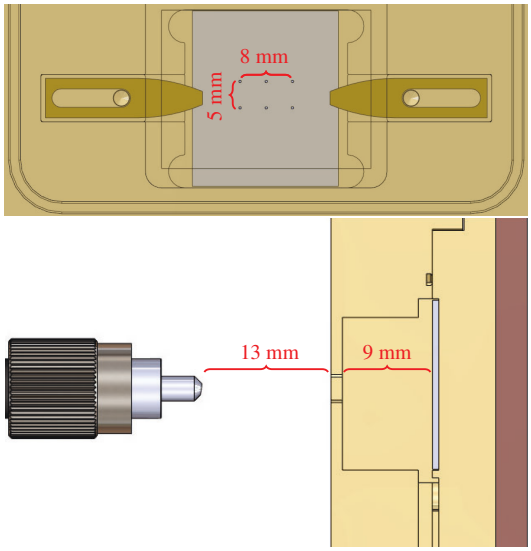

Figure 3.6: A SolidWorks model of the laser setup. (Top) The TES housing box is shown with a transparent lid. The detectors are distributed along the detector wafer (gray). (Bottom) Side view of the laser setup.

3.4 AC Measurements

Two TESs with absorbers and two TESs without absorbers were studied sequentially with the AC system, all at a bath temperature of 100 mK. The resonant frequencies of the four LC filter channels associated with the TESs are given in Table 3.1. Current versus voltage curves are measured for each TES, and bias voltages for the subsequent response and noise measurements are chosen such that the TES is at 1/2 the normal resistance. DC current versus voltage curves are presented in Section 3.5.1.

3.4.1 Photon-noise Calibration

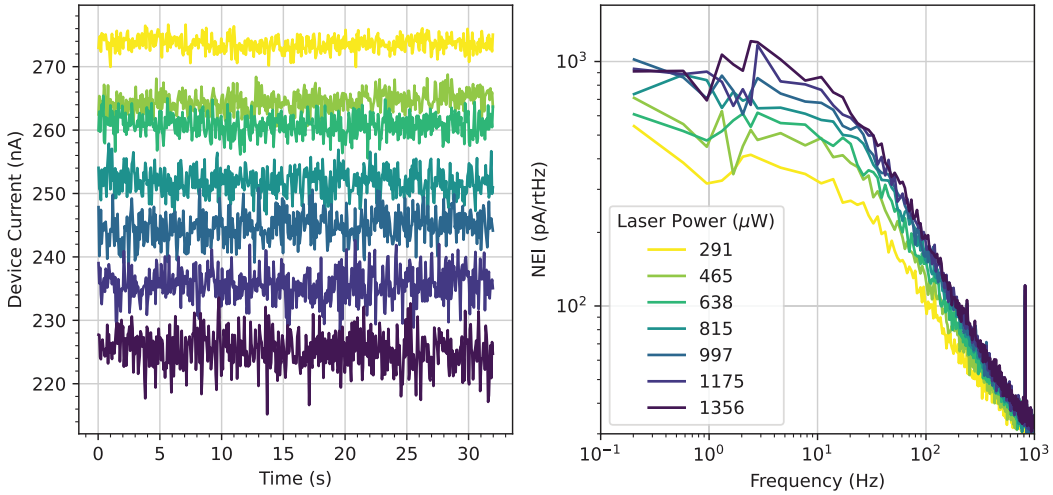

Figure 3.7: TES response to a laser power sweep. The laser power values are the measured laser power at the entrance to the cryostat. (Left) TES current versus time. (Right) NEI versus frequency. Both current and NEI are averaged in bins for visibility.

Approach

The absolute current and voltage scales in the AC setup are not known accurately due to uncertainty in the shunt resistor value, difficulty in establishing the open-loop MHz SQUID response, and reactive effects in the TES resonant circuit. To overcome these obstacles and provide an absolute electrical power calibration, we developed a technique using shot noise from a 1550 nm laser. When the laser is turned off, the current is I_0 and the noise-equivalent current (NEI) is NEI_0. Shot noise in the near-IR photon stream incident on the TES has a noise-equivalent power (NEP) given by Equation 2.5. The corresponding NEI generated by the fluctuating photon power absorbed by the TES is

$$\mathrm{NEI}_{\mathrm{photon}} = -S(\nu)\mathrm{NEP}_{\mathrm{photon}}, \tag{3.1}$$

where $S(\nu) = dI/dP$ is the current to power responsivity. The frequency dependence of the responsivity is given by

$$S(\nu) = \frac{S(\nu = 0)}{\sqrt{1 + (2\pi\nu\tau)^2}}, \tag{3.2}$$

where the rolloff is produced by the time constant of the TES, τ. The mean value of the current also changes as the near-IR power is introduced, creating an additional constraint

$$I - I_0 = S(\nu) P_{\text{photon}}, \tag{3.3}$$

which is an excellent approximation for a voltage-biased TES so long as the responsivity is constant. The power of absorbed photons is eliminated by combining Equations 3.1 and 3.3:

$$\text{NEI}^2_{\text{photon}} = 2h\nu_{\text{photon}} S(\nu)(I - I_0), \tag{3.4}$$

where $\text{NEI}^2_{\text{photon}}$ is the photon shot-noise contribution to the NEI. The measured NEI is

$$\text{NEI}^2_{\text{measured}} = \text{NEI}^2_{\text{photon}} + \text{NEI}^2_0. \tag{3.5}$$

Combining Equations 3.4 and 3.5 yields

$$\text{NEI}^2_{\text{measured}} = \alpha I + \beta, \tag{3.6}$$

where

$$\alpha = 2h\nu_{\text{photon}} S(\nu) \tag{3.7}$$

$$\beta = -\alpha I_0 - \text{NEI}^2_0. \tag{3.8}$$

The responsivity of the TES can be calculated from a fit to Equation 3.6 without knowledge of the absolute laser power incident on the detector. This calibration allows for a measurement of the NEP even if the absolute current scale unknown.

Measurements

With the bias voltage fixed, a timestream of the TES current is measured for a range of laser powers. The TES current is the mean of the timestream data. The NEI is averaged over frequencies below the rolloff, but above any low-frequency excess, to capture the white noise value. An example of a TES timestream and the corresponding NEI is plotted in Figure 3.7. The frequencies over which the NEI is averaged for this example are 0.3-3 Hz. The squared averaged NEI versus I corresponding to this example is plotted in Figure 3.8, with a linear fit. The fit parameter α is used to extract $S(\nu)$ using Equation 3.7. This calibration technique

works for the TESs with and without absorbers. The TESs with absorbers have a factor of 5 higher absorption at 1550 nm than the devices without absorbers. The measurement was repeated with both an SLD and a DFB laser source, and produced the same results to within the measurement uncertainty.

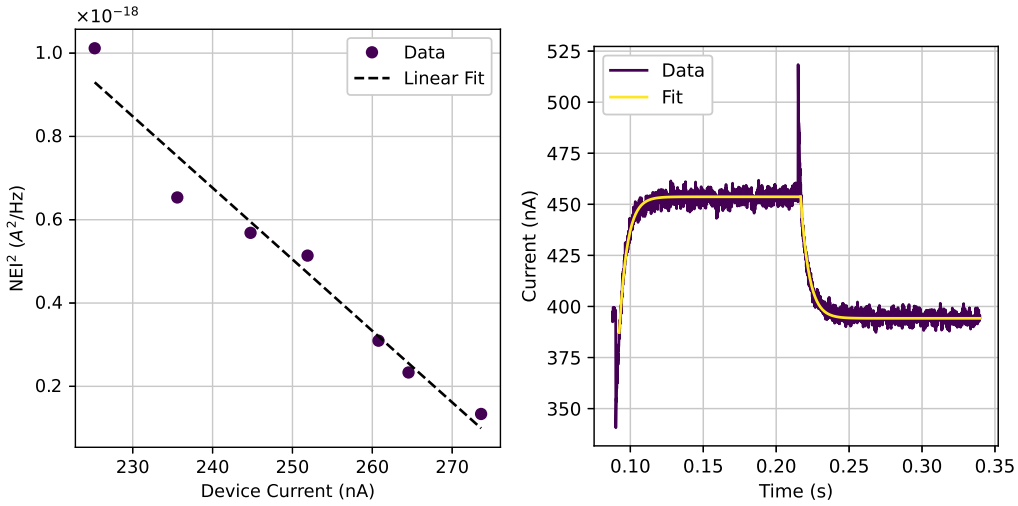

Figure 3.8: (Left) NEI^2 versus current with a linear fit. These data are extracted from the dataset presented in Figure 3.7. The responsivity for this dataset is -70.1 nA/fW. (Right) Example of time constant data and fits for ABS 1 (time constant = 6.4 ms). At each transition, the TES shows short electrical transient followed by the thermal response in the opposite direction, the latter being the relevant time constant.

3.4.2 Time Constant

Time constants are measured from a detector response to a modulated electrical signal. A small square-wave modulation is applied to the TES bias voltage. The response is fitted to an exponential function to extract the time constant. An example of the detector response to the modulated signal is plotted in Figure 3.8 with exponential fits. 64 time constants are fitted and averaged for each TES (32 ascending and 32 descending). The averaged time constants for each of the four detectors are given in Table 3.1. Our devices are slower than those from SRON.[11,12,13] Those measurements were obtained while biased deeper in the transition ($R \sim 0.25R_n$), and were generally at bath temperatures of 40-60 mK, both of which increase the electrothermal feedback and, thus, the speed relative to the conditions of our measurements: biased at $R_n/2$ and a bath temperature of 100 mK. These devices may also have excess heat capacity. The fact that our devices with absorbers are slower than those without suggests additional heat capacity in the superconducting film,

TES	Frequency (MHz)	R/R_{normal}	τ (ms)	$S(\nu = 0)$ (nA / fW)
ABS 1	2.346 970	0.538	6.4	-70.1
ABS 2	3.476 124	0.467	9.1	-29.2
NO ABS 1	2.423 641	0.449	3.7	-51.1
NO ABS 2	4.273 528	0.526	4.0	-14.8

Table 3.1: AC configuration resonant frequencies and averaged time constants for four measured TESs. ABS refers to a TES with an absorber, and NO ABS refers to a TES without an absorber. R/R_{normal} is the fraction of the normal resistance at which the detector is biased for both noise and time constant measurements. The responsivities presented here are calibrated with the laser. τ is the detector time constant.

an aspect that is anomalous and may indicate excess heat capacity in the metallic components generally.

3.4.3 AC Setup NEP

The responsivity is calculated using the photon-noise calibration method described in Section 3.4.1. The responsivities are presented in Table 3.1, along with the time constants, which are used to calculate the frequency dependence of the responsivities. The spread in responsivities is likely an artifact of the laser calibration: the responsivities include the frequency-dependent gain of the system, an aspect that is removed from the NEP through the calibration. The calculated NEPs for the four TESs are shown in Figure 3.9. The NEPs show a white noise of 1×10^{-18} and rolloffs of 30 Hz set by the measured time constant.

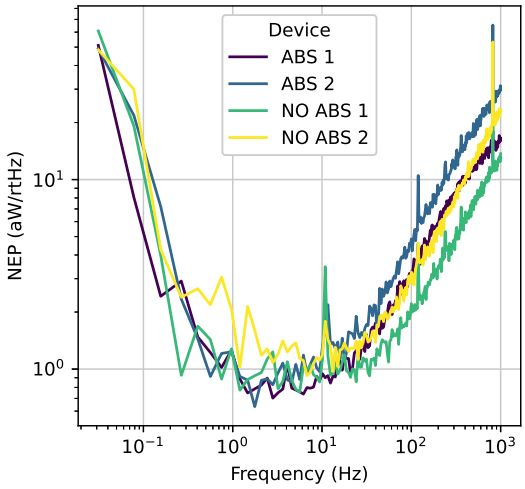

Figure 3.9: Calculated NEPs of four TESs, with the frequency response from Equation 3.2 and the measured time constants from Table 3.1.

3.5 DC Measurements

As a check on the AC measurements, we employed the well-understood DC bias setup (Section 3.3.2) to both directly measure the TES properties and to repeat the laser shot-noise calibration measurement. The DC measurements focus on the single device labeled ABS1 in Section 3.4.

3.5.1 Current Versus Voltage

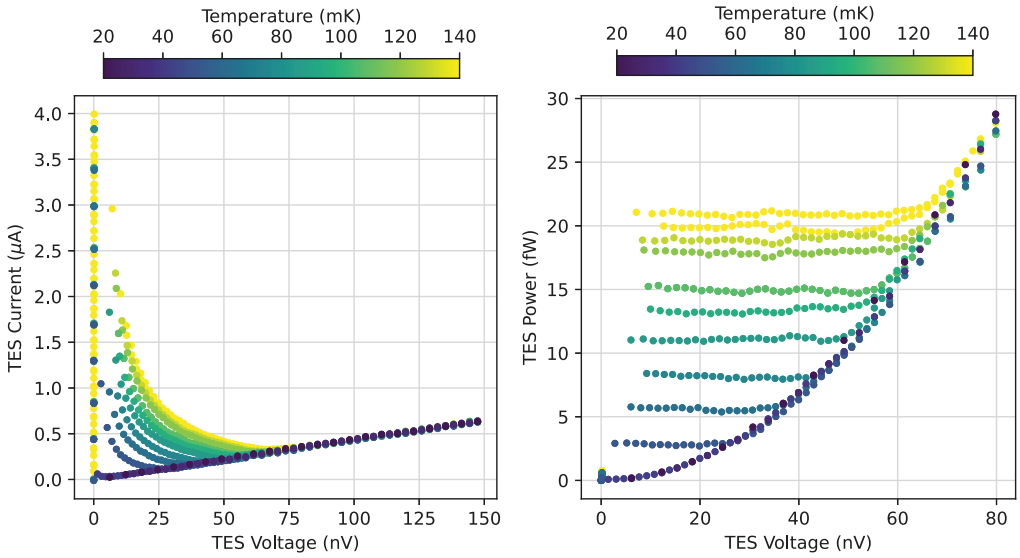

Figure 3.10: (Left) TES current versus voltage "load" curves in a DC mode. (Right) TES power versus voltage.

The total current through the parallel combination of the shunt resistor and TES is defined as I_{bias}. I_{bias} is calculated from the applied function generator voltage using the circuit model in Figure 3.5. The TES current I_{TES} is measured through the SQUID. For these DC measurements, the SQUID is operated with feedback, and the current calibration is confirmed to match the datasheet using the built-in generator. The voltage is swept from high to low for multiple bath temperatures, and the TES current is plotted versus the TES Voltage in Figure 3.10 (left). The TES power is calculated from $P_{\text{TES}} = I_{\text{TES}} V_{\text{TES}}$ and plotted versus the TES voltage in Figure 3.10 (right). The resistance of the TES is calculated from $R_{\text{TES}} = R_{\text{shunt}} \left[I_{\text{bias}} / I_{\text{TES}} - 1 \right]$. The ratio $I_{\text{TES}} / I_{\text{bias}}$ is 0.977 for the superconducting branch, and 0.00847 for the normal branch, corresponding to a negligible series resistance and a normal resistance of 211 mΩ.

3.5.2 Resistance Versus Temperature

For a range of temperatures, the TES resistance can be measured from the TES voltage versus current. For each temperature, a linear fit to current versus voltage (in the regime where heating is negligible) determines the resistance at each temperature. The resistance versus temperature is presented in Figure 3.11 (left).

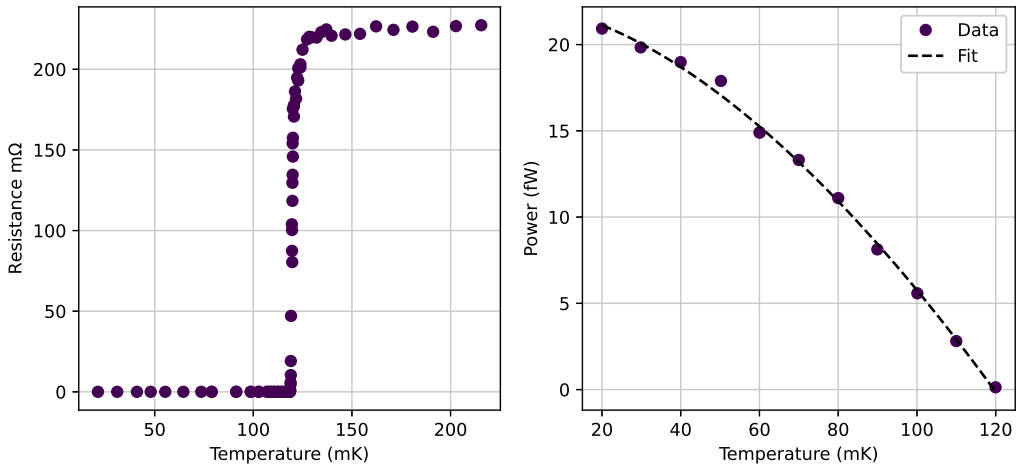

Figure 3.11: (Left) TES resistance versus temperature. (Right) TES power versus temperature on transition with a fit to Equation 3.10.

3.5.3 Thermal Conductance

The temperature dependence of the thermal conductance $G = dP/dT$ is modeled as[9]

$$G = G_c \left(\frac{T_{\text{bath}}}{T_c} \right)^{\beta}. \tag{3.9}$$

The power versus temperature relation can be calculated by integrating $dP = GdT$ with $G(T)$ defined in Equation 3.9. The integrated equation is

$$P = \frac{G_c}{(\beta + 1) T_c^{\beta}} \left(T_c^{\beta+1} - T_{\text{bath}}^{\beta+1} \right) - P_{\text{dark}}. \tag{3.10}$$

The power versus temperature data are extracted from the TES current versus voltage curves by averaging the power for each temperature in the transition. The power versus temperature is plotted in Figure 3.10 (right). The negative slope in some of the power versus voltage curves is likely due to a small error in the current calibration. This error is negligible for our purpose of calculating the thermal conductance. The data are fit to Equation 3.10. The data and fit are presented in Figure 3.11 (right). The fit parameters are presented in Table 3.2. Note that P_{Dark} is not a reliable

measurement of the actual dark power because an accurate fit to P_{Dark} requires a dark measurement of T_c and the measurement of T_c was under the same loading conditions as the power versus temperature data.

β	G_c (fW/K)	P_{Dark} (fW)
0.682	313	0.1411

Table 3.2: Power versus temperature fit parameters.

3.5.4 Photon-Noise Calibration

The photon-noise calibration was repeated with the DC setup. The DC electrical responsivity $S(\nu = 0)$ is equal to the inverse of the TES voltage, which is calculated from the circuit model in Figure 3.5. The photon-noise calibration was repeated at several bias voltages at 100 mK. The results are plotted in Figure 3.12 with the electrical responsivity. The error bars are propagated from the uncertainty in the linear fits to NEI^2 versus I.

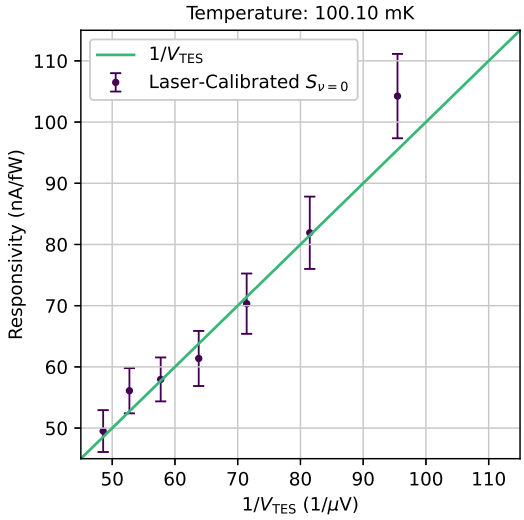

Figure 3.12: DC responsivity: comparison of electrical responsivity estimated from the applied voltage and the circuit, and via the photon-noise-calibration technique. V_{TES} is calculated from the circuit model in Figure 3.5, where R_{shunt} is set to the nominal shunt resistor value of 1.8 mΩ. The vertical error bars are propagated from the fits to NEI^2 versus I.

3.5.5 NEP Common-Mode Reduction

In order to determine whether the 1/f noise is intrinsic to the detector or due to the measurement setup, an array was tested with a time-domain readout system at the

Goddard Spaceflight Center. The time-domain system allows for common-mode reduction in the noise spectra of multiple detectors that were measured simultaneously. Four detectors without absorbers were measured.

Experimental setup

The laboratory Dewar is a custom-built cryostat designed at Goddard. It is a combination of parts from Simon Chase Cryogenics (4He sorption Cooler), High Precision Devices (ADR), and CryoMech (PT-407). A custom-built set of readout electronics is used to read and run all the thermometers and control the PID loop for the ADR at a level of less than 200 nK/$\sqrt{\text{Hz}}$.

Clocking and grounding are controlled and synchronized for electrical noise performance. Vibrational dampers are used to control acoustic noise that can be introduced from floor and air vibration. The thermal and electrical control provides a clean environment for bolometer testing. To provide a regime that makes it possible to test low-noise bolometers, a specially designed package was developed at Goddard. This package utilizes superconducting thermal filters that isolate the SQUID readout chips (the time-domain SQUID multiplexers and series arrays were provided by NIST/Boulder) from the detector chip under test. Both regions in the package are darkened with a special EMI/Thermally black paint developed at Goddard[5] and then closed out with a metal to metal stepped edge to block stray light. The multiplexed detector signals were read out using the Multi Channel Electronics (MCE) from UBC.[1]

Measurements and data reduction

The data for the plots were taken with a base temperature of 88 mK. The data were taken at night to minimize interference from other sources in three runs with different bias settings, each operating the detector at a different place on the transition. Data were taken for $\sim$ 800 s each of those runs. The sample rate is 50 MHz and 4 pixels (rows) were read out with a dead time of 4.8 µs (240 samples) for settling and a dwell time of 1.2 µs (60 samples) on each row. Thus, there were 33.33 Msamples for each row/run.

In two of these row/runs a single jump was noted. The data before the jump were averaged, and the mean was subtracted. The data after the jump were also averaged, and the mean was subtracted. Then, for each row/run, a straight line fit (offset and slope) was removed, though the slope is negligible. At the time the feedback is

locked, an arbitrary offset is set in. The gain was determined by the voltage setting on the TES and the counts to generate one Φ_0 in the feedback. The current to power responsivity is given as the standard V_{bias}. The shunt resistor is 250 $\mu\Omega$.

The PID controller was turned on but was not properly tuned for the temperature setting. Results are shown for three of the devices (there was a data glitch during the measurements of the fourth device). The noise data are presented in Figure 3.13. The white noise level is 0.8 aW/Hz$^{1/2}$, and the single-pole rolloff is at 50 Hz (3.2 ms time constant). NO ABS 2 and NO ABS 3 have a 1/f knee below 0.1 Hz, and NO ABS 1 has a higher 1/f knee of below 1 Hz. The 1/f noise is reduced from the measurements in Section 3.4.3 by up to a factor of 10.

The noise model in Figure 3.13 includes the phonon noise, the Johnson noise, and the SQUID noise from Equation 2.16. The phonon noise is 0.53 aW/$\sqrt{\text{Hz}}$, where G is measured in Section 3.5.3. The SQUID current noise was measured using an off-resonance bias, and matches the Magnicon datasheet. The SQUID current noise divided by the average responsivity of the TESs is 0.08 aW/$\sqrt{\text{Hz}}$. The average value of the Johnson current noise divided by the average responsivity is 0.19 aW/$\sqrt{\text{Hz}}$. The sum of the phonon, SQUID, and Johnson noise is 0.57 aW/$\sqrt{\text{Hz}}$.

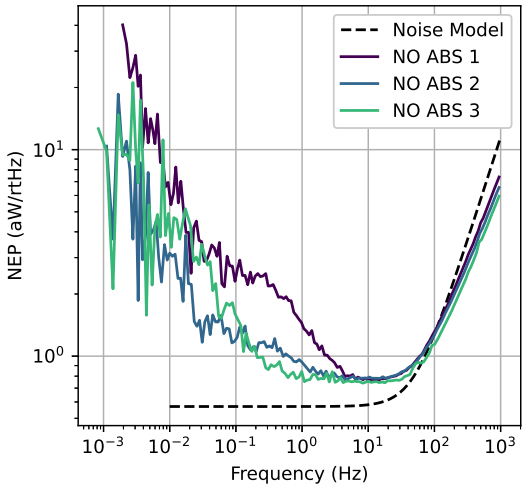

Figure 3.13: Calculated NEP of three TESs without absorbers, with the common-mode noise removed. The noise model includes the phonon noise, the SQUID noise, the Johnson noise, and the response rolloff.

3.6 Summary

The new wet-release process is compatible with large arrays of devices with 1-mm long legs on 1/4-µm SiN, and yields an improved speed of response (3–10 ms)

relative to previous low-G devices developed at the JPL Microdevices Lab (10-30 ms).[4,3,10] However, in a careful calibration in both AC and DC bias schemes and multiple experimental setups, the thermal conductances are ten times higher than previously measured with the same leg geometries in the old dry-release process. Note that a similar wet-release approach used for higher-G, higher-temperature devices (not presented here) confirms an increase in speed with fixed G relative to the dry process; therefore, the heat capacity improvements are real. The higher G in our low-G wet-release devices may be due to a reduction in phonon scattering along the legs due to the smoothness associated with the wet release.

In characterizing these devices, we developed a near-IR photon-shot-noise calibration technique which offers a rapid and unambiguous measure to total power on the TESs. While not a replacement for far-IR optical characterization, the near-IR technique is very convenient for assessing electrical properties. This technique is especially useful when the bias transfer is uncertain, as is often the case in AC bias systems. It works in the regime in which the power to current responsivity is constant, the bulk of the operating regime for TES devices. In future experiments, stray light could be reduced using a simple near-IR band-pass filter in front of the detectors.

The time-domain multiplexing system at Goddard yields better sensitivities than the AC setup, a fact attributed to improved filtration and stray light blockage, rather than a fundamental difference in the approach. Through a careful 1/f reduction, the noise is further reduced to an electrical noise-equivalent power as low as 0.8 $\mathrm{aW/Hz^{1/2}}$. This is only modestly larger than the 0.57 $\mathrm{aW/Hz^{1/2}}$ which is expected from the fluctuations in the thermal transport (the phonon noise), the Johnson noise, and the SQUID noise. The noise floor is white, suggesting that it could be dominated by stray light. The 1/f knee frequency is as low as 0.1 Hz, ample for large-scale mapping experiments envisioned for the cryogenic space missions.

Towards the end of this TES development work, the first high-sensitivity KIDs were tested at JPL. JPL research efforts shifted focus to KIDs after early measurements showed promising sensitivities. Within a year, kilo-pixel arrays of KIDs with NEPs of 1×10^{-19} $\mathrm{W/\sqrt{Hz}}$ were demonstrated. These results are described in detail in Chapter 4. Though it may be possible to resolve the challenges with TESs described above, KIDs have quickly become the leading technology for high-sensitivity far-IR applications.

References

[1] Elia S. Battistelli et al. "Functional Description of Read-out Electronics for Time-Domain Multiplexed Bolometers for Millimeter and Sub-millimeter Astronomy". In: *J. Low Temp. Phys.* 151.3 (May 2008), pp. 908–914. ISSN: 1573-7357. DOI: 10.1007/s10909-008-9772-z. URL: https://doi.org/10.1007/s10909-008-9772-z (visited on 01/27/2023).

[2] Andrew D. Beyer et al. "Characterizing Si x N y absorbers and support beams for far-infrared/submillimeter transition-edge sensors". In: ed. by Wayne S. Holland and Jonas Zmuidzinas. San Diego, California, USA, July 2010, p. 774121. DOI: 10.1117/12.857885. URL: http://proceedings.spiedigitallibrary.org/proceeding.aspx?doi=10.1117/12.857885 (visited on 07/31/2023).

[3] Andrew D. Beyer et al. "Comparing Transition-Edge Sensor Response Times in a Modified Contact Scheme with Different Support Beams". In: *J. Low Temp. Phys.* 176.3-4 (Aug. 2014), pp. 299–303. DOI: 10.1007/s10909-013-1027-y.

[4] Andrew D. Beyer et al. "Ultra-sensitive Transition-Edge Sensors for the Background Limited Infrared/Sub-mm Spectrograph (BLISS)". In: *J. Low Temp. Phys.* 167.3-4 (May 2012), pp. 182–187. DOI: 10.1007/s10909-011-0447-9.

[5] David T. Chuss et al. "A cryogenic thermal source for detector array characterization". In: *Rev. Sci. Instrum.* 88.10 (Oct. 2017). Publisher: American Institute of Physics, p. 104501. ISSN: 0034-6748. DOI: 10.1063/1.4996751. URL: https://aip.scitation.org/doi/10.1063/1.4996751 (visited on 01/27/2023).

[6] Logan Foote et al. "High-sensitivity transition-edge-sensed bolometers: Improved speed and characterization with AC and DC bias". In: *Journal of Applied Physics* 134.9 (Sept. 2023), p. 094503. ISSN: 0021-8979. DOI: 10.1063/5.0157208. URL: https://doi.org/10.1063/5.0157208 (visited on 08/19/2024).

[7] R. A. Hijmering et al. "The 160 TES bolometer read-out using FDM for SAFARI". In: ed. by Wayne S. Holland and Jonas Zmuidzinas. Montréal, Quebec, Canada, July 2014, 91531E. DOI: 10.1117/12.2056510. URL: http://proceedings.spiedigitallibrary.org/proceeding.aspx?doi=10.1117/12.2056510 (visited on 11/14/2022).

[8] *Integrated Two-Stage Current Sensors - Magnicon Research and Instrumentation - SQUID electronics, SQUID sensors, SQUID systems*. 2022. URL: http://www.magnicon.com/squid-sensors/integrated-two-stage-current-sensors (visited on 09/21/2022).

[9] Matthew Kenyon et al. “Progress on background-limited membrane-isolated TES bolometers for far-IR/submillimeter spectroscopy”. In: ed. by Jonas Zmuidzinas et al. Orlando, Florida , USA, June 2006, p. 627508. DOI: 10.1117/12.672036. URL: http://proceedings.spiedigitallibrary.org/proceeding.aspx?doi=10.1117/12.672036 (visited on 03/08/2022).

[10] Matthew Kenyon et al. “Toward a Detector/Readout Architecture for the Background-Limited Far-IR/Submm Spectrograph (BLISS)”. In: *J. Low Temp. Phys.* 176.3 (Jan. 2014), pp. 376–382. DOI: 10.1007/s10909-013-1020-5. URL: https://doi.org/10.1007/s10909-013-1020-5.

[11] Pourya Khosropanah et al. “Ultra-low noise TES bolometer arrays for SAFARI instrument on SPICA”. In: *Millimeter, Submillimeter, and Far-Infrared Detectors and Instrumentation for Astronomy VIII*. Ed. by Wayne S. Holland and Jonas Zmuidzinas. Vol. 9914. Society of Photo-Optical Instrumentation Engineers (SPIE) Conference Series. July 2016, 99140B, 99140B. DOI: 10.1117/12.2233472.

[12] Marcel L. Ridder et al. “Fabrication of Low-Noise TES Arrays for the SAFARI Instrument on SPICA”. In: *J. Low Temp. Phys.* 184.1-2 (July 2016), pp. 60–65. DOI: 10.1007/s10909-015-1381-z.

[13] T. Suzuki et al. “Development of Ultra-Low-Noise TES Bolometer Arrays”. In: *J. Low Temp. Phys.* 184.1-2 (July 2016), pp. 52–59. DOI: 10.1007/s10909-015-1401-z.

[14] Jan van der Kuur et al. “Implementation of frequency domain multiplexing in imaging arrays of microcalorimeters”. In: *Nuclear Instruments and Methods in Physics Research Section A: Accelerators, Spectrometers, Detectors and Associated Equipment* 520.1 (2004). Proceedings of the 10th International Workshop on Low Temperature Detectors, pp. 551–554. ISSN: 0168-9002. DOI: https://doi.org/10.1016/j.nima.2003.11.312. URL: http://www.sciencedirect.com/science/article/pii/S016890020303242X.

Chapter 4

KINETIC INDUCTANCE DETECTORS FOR FAR-INFRARED SPACE ASTROPHYSICS

[1] Logan Foote et al. "High-Sensitivity Kinetic Inductance Detector Arrays for the Probe Far-Infrared Mission for Astrophysics". en. In: *Journal of Low Temperature Physics* 214.3-4 (Feb. 2024), pp. 219–229. ISSN: 0022-2291, 1573-7357. DOI: 10.1007/s10909-023-03041-6. URL: https://link.springer.com/10.1007/s10909-023-03041-6 (visited on 04/12/2024).

[1] Logan Foote et al. "Highly sensitive far-IR KIDs for PRIMA: optical characterization of a 25-micron array". In: *Millimeter, Submillimeter, and Far-Infrared Detectors and Instrumentation for Astronomy XII*. Ed. by Jonas Zmuidzinas and Jian-Rong Gao. Yokohama, Japan: SPIE, Aug. 2024, p. 27. ISBN: 978-1-5106-7527-8 978-1-5106-7528-5. DOI: 10.1117/12.3020228. URL: https://www.spiedigitallibrary.org/conference-proceedings-of-spie/13102/3020228/Highly-sensitive-far-IR-KIDs-for-PRIMA--optical-characterization/10.1117/12.3020228.full (visited on 04/15/2025).

4.1 Introduction

This chapter describes the development of large-format arrays of low-volume Al KIDs to satisfy the requirements of the Probe Far-Infrared Mission for Astrophysics (PRIMA)'s spectrometer, the Far-InfraRed Enhanced Survey Spectrometer (FIRESS). FIRESS is a grating spectrometer that targets the 25 to 235 μm wavelength range and provides a spectral resolution in low-resolution mode of $R = 85 - 150$ and a tuneable spectral resolution in high-resolution mode, with a maximum of $R = 17,000$ at 25 μm and $R = 4,400$ at 112 μm.[5] The requirements for FIRESS detectors are stated in Table 2.1.

Pioneering work at the Netherlands Institute for Space Research (SRON) as part of the EU-funded SPACEKIDs program demonstrated noise equivalent powers (NEPs) below 1×10^{-19} W/$\sqrt{\text{Hz}}$ using a lens-antenna coupled detector with a low-volume Al active element.[3,7] At the short-wavelength end of the FIRESS band, antenna coupling is inefficient due to conductor loss. This chapter describes work done at JPL on KIDs based on multimode absorbers patterned in Al, which provide efficient

coupling down to FIRESS's shortest wavelengths. Subsection 4.2.1 describes low-volume absorber designs that cover the full FIRESS wavelength range. The following subsections describe the fabrication and testing of the long- and short-wavelength limits of the wavelength range. The long-wavelength detectors have met the NEP requirement for FIRESS in kilo-pixel array formats.[18,24,22] The short-wavelength detectors have met the NEP requirement for FIRESS in small test arrays.[12] Kilo-pixel arrays of the short-wavelength detectors are in development.

This work builds on Al KID array development for the Terahertz Intensity Mapper (TIM), a pathfinding mission for far-IR spectroscopy which will deploy thousands of KIDs on a balloon platform.[32] Due to atmospheric loading and absorption, the NEP requirement for TIM KIDs is more than an order of magnitude higher than the FIRESS requirement. Therefore, TIM detectors use larger volume absorbers (~200 μm^3) and can operate at higher temperatures (~250 mK) than FIRESS. TIM also operates at longer wavelengths than FIRESS (240 – 420 μm). Recalling Equation 2.51, the quasiparticle (QP) lifetime is expected to increase as the temperature is lowered, but eventually saturate at τ_{max}. A TIM array was measured in a FIRESS cryostat, and the QP lifetime saturation was found to be τ_{max} ~1 ms. These detectors achieved sensitivities of 1.3×10^{-18} W/$\sqrt{\text{Hz}}$. The FIRESS KIDs achieve better sensitivity through their lower absorber volume and higher QP lifetimes that result from a lower operating temperature. Based on the lifetime measurements from TIM, FIRESS detectors require a factor of ~ 15 reduction in absorber volume to achieve the NEP requirements of 1×10^{-19} W/$\sqrt{\text{Hz}}$, assuming QP noise dominates.

This chapter provides an overview of the development of both the long- and short-wavelength arrays for FIRESS. Following the introduction in Section 4.1, Section 4.2 is an overview of the KID design, Section 4.3 describes the challenges of working with low-volume Al absorbers, Section 4.4 is a description of the experimental setups, and Section 4.5 details measurements of the long- and short-wavelength arrays.

4.2 Design

As detailed in Section 4.5, our long- and short-wavelength arrays with a volume of ~10-20 μm^3 and QP lifetimes of ~1 ms at ~100 mK satisfy the FIRESS NEP requirement. At long wavelengths (> 200 μm), feedhorns are typically used for optical coupling. At the short-wavelength end of the FIRESS band, feedhorn manufacturing is impractical due to surface roughness requirements. We instead

implement Si microlenses across the full FIRESS band, which are fabricated using grayscale lithography and deep reactive ion etching, then bonded to the backside of the KID wafer.[10]

Each of FIRESS's four spectrometer modules will contain two arrays of 1,008 pixels with a 900 μm pixel pitch. The test arrays are laid out in 1,008 pixel flight-like format ("kilo-pixel arrays") or 44-pixel test array format. Subsection 4.2.1 is an overview of the absorber designs, Subsection 4.2.2 is an overview of the capacitor designs, and Subsection 4.2.3 is an overview of the kilo-pixel and 44-pixel array layouts.

4.2.1 Absorbers

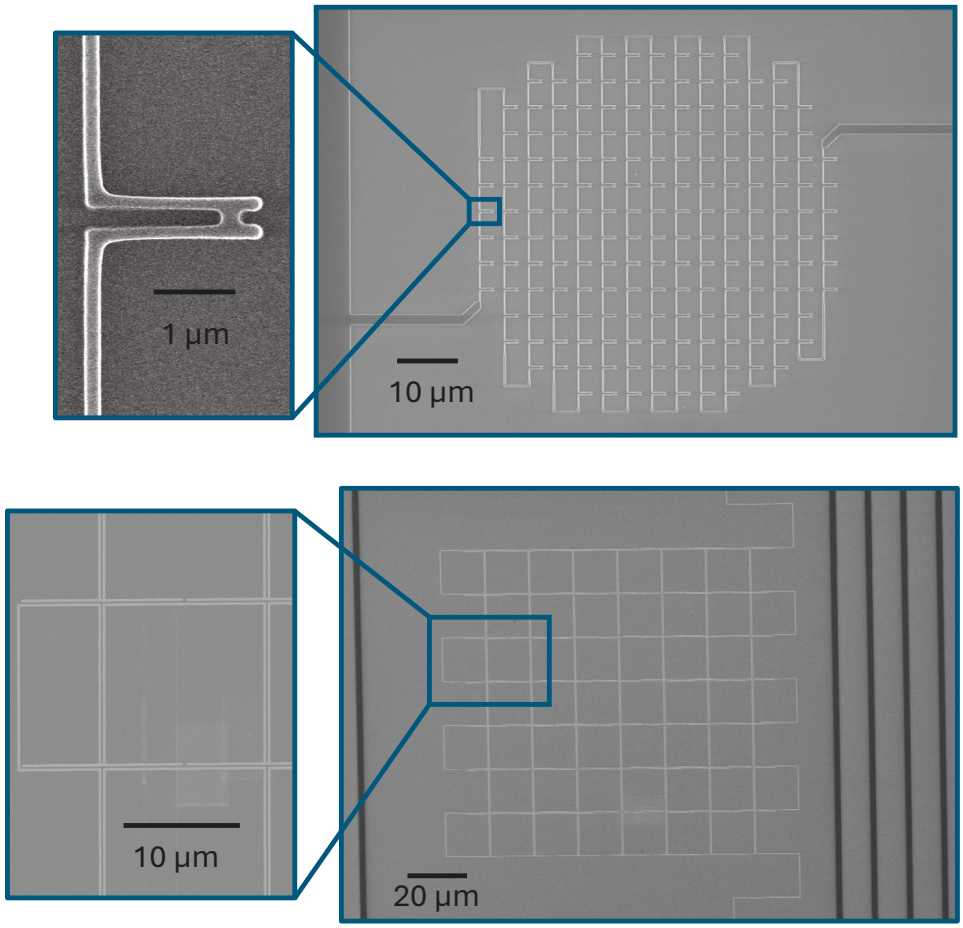

Figure 4.1: SEM images of the short-wavelength hairpin absorber (top) and the long-wavelength 7x7 Π-shaped absorber (bottom). The images are aligned such that S-pol is the horizontal direction and P-pol is the vertical direction.

The absorber must be a single Al meander with sufficiently high kinetic inductance and low volume. The meander must be optimized to absorb both polarizations efficiently at the desired wavelength, and the surface impedance must be matched for illumination through the backside of the silicon substrate. In order to minimize TLS noise, the capacitance values should be minimized, and therefore the inductance of the absorber should be maximized. Since the absorber volume is fixed by design and the absorber line-width is fixed due to fabrication capabilities, the ideal absorber will have 100% of the length contributing to the inductance.

Without a back short, the maximum possible efficiency is $\epsilon_r/(1+\epsilon_r) \approx 77\%$.[12] At the long-wavelength end of the FIRESS band, the absorber meander is a Π-shape, shown in Figure 4.1 (bottom). The absorber is a single meandered line, except for the upper horizontal lines of each Π shape, which do not contribute to the inductance but capacitively couple to the adjacent structures to improve absorption of the vertical polarization. The Al meander is 30 nm thick with a line width of 200 nm, and is fabricated using electron-beam (e-beam) lithography. The simulated absorption versus wavelength of this design is plotted in Figure 4.2 (left). The absorber achieves >60% absorption in both polarizations between 158 and 250 μm. We have studied either 5x5, 6x6, or 7x7 arrays of the Π-shaped structure, corresponding to absorber volumes of 11.3, 15.6, and 20.6 μm^3, respectively. Measurements the 6x6 and 7x7 designs are presented in Section 4.5. For a more detailed description of this Π-shaped absorber design, see Hailey-Dunsheath et al. 2023.[22]

The Π-shaped absorber has also been modified to target shorter wavelengths. The simulated absorption of the modified design is plotted in Figure 4.2 (right), achieving >60% absorption in both polarizations between 83 and 188 μm. This modified design requires 100 nm line widths, which we have successfully fabricated on our short-wavelength devices.

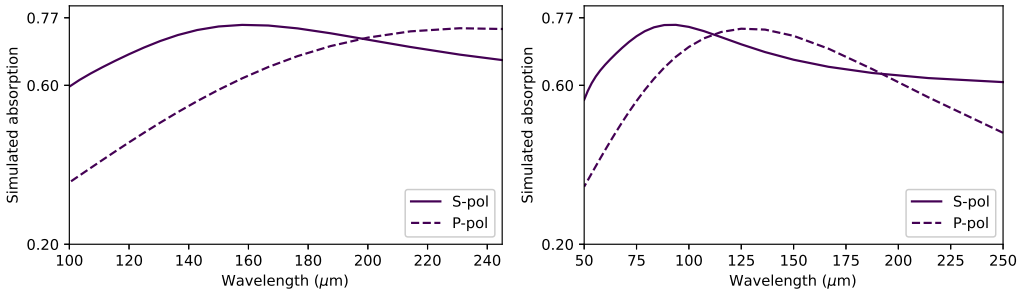

Figure 4.2: Simulated absorption for the Π-shaped absorbers. (Left) the nominal design, with >60% efficiency in both polarizations from 158-250 µm. (Right) the scaled design, with >60% efficiency in both polarizations from 83-188 µm. The polarization directions are indicated in Figure 4.1.

At shorter wavelengths, the Π-shaped structure is no longer a practical design to impedance match because the required Al line widths become too small for fabrication. Instead, the absorber can be designed with resonant structures tuned to the wavelength of interest. The so-called "hairpin" resonant structures are sensitive to both polarizations and can be tuned to wavelengths between 5 and 85 µm. Figure 4.1 (top) is a Scanning Electron Microscope (SEM) image of the hairpin structures, and Figure 4.3 is a plot of the simulated absorption versus wavelength for a several hairpin absorber designs. The Al fabrication is similar to that of the long-wavelength absorber, except the line thickness is 40 nm and the line width is 100 nm. The design tuned to 25 µm with an absorber volume of 11 μm^3 was fabricated, and the transmission was measured in a Fourier-transform spectrometer (FTS) at 5 K (details in Day et al. 2024[12]). The fabricated absorber transmission is centered on 24 µm (4% lower than design) and matches the absorption peak and width closely. For a more detailed description of the hairpin absorber design, see Day et al. 2024[12]

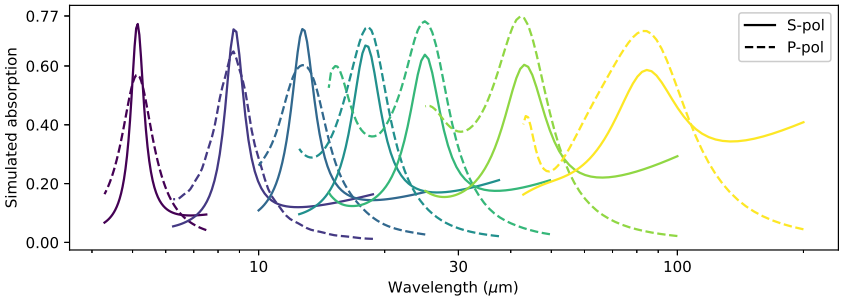

Figure 4.3: Simulated absorption for 7 different hairpin absorbers, optimized for wavelengths ranging from 5 to 85 µm. The colors correspond to the different absorber designs. The polarization directions are indicated in Figure 4.1.

The simulations of Π-shaped absorbers and the hairpin absorbers cover the wavelength range 5-250 μm with ~10-20 μm^3 absorber volumes and efficiencies of at least 60% in both polarizations. The NEP requirement for FIRESS has been demonstrated with the 25 μm hairpin absorber and the 6x6 158-250 μm Π-shaped absorber, as detailed in Section 4.5.

4.2.2 Capacitors

The current version of the arrays uses Nb interdigitated capacitors (IDCs) with 2 μm tine widths and 10 μm tine spacings. The number and effective length of the tines are varied across the arrays to vary the resonant frequency, as detailed in Subsection 4.2.3. IDCs are conventionally used in KIDs due to high TLS noise in parallel-plate capacitors (PPCs) that use conventional dielectric materials. Recent research into low-TLS dielectrics, such as amorphous silicon (a-Si), has renewed interest in the use of PPCs for KIDs.[34,13] As described in Subsection 2.4.3, for a given capacitance, larger capacitor geometries produce lower TLS noise. For FIRESS, the pixel pitch must be small (~1 mm), constraining the ability to increase the IDC geometry. For this reason, early versions of the short-wavelength arrays used Al/a-Si:H/Nb PPCs in an attempt to reduce the TLS noise and crosstalk.[11,17] The PPC short-wavelength arrays achieved good yield, optical efficiency, and fractional frequency noise, but had lower-than expected response due to reduced QP lifetimes (see Subsection 4.3.1). The current version of these arrays use IDCs to ensure that the QP lifetime remains high. An example of the FIRESS IDC capacitors can be seen in Figure 4.4.

4.2.3 Array Layouts

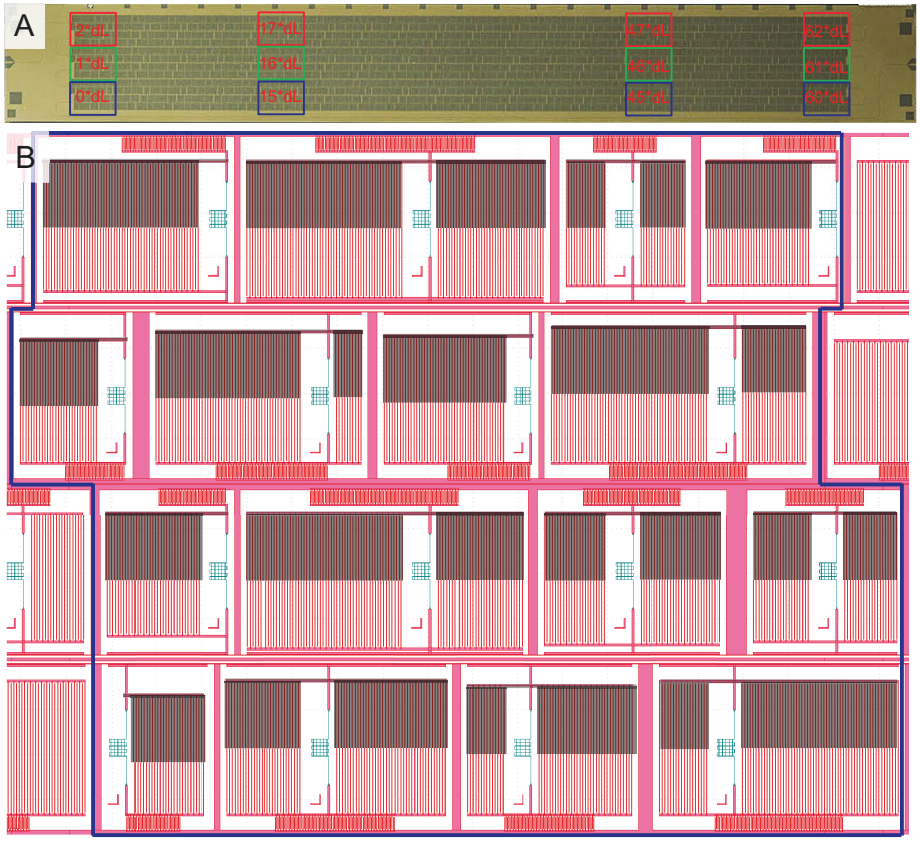

Figure 4.4: Layout of a kilo-pixel long-wavelength FIRESS array. Panel (a) shows a photograph of the 12 x 84 pixel array. Individual pixels can be identified in the Nb (greenish yellow), as can the single CPW transmission line that snakes through the array and has bondpads on left and right side edges. Around the edge, holes are left in the Nb to expose the Si wafer (black squares) and allow space for DC test structures (as seen above the left-most column of resonators). Panel (b) shows the design of the 4 by 4 pixel unit cell (inside blue outline) from which the array is constructed. Each detector consists of an Al (green) absorber/inductor, one or two Nb (red) main IDC capacitors, an IDC capacitor to ground, and a coplanar plate capacitor. The latter couples the KID to the CPW transmission line, which runs below rows 1 and 3. The ⌟ shapes are alignment markers for the absorber patterning.

The layout of the 12 by 84 pixel array is shown in Figure 4.4. The absorber designs presented above are interchangeable in this layout, with only minor modifications to the capacitors to compensate for differences in the absorber inductance. The Nb IDCs and coplanar waveguide (CPW) transmission line, to which all 1,008 KIDs are capacitively coupled, are lithographically patterned using a unit cell approach. The unit cell design, as shown in Figure 4.4 (b), contains an array of 4 by 4 KIDs, each of

which consists of the Al inductor (green elements in Figure 4.4 (b)), one or two main IDCs setting the pixel's resonant frequency, a coplanar plate capacitor near the CPW feedline, and an IDC grounding capacitor. The length of the coupling capacitor is matched to the combined width of the main IDCs to maintain an (approximately) constant capacitance ratio and an expected $Q_c \approx 30,000$. The IDC capacitor to ground provides approximately 10 times the capacitance of the coupling capacitor to the CPW readout line, thereby minimizing its effect on Q_c.

To generate unique resonator frequencies for each detector, the lithographic mask for the Nb components (red elements in Figure 4.4 (b)) is split in two: (1) a mask containing the top half of each of the main IDCs and the horizontal bar connecting the tines (Figure 4.4 (b) shaded regions). (2) a mask containing all other Nb components including the bottom half of the main IDCs, coupling capacitor, grounding IDC, two sections of CPW transmission line (below rows 1 and 3) and ground plane (forming a box around each resonator). The combined number of tines in the main IDCs of each KID in the unit cell is varied between 98 and 27 to create 16 resonances log-uniformly spaced in frequency. The size of the largest capacitor in the array (lowest frequency resonator) is limited by the 900 µm hex-packed pitch, which limits the area available for the main IDCs. This is partially mitigated by allowing low frequency resonators to use IDC space unused by resonators with a smaller IDC (higher frequency). For each consecutive instance of the unit cell, the length of all IDC tines is reduced by an integer number of $dL = 0.7$ µm through the relative position of the two masks. A few examples of the IDC lengths are indicated in Figure 4.4 (a). This creates an array with a uniform design spacing of $\Delta f_r / f_r \sim 6 \times 10^{-4}$.

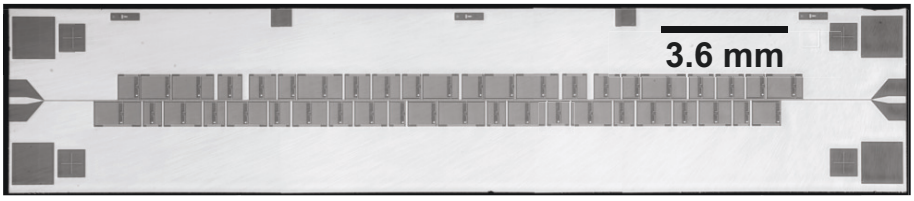

Figure 4.5: Stitched microscope photograph of the 44-pixel chip layout. The single CPW feedline runs in a straight line between the bondpads on the left and right edges of the array.

The 44-pixel chip, for which measurements are presented in Subsection 4.5.2, utilizes the same pixel architecture, but with the pixels laid out on either side of a single

straight transmission line with the same pixel pitch and hexagonal arrangement as the kilo-pixel array. Figure 4.5 is a stitched microscope image of the 44-pixel device layout. For more details on the 44-pixel chip layout, see Day et al. 2024.[12]

The advantage of the unit cell approach presented above is that the pixels in each 16 resonator unit cell are maximally spaced in resonant frequency, so spatial mapping of each pixel in the array can be done by identifying the unit cell to which each resonator belongs. Therefore, unique illumination of each unit cell via a single LED can provide spatial mapping of every pixel.[30,38,36,29] We have developed an array of 63 LEDs to uniquely illuminate each unit cell, and we successfully spatially mapped a long-wavelength array, as detailed in Albert et al. 2024.[1] Accurate placement of resonant frequencies is desirable to reduce collisions between resonances (which decrease the yield). Frequency placement can be improved via laser trimming of capacitors after LED mapping.[31] We intend to use this technique to separate overlapping resonators on FIRESS arrays.

An unintended consequence of the unit cell approach is the so-called "frequency bunching" effect, wherein the resonant frequencies bunch into 16 groups (shown in Figure 4.18), decreasing the median spacing between resonators. The Al film thickness on our 6-inch wafers has a 3% variation from center to edge, leading to alteration of resonator frequencies. The resulting bunching of resonances depends on the location of the chip on the wafer. Chips near the center of the wafer have less bunching ($\Delta f_r / f_r \approx 0.0015 \pm 0.001$) while those at the edges of the wafer have more bunching ($\Delta f_r / f_r \approx 0.006 \pm 0.001$). Two design changes are in progress to attempt to mitigate the bunching effect: (1) The number of arrays per wafer and placement of arrays on the wafer will be modified to minimize the spread in Al thickness across each array. (2) The resonant frequency placement across each array will be rearranged to better match the expected Al thickness profile. Capacitor trimming could also be used to reduce bunching.

Measurements of an early 25 µm array suggested that a high-energy event (e.g. cosmic ray) mitigation technique will be required for the FIRESS arrays. Because the detectors are backside illuminated, a low-T_c Ti grid was added to the arrays to reduce data glitches produced by high-energy events, following the strategy of Karatsu et al. 2019.[26] The low-T_c material mitigates these data glitches by down-converting non-thermal phonons to sub-gap energies, decreasing the number of KIDs that see a glitch for a given high-energy event. Because the arrays described here are backside-illuminated, circular cutouts are made in the Ti grid to allow light

through. These arrays achieve a sufficient level of high-energy event mitigation for FIRESS, as detailed in Kane et al. 2024.[25]

4.3 Challenges of Low-Volume Al

Low-volume Al KIDs present two unique challenges: maintaining a high QP lifetime is difficult and the absorbers experience aging on ~month timescales, likely due to oxidation. The QP lifetime is discussed in Subsection 4.3.1 and the aging effect is discussed in Subsection 4.3.2.

4.3.1 QP Lifetime

The QP lifetime is highly sensitive to Al uniformity: a study on QP lifetimes in Al films found that ion implanting 100 ppm of Mn and Al into an Al film reduces the QP lifetime by a factor of ~10 and ~7, respectively.[2] Because implanted Al ions decrease the QP lifetime almost as much as implanted Mn ions, it appears that this effect is at least in part due to disorder in the film created by the implantation.

Absorbers that are connected directly to Al capacitors can exhibit QP diffusion into the capacitor, while absorbers connected to higher gap capacitors will retain QPs until they recombine. The QP diffusion time is given by

$$\tau_{\text{diff}} = \frac{l^2}{D}, \tag{4.1}$$

where l is the average length to the edge of the absorber and D is the diffusion constant, taken to be 100 cm^2/s.[35] Taking l to be 1/4 the total length of our absorbers, $\tau_{\text{diff}} \sim 10$ µs, so the absorbers that connect directly to an Al capacitor will exhibit lower effective QP lifetimes. In early designs of the short-wavelength arrays that used PPCs, the absorber was connected directly to an Al capacitor plate. Later designs of the PPC arrays used QP plugs. The QP plug types can be categorized as follows: (1) None - the absorber is connected directly to the Al capacitor. (2) Nb gap - the Al absorber and Al capacitor are separated by a small strip of Nb. (3) Proximity effect - The Al absorber and the Al capacitor are directly connected, but with a small segment of Nb covering the Al. Through the proximity effect, the Al under the Nb has a higher gap. This solution is more robust against shorts due to fabrication errors compared to the Nb gap plugs. (4) Intrinsic - The capacitor is Nb, so the connection to the absorber is an intrinsic QP plug. The current array designs all use intrinsic QP plugs.

QP lifetime results at ~125 mK are summarized in Table 4.1. The importance of the Nb plug is clear by comparing the hairpin device without a plug to the hairpin

devices with plugs. The arrays with a-Si in contact with the absorber see a reduced QP lifetime. The long-wavelength array with a-Si deposited on top and the short-wavelength array with IDCs over a-Si saw a factor of ~10 reduction in QP lifetime, suggesting that the QP lifetime reduction is due to the Al to a-Si interface, rather than some other property of the PPC devices. The QP lifetime reduction may be due Silicide formation at the Si:a-Si interface, diffusion of a-Si into Al, or another unknown effect. The only devices that achieve a QP lifetime of ~1 ms use Nb IDCs (and therefore intrinsic QP plugs) without any a-Si, so the current FIRESS arrays will use this architecture.

The early long-wavelength fabrication process was unreliable and produced short QP lifetimes. This process is labelled "A" in Table 4.1. In order to improve the fabrication reliability of the Al lift-off absorbers, the fabrication process was optimized, as detailed in Appendix C. The new fabrication process is labelled "B" in Table 4.1.

Absorber	Capacitor	a-Si placement	QP plug	QP lifetime (µs)
5x5 Π A	Nb IDC	None	intrinsic	110
7x7 Π A	Nb IDC	None	intrinsic	420
6x6 Π B	Nb IDC	None	intrinsic	1,200
7x7 Π B	Nb IDC	None	intrinsic	930
6x6 Π B	Nb IDC	over abs	intrinsic	100
hairpin	PPC	under abs	None	34
hairpin	PPC	under abs	Nb gap	53
hairpin	PPC	under abs	proximity effect	85
hairpin	Nb IDC	over abs	intrinsic	110
hairpin	Nb IDC	None	intrinsic	1,000

Table 4.1: Summary of QP lifetimes for a variety of array designs. All measurements were taken between 100 and 150 mK. All PPCs are Al:a-Si:Nb, which connect to the absorber through the Al plate. The Π-shaped absorbers are further labelled by the fabrications processes A and B detailed in the text.

4.3.2 Aging

The FIRESS low-volume Al absorbers exhibit an aging effect, where the resonant frequency shifts on a timescale of days to months. This aging effect was observed in devices that were tested multiple times over the course of several months after fabrication, and is likely due to oxidation of the Al. Figure 4.6 is a plot of the fractional frequency shift versus time spent in air at room temperature. Note that the fractional frequency shift offset cannot be determined without a model for the

aging effect, so each dataset is offset by the unknown quantity x_1. The first array was a kilo-pixel array with the long-wavelength 7x7 Π-shaped absorber design. The second array contained devices with the short-wavelength hairpin absorber and PPCs, with a-Si covering the absorber. The third array contained two different types of devices: the short-wavelength hairpin absorber with IDCs and a Nb absorber with IDCs. All absorbers on the third array are deposited on top of a-Si. All arrays were kept in the same packaging with the same test setup except the Π-shaped absorber array, which changed packaging between the first and second measurement. The three Al absorber arrays show significant aging. Given the limited number of data points, low statistics, and unknown fractional frequency shift offset, it is difficult to draw conclusions about the relative aging rates, other than to say they are of the same order-of-magnitude for all the Al absorbers.

The Nb control device experiences negligible aging. If the aging of the exposed absorbers is due to oxidation, it is consistent with one to a few monolayers of Al, which is not unreasonable. However, we note that oxidation of Al on these timescales has not been studied in the literature.

The absorber with a-Si over the absorber experiences aging at a rate of the same order as the bare Al absorbers, suggesting some type of long-timescale diffusion of a-Si into Al. However, this dataset is limited so further work is required to confirm these findings. This effect could be related to the low QP lifetime the PPC devices experience. The a-Si aging may be a separate phenomenon that requires further study, but this work is outside the scope of FIRESS detector development.

A new experiment has been set up to track aging more carefully, with an array in a nitrogen purge as control. Results from this experiment will be published in a future work. If the aging effect occurs identically across the array, it would be manageable from an instrument calibration perspective. However, this level of aging causes the resonance ordering to change significantly over the course of $\sim$ 100 days, so it must be reduced to maintain a spatial pixel mapping. The following are several ideas for managing aging.

1. Pre-age the devices in an oxygen rich environment. Once a thick oxide layer has formed, the aging is expected to slow. The efficacy of this method has not yet been tested.

2. Protect the Al from aging by depositing a dielectric on top. The reduction in QP lifetime due to a-Si and the aging we measured in a-Si covered absorbers

suggest that this method will not be possible for our detectors.

3. Keep the detectors in a nitrogen purge through fabrication, testing, and assembly. Nitrogen purges have been used on previous space missions, with total air exposure times of 1–2 months. PRIMA would need tighter requirements, which would be difficult to implement.

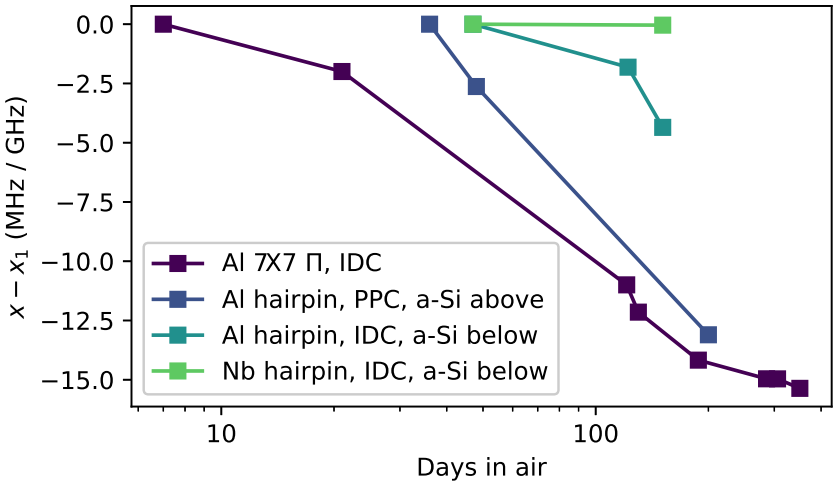

Figure 4.6: Offset fractional frequency shift versus days spent in air at room temperature for four device designs. The offset x_1 is unknown and different for each curve. The first curve (purple) corresponds to the Al 7x7 Π-shaped absorber with IDCs, and the data is averaged across 11 KIDs with frequencies in the range 513-1,200 MHz. The second curve (blue) corresponds to the Al hairpin absorber with PPCs, with the absorber covered in a-Si, and the data is averaged across 4 KIDs in the range 400-1,800 MHz. The third and fourth curves (teal and green) correspond to the array with IDCs and a-Si below the absorber. The third curve (teal) corresponds to the Al hairpin absorber, and the data is averaged over 2 KIDs with frequencies of 844 and 895 MHz. The fourth curve (green) corresponds to the Nb absorber, and the data is averaged over 2 KIDs with frequencies of 2.81 and 3.00 GHz.

4.4 Experimental Setup

Measurements presented in this thesis were performed in three different dilution refrigerator (DR) systems, which will be referred to as DR0, DR1, and DR2. DR0 and DR1 are both BlueFors LD400 fridges, capable of reaching < 10 mK. DR2 is capable of reaching 50 mK. All fridges include magnetic shielding. Unless otherwise specified, measurements in this thesis were performed in DR0. Subsection 4.4.1 describes the blackbody setup, Subsection 4.4.2 describes the RF circuit setup, and Subsection 4.4.3 describes the multi-tone readout systems.

4.4.1 Blackbody Setup

In all fridges, the blackbody is mounted on the 4 K stage with thermal isolation using G10, so that it can be heated to sufficiently high temperatures without disrupting the fridge cooling. Filters are placed in front of the blackbody, followed by an aperture on the 1 K stage. On the cold stage, the detector arrays are mounted in a box with filters directly in front or the arrays. The blackbody setup follows standard stray light mitigation techniques.[4,14] The detector + filter assembly is mounted inside a secondary box, which is coated with a mixture of Epoxy with carbon black and SiC grains. The cold stage, 1 K stage, and 4 K stage have shields which are also blackened to provide further stray light reduction. A model of the DR2 blackbody setup is presented in Figure 4.7. DR0 and DR1 follow the same design principles. The details of the filter stack, blackbody size, and aperture size/placement vary based on the detector design and array format.

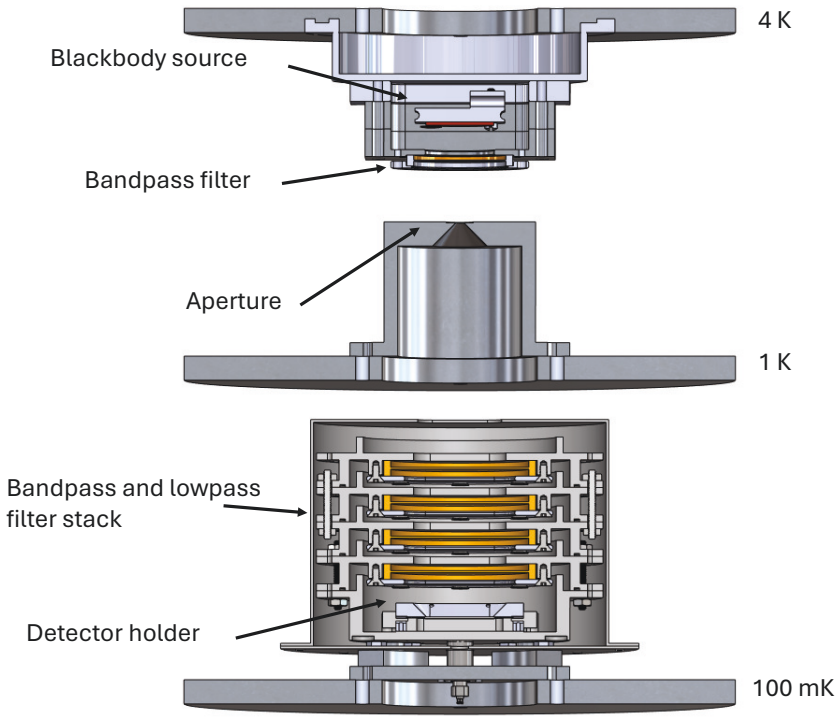

Figure 4.7: Blackbody setup in DR2. The blackbody is mounted on the 4 K stage at the top of the cryostat, with band-pass filters directly in front of the blackbody. An aperture is mounted on the 1 K stage, and the detector + filter assembly are mounted on the cold stage (labelled 100 mK), in a secondary box that is coated with the blackened Epoxy mixture. The 4 K, 1 K, and cold shields are not pictured here.

4.4.2 RF Setup

A schematic of the RF setup for DR0 is presented in Figure 4.8. In DR0, four equivalent RF circuits are installed. DR1 and DR2 have RF circuits that follow similar design principles. The measurements in this thesis use Low Noise Factory LNC0.2_3a and LNC0.2_3b cryogenic High-Electron-Mobility Transistor (HEMT) amplifiers on the 4 K stage as the first stage amplifiers, which produce 30dB of gain in the 0.2-3 GHz range with a noise temperature of 1.6 K. The warm amplifiers were chosen such that the cryogenic amplifier dominates the total amplifier noise.

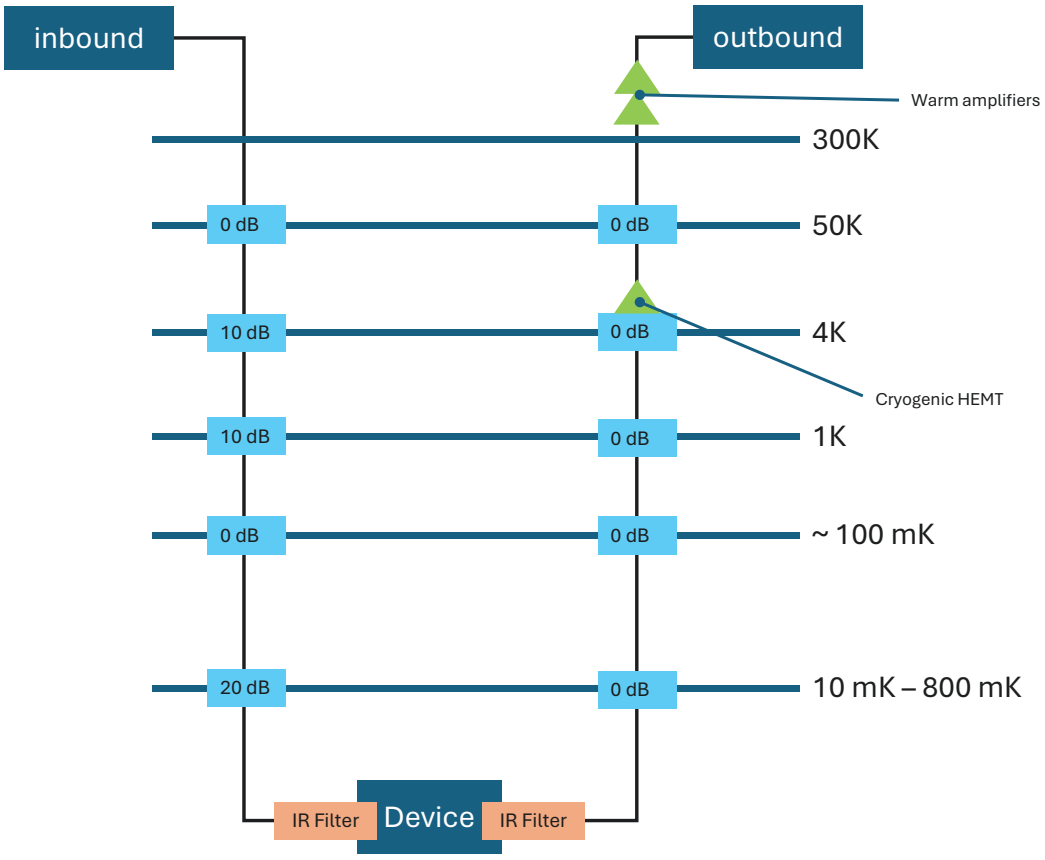

Figure 4.8: Schematic of the RF setup of DR0. Four equivalent RF circuits are installed.

The cables use silver-plated cupronickel as center conductors and cupronickel as outer conductors at temperatures between 4 K and room temperature, and NbTi for both conductors at temperatures below 4 K. The input attenuation is configured to minimize Johnson noise from warm stages. The effective noise temperature at the cold stage is 150 mK when the cold stage is 100 mK. In some early measurements, the

effective noise temperature was reduced to 110 mK with the 4 K and 1 K attenuators increased to 20 dB. However, the increased attenuation requires amplification of the multi-tone system output, so for simplicity, the 4 K and 1 K attenuators are kept at 10 dB for the majority of measurements. Heat sinking is aided by 0 dB attenuators on feedthroughs where attenuators are not otherwise present.

Commercially available IR filters are included at the entrance to the device housing to reduce high-frequency noise. The efficacy of these filters for high-sensitivity KID applications has not been studied in detail, but they are installed nonetheless as a precaution.

4.4.3 Multi-tone Readout

Two multi-tone readout systems were used for measurements in this thesis. Unless otherwise stated, the multi-tone readout system is a Xilinx ZCU111 Radio Frequency System on a Chip (RFSoC) with firmware[37] and software[8] developed for the Cerro Chajnantor Atacama Telescope (CCAT) Prime-Cam instrument.[9] This system will be referred to as the "Prime-Cam readout system". In the current iteration of the firmware, the readout system can measure 1,000 tones in a 500 MHz bandwidth. The Nyquist frequency of the Prime-Cam readout system is 2 GHz. For a standard FIRESS kilo-pixel array, the Nyquist frequency and bandwidth present limitations: resonators near the Nyquist frequency cannot be read out due to the internal filtering, and the array must be read out in four separate measurements to cover the full 2 GHz bandwidth. More recent measurements use the Control and Readout System (CRS) from t0.technology,[33] which uses a third generation AMD RFSoC. The CRS can cover a 2 GHz bandwidth with 4,096 tones across four channels, and has a Nyquist frequency of 2.5 GHz, overcoming both limitations of the Prime-Cam readout system. Software for performing measurements with both the Prime-Cam readout system and the CRS are available in the `citkid` Python repository, developed as a part of this thesis.[16]

4.5 Results

The goal of the FIRESS detector development is to satisfy all the requirements in Table 2.1. The time constants of these detectors are dominated by the QP lifetime (~1 ms for Al), so the time constant requirement is met in all of our detectors. The FIRESS arrays have achieved sufficient cosmic ray mitigation to meet the requirement,[25] which will not be covered here. Therefore, the remaining requirements to demonstrate are: (1) $\mathrm{NEP}^0_{\mathrm{abs}}$, (2) P_{max}, and (3) ν_{min}. KIDs have

naturally high dynamic range, so we expect P_{max} to be satisfied for all of our arrays. P_{max} was measured to exceed the FIRESS requirement by a factor of more than 100 on our short-wavelength devices (see Subsection 4.5.2). Thus, the following section will focus on the NEP requirement, and the readout frequency dependence of the NEP.

These requirements must be demonstrated with flight-like kilo-pixel arrays for at least 800 pixels to satisfy the yield requirement. As described below, the measurements have thus far been limited by the readout system and the tuning procedure. The FIRESS requirements have been met for the subset of pixels read out on long-wavelength kilo-pixel arrays and short-wavelength 44-pixel arrays. The switch to the CRS and improvements to the tuning algorithm provide a promising path forward to achieving these requirements across the full array, with > 750 resonators read out on a recent long-wavelength kilo-pixel device (see Subsection 4.5.4), limited by the fact that the resonant frequencies were placed higher than anticipated and crossed the Nyquist zone of the readout system.

Subsection 4.5.1 is an overview of pair-breaking efficiency measurements, Subsection 4.5.2 describes array-level measurements of the short-wavelength 44-pixel arrays, Subsection 4.5.3 describes array-level measurements of the long-wavelength kilo-pixel arrays, and Subsection 4.5.4 describes a demonstration of the tuning procedure and measurements of correlated noise in the arrays.

4.5.1 Pair-breaking Efficiency

The pair-breaking efficiency η_{pb} is the fraction of photon energy that is converted to QPs, with the rest of the energy lost to phonons. At low photon energies, the pair-breaking efficiency of Al has been calculated to be $\eta_{\mathrm{pb}} = 0.6$.[28] At higher photon energies where pair-breaking phonons can be produced and lost, the pair-breaking efficiency will degrade. Standard methods to decrease the loss from high-energy phonons are: (1) placing the absorber on a membrane to trap phonons[20,3] or (2) introducing a material in between the absorber and the substrate with a low effective phonon cutoff energy.[40] However, the arrays presented here are backside-illuminated, so both of these methods are impractical. The pair-breaking efficiency can be measured through the height of single-photon pulses of known energy, or by comparing QP noise with and without absorbed power.

Pair-breaking efficiency from single-photon pulses

The method for extracting $\eta_{\rm pb}$ using single-photon pulses is described in detail in Kane et al. 2024,[25] and summarized here. The resonance is described by Equation 2.20. The fractional frequency shift and inverse Q shift as a function of QP density are written in Equations 2.44 and 2.45. From these equations, the complex S_{21} timestreams are converted to QP density timestreams. For single-photon pulses, the QP density can be modelled as

$$n_{\rm QP}(T) = n_{\rm QP}(t=0)e^{-t/\tau_{\rm QP}}, \tag{4.2}$$

where $t = 0$ is determined by extrapolating backwards from the pulse decay to compensate for the resonator response time. The equilibrium value of $n_{\rm QP}$ is calculated using Equation 2.32 with $\mu^* \to 0$ and $\Delta \to \Delta_0$. The pair-breaking efficiency is then given by

$$\eta_{\rm pb} = \frac{n_{\rm QP}(t=0)V\Delta_0}{h\nu_{\rm photon}}. \tag{4.3}$$

Pair-breaking efficiency from noise measurements

The QP noise is given in Equation 2.118, and can be rewritten in the more convenient form following Hailey-Dunsheath et al. 2023.[22] For $P_{\rm abs} = 0$,

$$S_{xx}^{\rm QP,thermal} = \left(\frac{\partial x}{\partial n_{\rm QP}}\right)^2 \left[\frac{4n_{\rm QP}\tau_{\rm QP}}{V}\left(1 + \frac{\tau_{\rm QP}}{\tau_{\rm max}}\right)\right]. \tag{4.4}$$

In the limit where the optically excited QP noise dominates over the thermal QP noise,

$$S_{xx}^{\rm QP,optical} = \left(\frac{\partial x}{\partial n_{\rm QP}}\right)^2 \frac{1}{2}\left[\frac{4n_{\rm QP}\tau_{\rm QP}}{V}\left(1 + \frac{\tau_{\rm QP}}{\tau_{\rm max}}\right)\right]\left[\left(\frac{\eta_{\rm pb}h\nu_{\rm photon}}{2\Delta_0}\right) + 1\right]. \tag{4.5}$$

For conserved $n_{\rm QP}$, the ratio of the optical to thermal QP noise is

$$\frac{S_{xx}^{\rm QP,optical}}{S_{xx}^{\rm QP,thermal}} = \frac{1}{2}\left[\left(\frac{\eta_{\rm pb}h\nu_{\rm photon}}{2\Delta_0}\right) + 1\right]. \tag{4.6}$$

Therefore, the pair-breaking efficiency can be measured by comparing QP noise that is dominated by absorbed power to the dark QP noise while ensuring conservation of $n_{\rm QP}$ through measurements of the QP lifetime.

Pair-breaking efficiency results

The pair-breaking efficiency was measured at three different wavelengths: 210 µm using the noise method, 25 µm using the noise method and the single-photon method, and 1.55 µm using the single-photon method. The measurements were performed on three different devices with similar inductor volumes, but the absorber design is not expected to affect the pair-breaking efficiency. The results are presented in Table 4.2. Unsurprisingly, η_{pb} increases as a function of wavelength, approaching the theoretical value of 0.6 at 210 µm. At 25 µm, the noise method and the single-photon method were both implemented and found to be in good agreement with each other.

Absorber	Method	Wavelength	η_{pb}
7x7 Π-shaped	noise	210 µm	0.5[22]
hairpin	noise and single-photon	25 µm	0.3[12]
hairpin	single-photon	1.55 µm	0.1[25]

Table 4.2: Pair-breaking efficiency measurements of FIRESS detectors at three difference wavelengths. For more details on each measurement, see the papers cited in the table.

4.5.2 Short-wavelength Results

The current iteration of the short-wavelength array design uses the 25 µm hairpin absorber with Nb IDCs, thereby avoiding a-Si entirely on the wafer and consistently achieving a QP lifetime of ~1 ms. These detectors are sensitive enough to detect single 25 µm photons. This subsection details measurements of one of these 44-pixel arrays. The measurements were performed in DR2, and multi-tone measurements were performed with the Prime-Cam readout system. One pixel from this array was characterized in Day et al. 2025.[12] Key results from this paper follow. Unless otherwise stated, the measurements were performed at a bath temperature of 150 mK.

1. The detector is capable of counting single photons at 25 µm. Using an optimal filtering technique, photon pulse heights and decay times were extracted. The photons have exponential decays, dominated by the QP lifetime. The signal-to-noise of the pulses is high enough to accurately distinguish between photon pulses and noise. The single-photons allow for a robust measurement of the efficiency through the photon count rate at low blackbody powers, as an

alternative the conventional method of fitting $\mathrm{NEP}_{\mathrm{abs}}$ versus P_{abs} to Equation 2.5. The efficiency is found to be 0.46 from the photon count rate.

2. The QP lifetime is extracted by fitting to noise spectra as a function of blackbody power, and found to saturate at 1.1 ms at $P_{\mathrm{abs}} = 0$. The QP lifetime was also measured by fitting to the decay from single-photon pulses, and found to be 1.02 ms.

3. The absorber volume is 11 $\mu\mathrm{m}^3$, so, in combination with the long QP lifetimes, an NEP below 1×10^{-19} $\mathrm{W}/\sqrt{\mathrm{Hz}}$ is expected. The NEP reached a minimum of 4.6×10^{-20} $\mathrm{W}/\sqrt{Hz}$ at 30 Hz, and satisfies $\mathrm{NEP} < 1 \times 10^{-19}$ $\mathrm{W}/\sqrt{\mathrm{Hz}}$ at readout frequencies as low as 15 mHz.

4. The device remains photon shot-noise limited up to about 100 fW, exceeding the FIRESS requirement for P_{max} by a factor of 100.

5. The pair-breaking efficiency was measured using both the noise and single-photon methods discussed in Subsection 4.5.1. The methods are in good agreement, with $\eta_{\mathrm{pb}} = 0.28$ using the noise method, and $\eta_{\mathrm{pb}} = 0.32$ using the single-photon method.

6. The detector is stable down to $\sim$ 10 mHz at absorbed powers as low as 0.6 aW and $\sim$ 1 mHz at powers of 3.5 fW, far exceeding stability requirements for FIRESS, which were set in part due to stability limitations of previous detector candidates. This stability relaxes requirements on the PRIMA modulation mechanism, and could enable future science cases that require high stability, such as line intensity mapping[27] or planetary atmosphere transits.[6]

For more details on these single-pixel measurements, see Day et al. 2025.[12] Here, these pioneering results are extended to a multiplexed framework with the same 25 µm 44-pixel array and the same test setup. Response and noise measurements are presented to provide a comparison of the multi-tone and single-tone readout performance. The sensitivity is demonstrated at array-level. The multi-tone readout offers the benefit of encoding any frequency instability (due to the readout system, amplifiers, magnetic pickup, temperature drifts, etc.) into multiple channels, so it can be identified and removed. Correlated noise removal can be used in flight with PRIMA. Excess long-timescale correlated noise in the multi-tone system is overcome to reveal fundamental device noise which meets or exceeds that obtained with the single-tone system. The following results were first published in Foote et

al. 2024,[19] but the analysis is modified here to use the correlated noise removal scheme in Appendix D.

Once the testbed is dark enough to permit sub-1×10^{-19} W/$\sqrt{\text{Hz}}$ sensitivities,[14,4] the most challenging aspect of characterizing very sensitive KIDs is to extract the low-power responsivity. While straightforward on orbit with a modulation mirror that can chop between source of known flux and the surrounding sky, extracting the responsivity is more difficult in our current test facilities which do not have fast modulation capability with the radiometrically calibrated blackbody source. Blackbody sources necessarily have low power dissipation and thus long (~hour) thermalization timescales. Fitting of measured fractional frequency shifts to Mattis-Bardeen models after sweeping through a range of temperatures spanning many orders of magnitude in power is often used to extract the responsivity.[21,4,24] However, such measurements are not extremely sensitive to the response at the low-power limit, particularly when there is substantial frequency drift in the run of measurements at different blackbody powers. These difficulties can be overcome by averaging over several blackbody power sweeps, which is time-consuming. As we show in Day et al. 2024, by connecting photon arrival rates to total power, the blackbody modulation method provides a faster measurement of the responsivity in the low-power limit than the conventional fit to x versus P_{abs}.

Array layout

The array yielded 42 out of 44 pixels with resonant frequencies between 570 and 1,120 MHz. Due to the 500 MHz bandwidth of the Prime-Cam readout system, only 38 of the 42 yielding resonators were measured. Of the 38 in-band resonators, the data from one resonator was rejected because the tone power was too low, and the data from two were rejected because they were highly overlapping. Of the remaining 35, 28 have microlenses and 7 are unlensed. The device at 602 MHz was studied in detail with the single-tone system in Day et al. 2024.

Responsivity

The responsivity is measured using the blackbody modulation technique described in Day et al. 2024. We use the same blackbody temperature settings, producing the same power differences. The long-timescale drift present in the multi-tone data is frequency-independent, so it can be removed using the correlated noise removal

scheme describe in Appendix D. An example of the x timestreams for the 602 MHz lensed, unlensed correlated component, and the subtraction is shown in Figure 4.9.

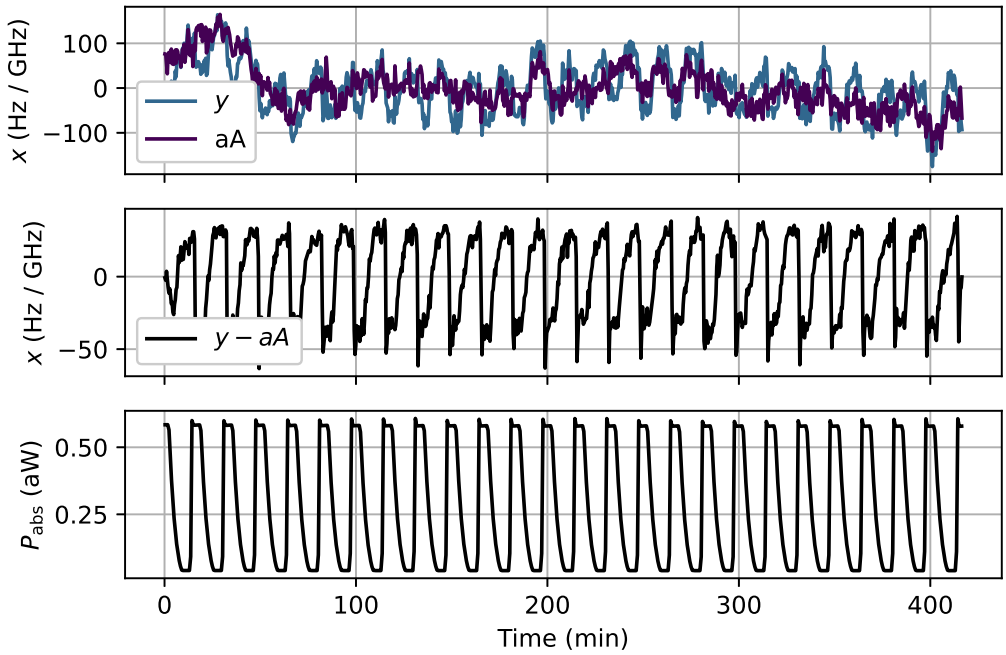

Figure 4.9: Fractional frequency shift x and blackbody power timestreams with the blackbody modulating at 0.3 aW. (Top) 602 MHz lensed detector timestream and average of unlensed detector timestreams. The notation from Appendix D is adopted, where y is the lensed detector timestream and aA is the matrix multiplication of the components a_{kc} and unlensed common timestreams A_{ct} at the index k corresponding to y. (Middle) subtraction of the correlated components from the 602 MHz lensed timestream. (Bottom) blackbody power timestream, where the absorbed power is calculated using the temperature of the blackbody, the system efficiencies, and the efficiency measured using the photon count rate.

The fractional frequency shift modulation amplitude δx is measured by averaging over all periods of the blackbody oscillation, then extracting the peak-to-peak signal height. A small correction factor is applied to the measured δx value to account for the unlensed detector response to incident power, which was measured to be 7 times lower than the lensed detector response to incident power at high powers. δP is measured similarly using the blackbody power timestream. The efficiency factor of the 602 MHz detector, as measured through single-photon counts using the single-tone system, is adopted for all the lensed detectors. The geometry dependence of the blackbody illumination is negligible across this small array, but becomes important for the kilo-pixel arrays. A comparison of the responsivity measurement with the

multi-tone system to the single-tone system for the 602 MHz detector is plotted in Figure 4.10. The responsivities are consistent between the two measurement systems for the range of P_{abs} studied.

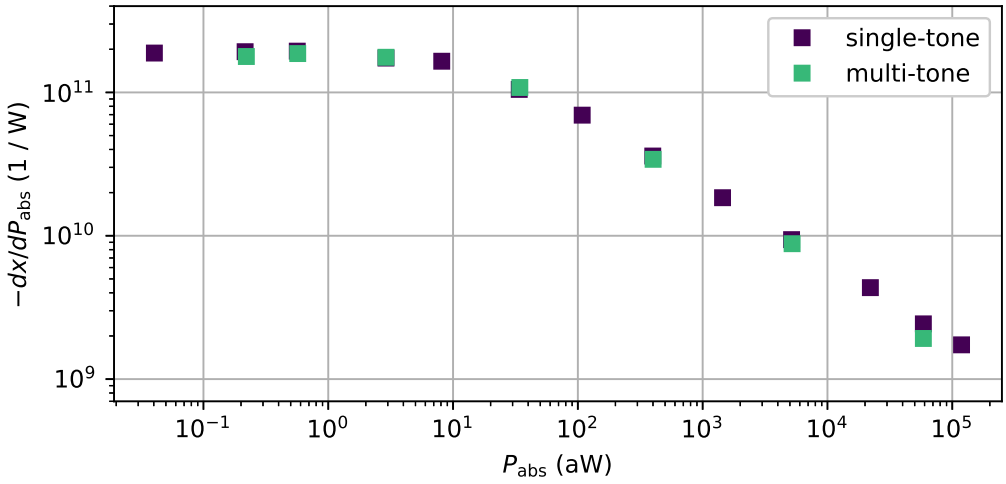

Figure 4.10: Responsivity at $\nu = 0$ versus P_{abs} for the 602 MHz resonator, extracted using the single-tone and multi-tone systems.

The responsivity at $P_{\text{abs}} = 0$ is plotted as a function of resonant frequency in Figure 4.11. The mean responsivity is 2.0×10^{11} 1/W.

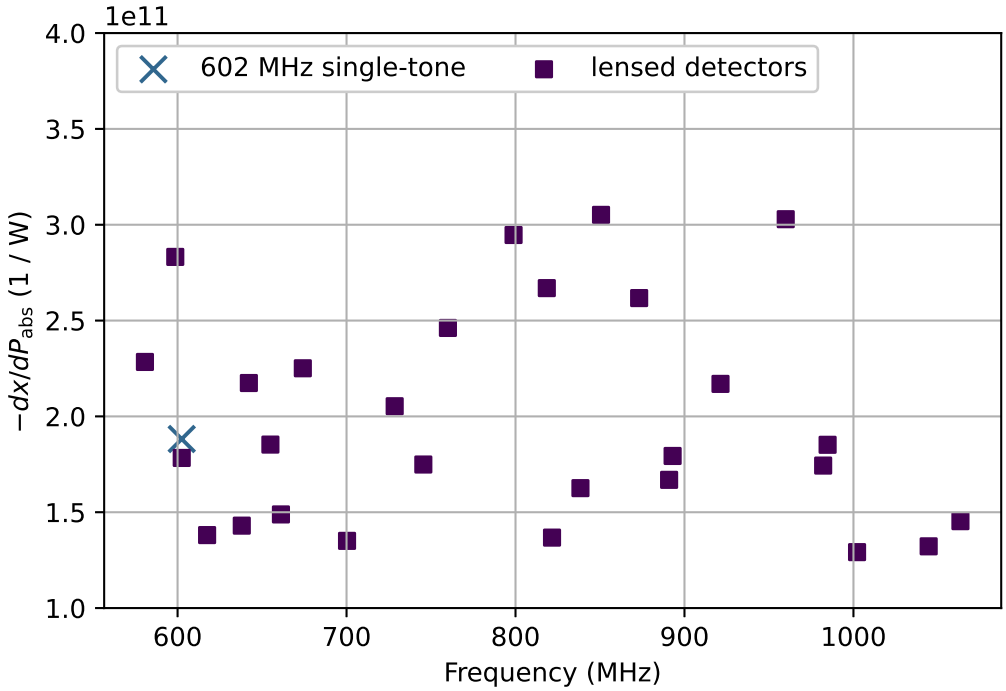

Figure 4.11: Responsivity at $\nu = 0$ and the lowest blackbody power versus resonant frequency. The single-tone measurement of the 602 MHz detector is also plotted for comparison.

NEP

A comparison of NEP spectra using the single-tone and multi-tone systems is plotted in Figure 4.12. The long-timescale drift present in the multi-tone data manifests as a 1/f component in the noise PSD. This 1/f noise is not present in the single-tone data, and will be discussed further in Subsection 4.5.4. The 1/f component is common, and can be removed with the correlated noise removal scheme detailed in Appendix D. The correlated noise removal scheme also removes the pulse tube harmonics. After correlated noise removal, the noise spectrum agrees with the single-tone measurement. Correlated noise is removed for the remainder of the NEP measurements.

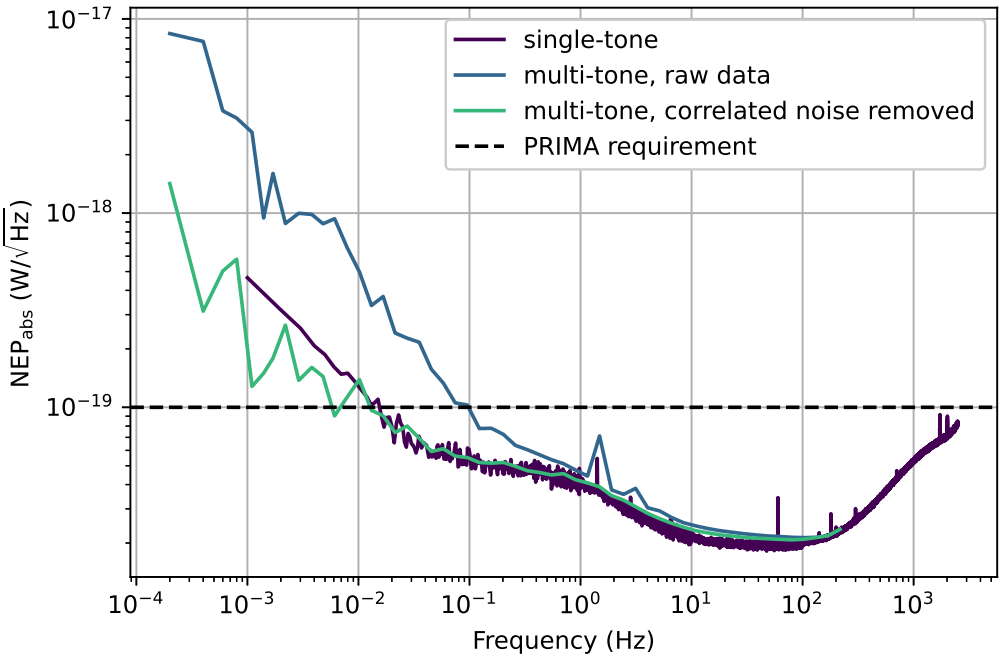

Figure 4.12: The NEP referred to absorbed power, $\mathrm{NEP_{abs}}$, versus frequency, as measured by the single-tone system and the multi-tone system with $P_{\mathrm{abs}} = 0$. Also plotted is the spectrum of the multi-tone data after correlated noise removal, which agrees with the single-tone measurement across the measured frequency range.

The NEP at 10 Hz versus power is plotted for the 602 MHz resonator in Figure 4.13. The results are in good agreement, although the multi-tone data has higher scatter due to the impact of correlated noise on both the responsivity and the S_{xx} spectra.

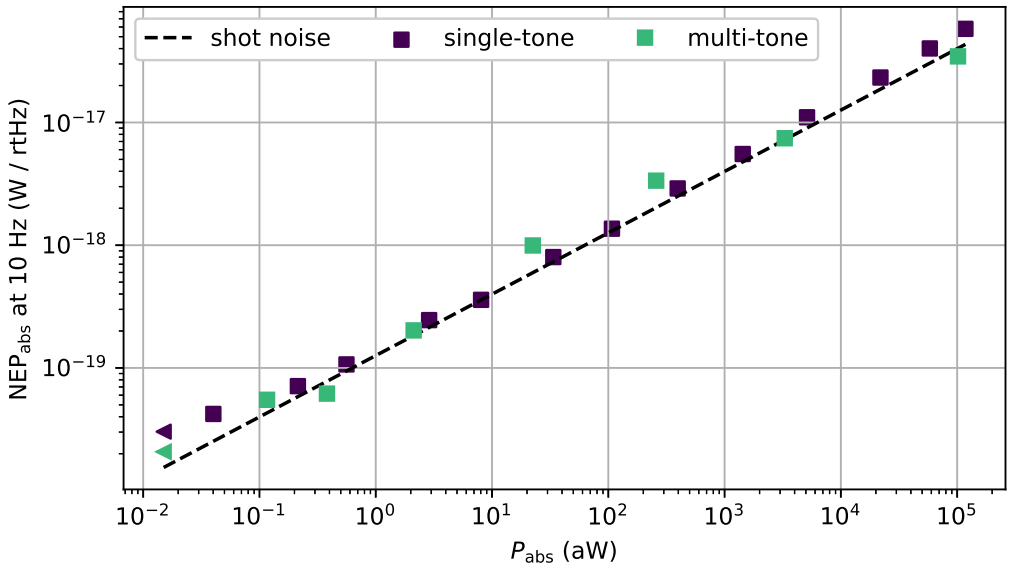

Figure 4.13: NEP$_{abs}$ averaged at 8-12 Hz versus P_{abs} at the lowest blackbody power for the 602 MHz detector. Results from the single-tone and multi-tone measurements are both plotted, with the photon shot noise line for reference.

The NEP at 0.1 and 10 Hz versus resonant frequency is plotted for the lensed detectors in Figure 4.14. All the detectors achieve an NEP below the FIRESS requirement of 1×10^{-19} W/$\sqrt{\text{Hz}}$ at both readout frequencies. The mean NEP is 2.4×10^{-20} W/$\sqrt{\text{Hz}}$ at 10 Hz and 5.9×10^{-20} W/$\sqrt{\text{Hz}}$ at 0.1 Hz.

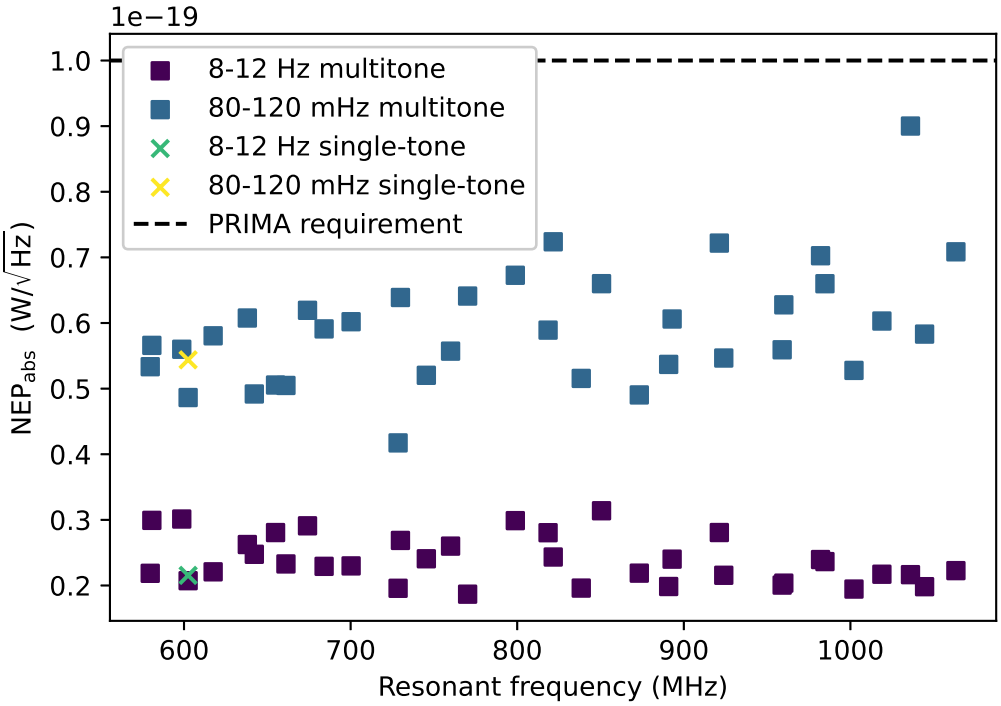

Figure 4.14: NEP_{abs} at 0.1 and 10 Hz versus resonant frequency at the lowest blackbody power for lensed detectors. Results from the single-tone and multi-tone measurements are both plotted for the 602 MHz detector.

Discussion

NEPs surpassing the FIRESS requirement were demonstrated for our 44-pixel 25 µm KID array using multi-tone readout. This measurement technique can be scaled up to kilo-pixel arrays. The detector responsivity was measured using the blackbody modulation technique, which is faster than the conventional method of fitting to x versus P_{abs}. The multi-tone data has low-frequency fractional frequency noise that is correlated, and can be removed following the method described in Appendix D. The source of the correlated noise will be discussed in Section 4.5.4.

Looking forward, a readout system with a faster sample rate will enable photon counting at the array level. While not required for science or calibration with PRIMA, photon counting is a powerful long-term capability which may eliminate some aspects of system noise for faint sources. Full-array photon-counting readout is well within the logical capabilities of the RFSoC systems.

4.5.3 Long-wavelength Results

Results of long-wavelength kilo-pixel array testing are presented here, for both the 7x7 and 6x6 Π-shaped absorber designs with the optimized fabrication process that produces ~ 1 ms QP lifetimes (see discussion in Subsection 4.3.1). The data for the 7x7 Π-shaped absorber were first published in Foote et al. 2023,[18] and are presented here with the addition of correlated noise removal following the algorithm presented in Appendix D. The data for the 6x6 Π-shaped absorber were first published in Kane et al. 2024,[24] and the NEP results will be presented at the end of this subsection to compare to the 7x7 Π-shaped absorber results.

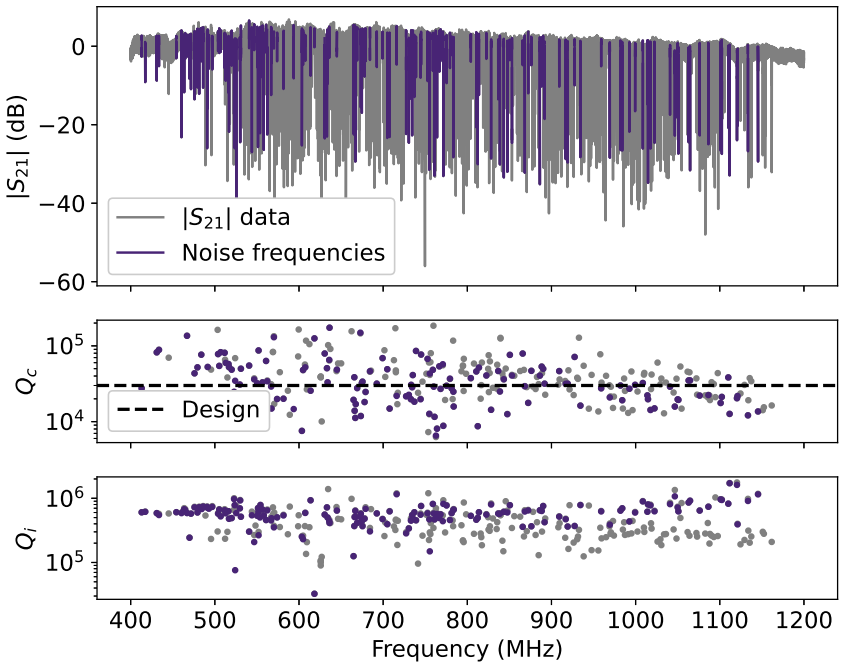

Figure 4.15: $|S_{21}|$, Q_c, and Q_i versus resonant frequency. Purple data corresponds to detectors for which NEPs were measured. Resonances were not found below 400 MHz or above 1,200 MHz.

Array layout

A 1,008 pixel array prototype without microlenses was measured in DR1. Without lenses, radiation enters the wafer through the backside with a circular aperture for each pixel defined by holes in the Ti grid. The array is cooled to a temperature of 125 mK for the measurements presented here. The absorber is a 7x7 Π-shaped design, and the layout is described in Subsection 4.2.3. The Prime-Cam readout system is used for multi-tone measurements.

A measurement of S_{21} versus readout frequency is presented in Figure 4.15. 941 out of 1,008 resonances were found, corresponding to a fabrication yield of 93%. The resonant frequencies fall within 400-1,200 MHz (compared to the design of 400-2,400 MHz). A 10 nH inductor was assumed during design. However, based on the measurements presented here, as well as measurements of arrays using the same layout in combination with different absorbers, we conclude that the inductance is higher and modify capacitors in future arrays accordingly.

Quality factors at the base blackbody temperature of 5.4 K are also plotted in Figure 4.15. The median quality factors are $Q_i = 480,000$ and $Q_c = 32,000$, matching the design value of $Q_c = 30,000$, and the observed spread is within fabrication tolerances.

These were the first kilo-pixel array noise measurements performed with the Prime-Cam readout system, so we used a simple tuning algorithm with limited success. The following response and NEP measurements were acquired for 171 pixels on the array (indicated in purple in Figure 4.15). We conservatively rejected 266 out of 941 resonators with a spacing closer than 200 kHz to avoid any collided resonators and to ensure a robust operation of our analysis code. Data for another 504 resonators were rejected due to improper tuning. The remaining 171 resonators are representative of the full array, based on the resonant frequencies and quality factors.

The resonant frequency at each blackbody temperature is determined using a fit to the nonlinear resonance model described in Appendix B. The fractional frequency shift x with respect to the lowest blackbody temperature ($T_{\rm bb} = 5.4$ K) is plotted as a function of $P_{\rm abs}$ in Figure 4.16 (left) for one detector. The responsivity is found by fitting this data to Equation 2.73.

Responsivity

A frequency sweep of S_{21} and a 200 s on-resonance timestream is obtained for each of the detectors as a function of blackbody temperature (5.4-30 K). The incident power on our detectors is estimated from the blackbody temperature, filter transmission and setup geometry. The power absorbed by the detectors, $P_{\rm abs}$, is then determined from the photon shot noise at high blackbody temperatures, following the methodology of Janssen et al. 2013.[23] The NEP referred to absorbed power, $\mathrm{NEP}_{\rm abs}$, is plotted as a function of $P_{\rm abs}$ for one detector example in Figure 4.16 (right). This data is well described by QP noise (Equation 2.118). At low powers, the thermal QP noise dominates, and at high powers the photon noise dominates.

The maximum blackbody temperature was 30 K, corresponding to an absorbed power of 85 aW. The blackbody used for these measurements has a relatively large volume of copper which cannot be heated further without depositing too much power on the 4 K stage of the DR. The blackbody used for the measurements in Subsection 4.5.2 was much smaller in volume, but is not large enough for the kilo-pixel arrays. A new blackbody with significantly reduced volume has been designed and fabricated for kilo-pixel array measurements to overcome this limitation.

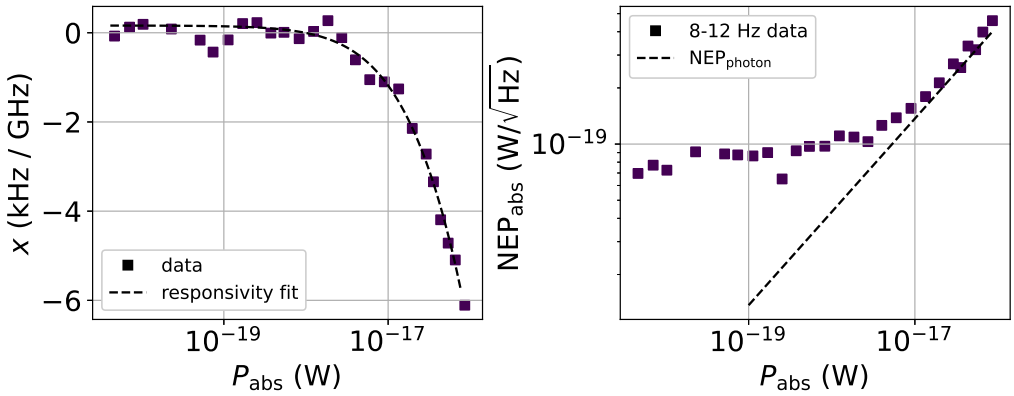

Figure 4.16: (Left) Single detector example of the fractional frequency shift (referred to the lowest blackbody power) versus absorbed power, with the fit to the responsivity model. (Right) NEP_{abs}, averaged at readout frequencies of 8-12 Hz, versus absorbed power. The dashed line indicates the photon noise component.

NEP

After further development of the tuning algorithm, a 6x6 Π-shaped inductor kilo-pixel array was measured following the procedures above. The data is presented in Kane et al. 2024,[24] and the key results are summarized here. The array layout is similar to the 7x7 array, but with decreased capacitance values to account for the higher-than-expected inductance observed in the 7x7 array. Due to an issue related to the ion mill tool which was later resolved, this array only had a fabrication yield of 585, with 436 resonant frequencies within the first Nyquist zone of the Prime-Cam readout system. 295 resonators were read out, with the rest rejected due to poor tuning, overlaps, or data glitches. This measurement yield of $295/436 = 68\%$ marks a significant improvement in tuning capabilities compared to the simple tuning algorithm used with the 7x7 detectors, though still far from the FIRESS requirement of 800 pixels, in part due to the low fabrication yield. The median quality factors are $Q_c = 19,300$ and $Q_i = 86,000$, both lower than the 7x7 detectors. The lower

coupling quality factor is a result of the difference in inductance and other associated design changes.

Figure 4.17 is the histogram of the detector limited NEP at the lowest blackbody power at 0.1 and 10 Hz for the 6x6 and 7x7 Π-shaped absorbers. The 6x6 dataset had a much larger excess correlated noise than the 7X7 dataset. The source of the correlated noise is unknown, but may be due to a loose GE varnish connection. Correlated noise is discussed further in Subsection 4.5.4. The responsivity roll-off due to the QP lifetime is negligible at these readout frequencies. The correlated noise removal algorithm described in Appendix D is applied to this data, using the same parameters for both datasets.

Time constants were measured for a single pixel on each array and found to be 930 µs for the 7x7 detector and 1,150 µs for the 6x6 detector. The designed volumes are 15.6 μm^3 for the 6x6 Π-shaped absorber and 20.6 μm^3 for the 7x7 Π-shaped absorber. The mean of the NEP for the 7x7 array is 4.7×10^{-20} $W/\sqrt{Hz}$ at 10 Hz and 3.3×10^{-19} $W/\sqrt{Hz}$ at 0.1 Hz. The mean of the NEP for the 6x6 array is 6.3×10^{-20} $W/\sqrt{Hz}$ at 10 Hz and 2.4×10^{-19} $W/\sqrt{Hz}$ at 0.1 Hz. Based on the volume and QP lifetime scalings in Equations 2.118 and 2.117, the 6x6 detectors are expected to have a NEP^{QP} of 0.7 and NEP^{TLS} of 0.6 times that of the 7x7 detectors, compared to the measured ratios of 1.4 at 10 Hz and 0.7 at 0.1 Hz. This discrepancy is likely due to the excess correlated noise in the 6x6 dataset, which cannot be removed completely.

The 7x7 array achieves an NEP of $\leq 1 \times 10^{-19}$ $W/\sqrt{Hz}$ for 92% of the array at 10 Hz. These results differ from those in Foote et al. 2024[18] due to the correlated noise removal. The 6x6 array also achieves an NEP of $\leq 1 \times 10^{-19}$ $W/\sqrt{Hz}$ for 92% of the array at 10 Hz. These results are consistent with those in Kane et al. 2024,[24] though the correlated noise removal procedure differs.

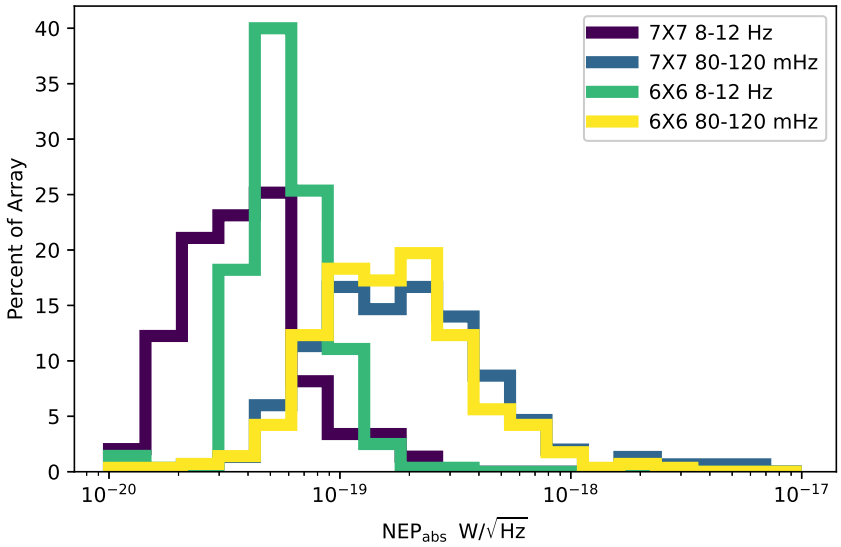

Figure 4.17: Histogram of NEPs for the kilo-pixel arrays with 6x6 and 7x7 Π-shaped absorbers, averaged at 0.08-0.12 and 8-12 Hz.

Discussion

The design, initial characterization and array-level performance statistics of two flight-like long-wavelength FIRESS array were presented, using the 7x7 and 6x6 Π-shaped absorber designs. We find 941 resonances on the 7x7 array, corresponding to a fabrication yield of 93%, and 585 resonances on the 6x6 array, corresponding to a fabrication yield of 58%. The readout bandwidth and quality factors are consistent with the respective designs and match the instrument requirements. Using the Prime-Cam readout system we measured the noise and response for a subset of 171 KIDs on the 7x7 array and 295 KIDs on the 6x6 array. The 7x7 dataset used a simple tuning scheme, which resulted in significant number of KIDs that did not have optimized tone powers and frequencies. The 6x6 dataset represents the first attempt to use a more sophisticated tuning algorithm. Further progress on the tuning algorithm, which resulted in a measurement of $>$ 750 resonators, is discussed in Subsection 4.5.4. Both arrays surpass the FIRESS NEP requirement for $>$ 90% of the array at 10 Hz, corresponding to a modulation frequency well within the capabilities of PRIMA.

4.5.4 Tuning Demonstration and Correlated Noise

The measurements in Subsection 4.5.3 achieved measurement yields of 171 / 941 = 18% and 295 / 585 = 50% using simple tuning algorithms with the Prime-Cam

system. FIRESS will require a measurement yield of at least 800 pixels that achieve the NEP requirement. Assuming 92% of the array achieves the NEP requirement, as measured in Subsection 4.5.3, more than 870 KIDs must be simultaneously read out. The limitations of the Prime-Cam system discussed in Subsection 4.4.3 were overcome by switching to the CRS. To demonstrate these new capabilities, a kilo-pixel array was measured in DR0 in a dark housing. This array uses a new absorber design aimed at reducing the volume of Al that does not contribute to the inductance. However, this design was found to have poor absorption efficiency, so NEP measurements were not performed. Unless otherwise stated, these measurements were performed at 50 mK.

The tuning scheme described in Appendix E is used for these measurements. Manual intervention was required for resonators for which the fit to the resonance model was unsuccessful. This manual intervention is time-consuming, and therefore was not performed for the previous long-wavelength measurements, contributing to the decrease in measurement yield. The "distance" method was used to optimize tone frequencies, to ensure robust operation under data glitches and noise. Improvements to the CRS firmware following this measurement have reduced data glitches (e.g., deglitching is performed on the CRS before averaging down the sweep data to send to the data acquisition computer). As the data quality improves, the tuning algorithm can switch to the "spacing" method for frequency optimization, which should increase the measurement yield.

The array had a fabrication yield of 988, and the frequencies range from 850 MHz to 3.1 GHz, a factor of ~1.4 higher than design. This array exhibits the frequency bunching effect described in Subsection 4.2.3, as seen in Figure 4.18. Fortunately, the CRS Nyquist frequency fell on an area of sparse frequency placement, so only 10 resonators were rejected from the first Nyquist zone due to proximity to the Nyquist frequency. 42 resonators were rejected from the second Nyquist zone due to proximity to the Nyquist frequency. The larger number of rejected resonators in the second Nyquist zone are attributed to suboptimal filtering, which causes aliased resonators from the first Nyquist zone to appear. Of the remaining resonators, 51 were rejected due to proximity to neighboring resonators, and 119 were rejected due to improper tuning. An amplifier noise clearance of 3 dB or greater was used as the criterion for rejecting resonators based on poor tuning. The measurement yield was therefore 766 / 988 = 78%, a significant improvement over the previous measurements using the Prime-Cam board, though still falling

short of the 870 resonator yield required for FIRESS. With an array that meets the design frequency scheduling (and therefore does not cross the Nyquist frequency), an estimated 42 resonators could be recovered. The switch to the "spacing" method for frequency tuning as the CRS firmware improves and the development of a more efficient manual intervention procedure should further increase the measurement yield. Additionally, some KIDs with tone powers that are too low could still be read out with NEPs dominated by amplifier noise. These KIDs have been rejected from the datasets presented in this thesis to ensure that the results are representative of the fundamental detector performance.

Array layout

Figure 4.18 is a histogram of resonant frequencies on this array. The frequency bunching effect is visible in the 16 peaks in the histogram, corresponding to the 16 unit cells.

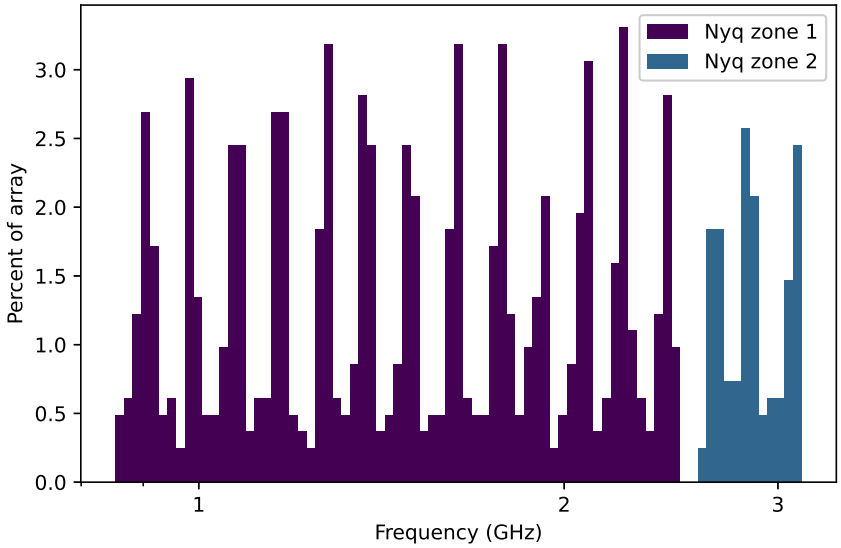

Figure 4.18: Histogram of resonant frequencies, separated by Nyquist zone.

The plots in Figure 4.19 are histograms of Q_c and Q_i. Both quality factors do not have a significant dependence on resonant frequency. The median quality factors are $Q_c = 18,000$ and $Q_i = 390,000$. The values are consistent with the 6x6 Π-shaped absorber array measured in Subsection 4.5.3.

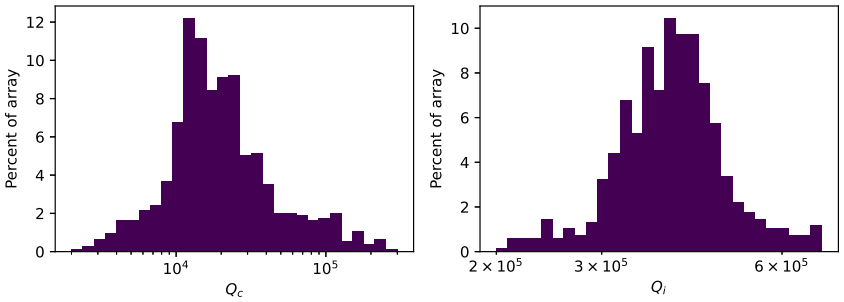

Figure 4.19: Histograms of the internal and coupling quality factors.

S_{21} versus frequency was measured for each resonator for 10 temperatures between 10 mK and 350 mK, though there is uncertainty at the lowest temperatures because the thermometer is mounted on the detector housing package, which may cool to lower temperatures than the array. The frequency shift was fit to Equation 2.44 to obtain T_c. The response due to TLSs is negligible compared to the response due to QPs over this temperature range. Reliable results were obtained for 783 resonators, where resonators were rejected due to poor resonance fits or poor fits to Equation 2.44. Figure 4.20 is histogram of T_c. The median value of T_c is 1.17 K.

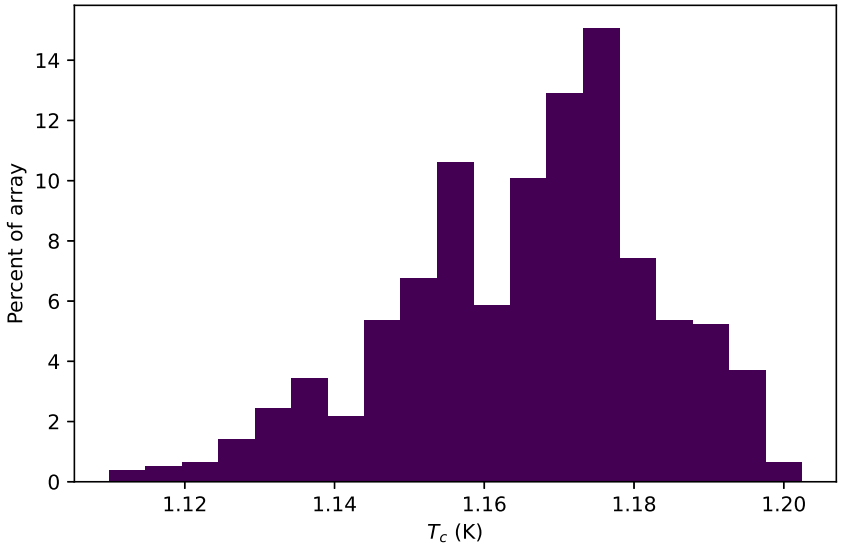

Figure 4.20: Histogram of T_c for 783 resonators.

Noise measurements

Noise was measured at 50 mK for the 766 resonators that passed the cuts discussed above. This array was not tested with the blackbody, so responsivities are not

measured. A histogram of S_{xx} at 10 Hz is presented in Figure 4.21. The spread in S_{xx} is roughly consistent with the long-wavelength datasets presented above. The histograms are plotted before and after removing correlated noise via the procedure in Appendix D. Note that the correlated noise in the off-resonance tones is removed from both datasets, since this algorithm is run on the complex S_{21} data before converting to x. Assuming the mean value of the responsivity for the arrays measured in Subsection 4.5.3, an NEP of 1×10^{-19} W/$\sqrt{\text{Hz}}$ corresponds to an S_{xx} of $\sim 1 \times 10^{-16}$ 1/Hz, suggesting that this device comfortably meets the FIRESS NEP requirement. The successful tuning of 766 KIDs combined with the successful measurement of T_c of 783 KIDs suggests that these procedures are capable of reading out enough pixels simultaneously to fully satisfy the FIRESS requirements, with expected future progress on array frequency scheduling and manual tuning techniques.

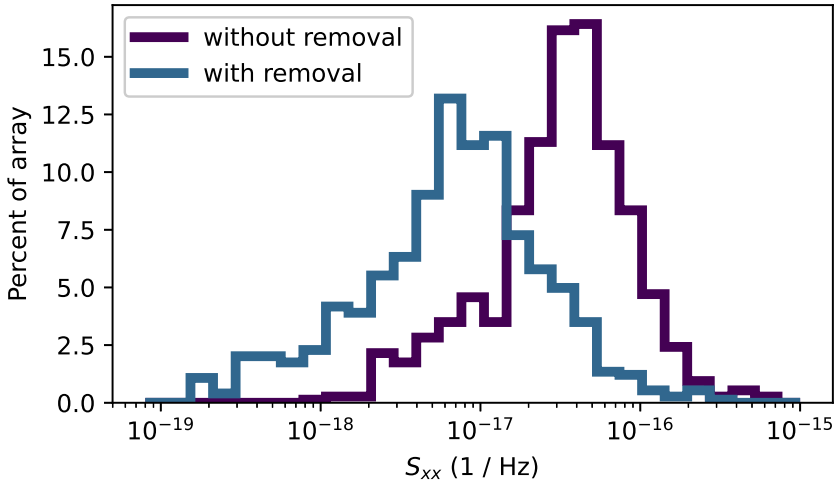

Figure 4.21: Histogram of S_{xx} at 50 mK, before and after removing correlated noise.

Correlated noise

The FIRESS detectors exhibit large correlated noise when read out with multi-tone readout. The noise is present on a variety of arrays including those presented in Subsections 4.5.2, 4.5.3, and in this subsection. The correlated noise is present in both the Prime-Cam system and the CRS, and it is generally greater in multi-tone measurements compared to single-tone measurements. This level of correlated noise is not present when measuring TIM arrays with the Prime-Cam system. The correlated noise is quantified by the Pearson correlation coefficient R_{ij}. The timestreams are first filtered to the readout frequency range of interest before calculating R_{ij}. Figure

4.22 is a plot of the correlation coefficient for the array presented in this subsection. The timestream was 60 s long, so the correlation coefficient is calculated for the 10-30 Hz band. Longer timestreams will be required to accurately measure correlated noise at lower readout frequencies. The timestream measurement was performed separately for each of the numerically controlled oscillator (NCO) frequencies, due to a limitation in the early CRS firmware that has since been overcome. The correlation matrix is therefore calculated separately for each of the NCO bands. Figure 4.22 includes R_{ij} in the 10-30 Hz band with and without the correlated noise removal algorithm from Appendix D applied. The correlated noise removal algorithm removes the majority of the correlated noise.

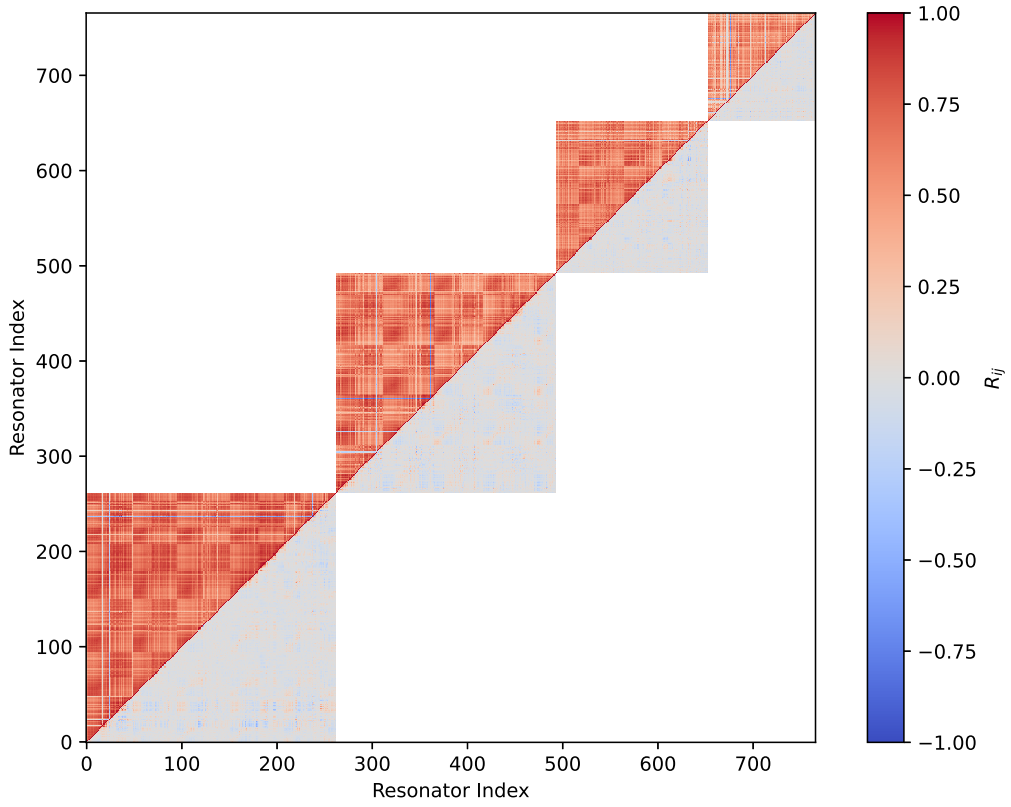

Figure 4.22: Correlation coefficient matrix at readout frequencies of 10-30 Hz. The upper left half of each band corresponds to the data without correlated noise removal, and the lower right half corresponds to the data after correlated noise removal.

The off-resonance correlated signal is mostly contained in the first 3–5 modes. Figure 4.23 contains plots PSDs of amplitude and phase components of the off-resonance common noise for the first 4 modes. The correlated phase noise contains a large 1/f component and small pulse-tube pickup components. The majority of the

correlated signal is contained in the first common mode. In the amplitude direction, the first common mode contains a 1/f component with a shallower slope than the phase direction. The spike at $\sim$ 10 Hz in the second mode is anomalous and of unknown origin.

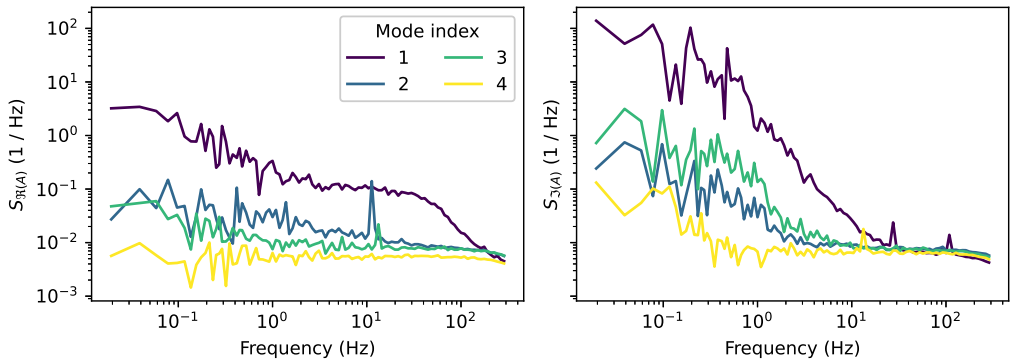

Figure 4.23: PSDs of the real (left) and imaginary (right) part of the first four common modes in the off-resonance data. The data is rotated via Appendix D such that the real signal corresponds to amplitude noise and the imaginary signal corresponds phase noise. The PSDs are averaged over the four NCO bands.

After subtracting the correlated off-resonance noise and converting the timestreams to fractional frequency shift, the on-resonance correlated noise is calculated. Figure 4.24 is a plot of the PSD of the on-resonance correlated noise. The correlated noise consists of a 1/f component and pulse tube spikes, which are spread throughout the first three or four modes.

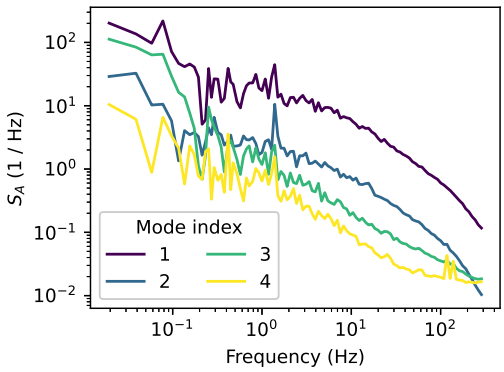

Figure 4.24: PSD of the first four common modes in the on-resonance data. The PSDs are averaged over the four NCO bands.

The correlated 1/f noise and pulse tube spikes are consistent features of the correlated noise in our arrays (e.g. Figure 4.12). 60 Hz pickup is rarely seen in our

measurements. The pulse tube pickup is highly correlated to packaging: arrays that are mounted with loose GE varnish or clips experience the most pulse tube pickup. In an initial test of the FIRESS flight-like mounting scheme, which uses flexures instead of GE varnish or clips, no pulse tube pickup was observed. The correlated 1/f noise, however, is observed in all multitone measurements, with both the Prime-Cam system and the CRS.

The "plaid" structure in the correlated noise is consistent with independent correlated components on the left and right half of the array. This array was mounted with clips on either end and a single GE varnish connection in the center, so this correlation may be dominated by vibrational pickup that is different on either half of the array.

The CPW feedline can support both odd and even modes, with the odd mode leading to an increase in correlated noise and a greater spread in Q_c for this array layout, because KIDs are located on either side of the feedline.[15] Suppression of the odd mode can be achieved by adding bridges across the feedline between resonators, and has been shown to control scatter in Q_c and significantly reduce correlated noise.[39] The current FIRESS layout does not have bridges across the feedline, so we hypothesize that some of the correlated noise arises in these asymmetric groundplane currents.

Given the high level of correlated noise and the short timestream lengths (60 s) used for this measurement, nearby frequency crosstalk cannot be measured with this dataset. The next array design includes at least one bridge across the feedline between every 4 KIDs. More bridges will be implemented if possible. Based on the successful reduction of correlated noise on similar devices,[39] this redesign is expected to significantly reduce correlated noise on our arrays. Because the pulse-tube pickup is correlated to packaging, we expect a further reduction in correlated noise by switching to the FIRESS flight-like mounting scheme. With these changes to the array design and packaging, and with longer timestreams measurements, the correlated noise should be reduced far enough to measure nearby frequency crosstalk. Spatial mapping of the array using the LED mapping setup will be required to measure spatial crosstalk.

References

[1] Chris Albert et al. “Spatial mapping of kilopixel kinetic inductance detector arrays for PRIMA”. In: *Millimeter, Submillimeter, and Far-Infrared Detectors and Instrumentation for Astronomy XII*. Vol. 13102. SPIE, Aug.

2024, pp. 631–637. DOI: 10.1117/12.3020503. URL: https://www.spiedigitallibrary.org/conference-proceedings-of-spie/13102/131021N/Spatial-mapping-of-kilopixel-kinetic-inductance-detector-arrays-for-PRIMA/10.1117/12.3020503.full (visited on 01/06/2025).

[2] Rami Barends et al. "Enhancement of quasiparticle recombination in Ta and Al superconductors by implantation of magnetic and nonmagnetic atoms". In: *Physical Review B* 79.2 (Jan. 2009). Publisher: American Physical Society, p. 020509. DOI: 10.1103/PhysRevB.79.020509. URL: https://link.aps.org/doi/10.1103/PhysRevB.79.020509 (visited on 10/01/2023).

[3] Jochem J. A. Baselmans et al. "Ultra-sensitive THz microwave kinetic inductance detectors for future space telescopes". In: *Astronomy and Astrophysics* 665 (Sept. 2022). ADS Bibcode: 2022A&A...665A..17B, A17. ISSN: 0004-6361. DOI: 10.1051/0004-6361/202243840. URL: https://ui.adsabs.harvard.edu/abs/2022A&A...665A..17B (visited on 09/14/2023).

[4] Jochem J. A. Baselmans et al. "Ultra-sensitive THz microwave kinetic inductance detectors for future space telescopes". In: *Astronomy and Astrophysics* 665, A17 (Sept. 2022), A17. DOI: 10.1051/0004-6361/202243840. arXiv: 2207.08647 [astro-ph.IM].

[5] Charles M. Bradford et al. "FIRESS: Unlocking Sensitive Far-IR Spectroscopy with PRIMA". In: *American Astronomical Society Meeting Abstracts*. Vol. 243. American Astronomical Society Meeting Abstracts. Feb. 2024, 457.11, p. 457.11.

[6] Charles Matt Bradford et al. "Origins Survey Spectrometer: revealing the hearts of distant galaxies and forming planetary systems with far-IR spectroscopy". In: *Journal of Astronomical Telescopes, Instruments, and Systems* 7.01 (Mar. 2021). ISSN: 2329-4124. DOI: 10.1117/1.JATIS.7.1.011017. URL: https://www.spiedigitallibrary.org/journals/Journal-of-Astronomical-Telescopes-Instruments-and-Systems/volume-7/issue-01/011017/Origins-Survey-Spectrometer--revealing-the-hearts-of-distant-galaxies/10.1117/1.JATIS.7.1.011017.full (visited on 05/04/2025).

[7] Juan Bueno et al. "Ultrasensitive Kilo-Pixel Imaging Array of Photon Noise-Limited Kinetic Inductance Detectors Over an Octave of Bandwidth for THz Astronomy". en. In: *Journal of Low Temperature Physics* 193.3 (Nov. 2018), pp. 96–102. ISSN: 1573-7357. DOI: 10.1007/s10909-018-1962-8. URL: https://doi.org/10.1007/s10909-018-1962-8 (visited on 10/25/2023).

[8] James Burgoyne. *primecam_readout*. original-date: 2022-01-17T17:02:02Z. Sept. 2023. URL: https://github.com/TheJabur/primecam%5C_readout (visited on 10/16/2023).

[9] James Burgoyne et al. “CCAT: FYST prime-cam readout software: a framework for massively scalable KID arrays”. In: *Software and Cyberinfrastructure for Astronomy VIII*. Ed. by Gianluca Chiozzi and Jorge Ibsen. Yokohama, Japan: SPIE, July 2024, p. 122. ISBN: 978-1-5106-7525-4 978-1-5106-7526-1. DOI: 10.1117/12.3019028. URL: https://www.spiedigitallibrary.org/conference-proceedings-of-spie/13101/3019028/CCAT--FYST-prime-cam-readout-software--a-framework/10.1117/12.3019028.full (visited on 04/02/2025).

[10] Nicholas F. Cothard et al. “Monolithic silicon microlens arrays for far-infrared astrophysics”. EN. In: *Applied Optics* 63.6 (Feb. 2024). Publisher: Optica Publishing Group, pp. 1481–1487. ISSN: 2155-3165. DOI: 10.1364/AO.510409. URL: https://opg.optica.org/ao/abstract.cfm?uri=ao-63-6-1481 (visited on 05/29/2024).

[11] Nicholas F. Cothard et al. “Parallel Plate Capacitor Aluminum KIDs for Future Far-Infrared Space-Based Observatories”. en. In: *Journal of Low Temperature Physics* 214.3-4 (Feb. 2024), pp. 200–209. ISSN: 0022-2291, 1573-7357. DOI: 10.1007/s10909-023-03039-0. URL: https://link.springer.com/10.1007/s10909-023-03039-0 (visited on 04/16/2025).

[12] Peter K. Day et al. “A 25-micrometer Single-Photon-Sensitive Kinetic Inductance Detector”. In: *Physical Review X* 14.4 (Oct. 2024). Publisher: American Physical Society, p. 041005. DOI: 10.1103/PhysRevX.14.041005. URL: https://link.aps.org/doi/10.1103/PhysRevX.14.041005 (visited on 11/02/2024).

[13] Fabien Defrance et al. “Characterization of the low electric field and zero-temperature two-level-system loss in hydrogenated amorphous silicon”. en. In: *Physical Review Materials* 8.3 (Mar. 2024), p. 035602. ISSN: 2475-9953. DOI: 10.1103/PhysRevMaterials.8.035602. URL: https://link.aps.org/doi/10.1103/PhysRevMaterials.8.035602 (visited on 04/26/2025).

[14] Pierre M. Echternach et al. “Single photon detection of 1.5 THz radiation with the quantum capacitance detector”. In: *Nature Astronomy* 2 (Nov. 2018), pp. 90–97. DOI: 10.1038/s41550-017-0294-y.

[15] Lorenza Ferrari et al. “Kinetic inductance detectors (KIDs) for the SAFARI instrument on SPICA”. In: ed. by Jacobus M. Oschmann Jr., Mark C. Clampin, and Howard A. MacEwen. San Diego, California, USA, July 2010, 77314H. DOI: 10.1117/12.868529. URL: http://proceedings.spiedigitallibrary.org/proceeding.aspx?doi=10.1117/12.868529 (visited on 05/16/2025).

[16] Logan Foote. *citkid*. original-date: 2024-03-01T17:58:06Z. Feb. 2025. URL: https://github.com/loganfoote/citkid (visited on 04/02/2025).

[17] Logan Foote. *High-sensitivity Kinetic Inductance Detector Arrays for the Probe Far-Infrared Mission for Astrophysics*. Poster presented at the 20th International Conference on Low Temperature Detectors. Daejon, South Korea, July 2023.

[18] Logan Foote et al. "High-Sensitivity Kinetic Inductance Detector Arrays for the Probe Far-Infrared Mission for Astrophysics". en. In: *Journal of Low Temperature Physics* 214.3-4 (Feb. 2024), pp. 219–229. ISSN: 0022-2291, 1573-7357. DOI: 10.1007/s10909-023-03041-6. URL: https://link.springer.com/10.1007/s10909-023-03041-6 (visited on 04/12/2024).

[19] Logan Foote et al. "Highly sensitive far-IR KIDs for PRIMA: optical characterization of a 25-micron array". In: *Millimeter, Submillimeter, and Far-Infrared Detectors and Instrumentation for Astronomy XII*. Ed. by Jonas Zmuidzinas and Jian-Rong Gao. Yokohama, Japan: SPIE, Aug. 2024, p. 27. ISBN: 978-1-5106-7527-8 978-1-5106-7528-5. DOI: 10.1117/12.3020228. URL: https://www.spiedigitallibrary.org/conference-proceedings-of-spie/13102/3020228/Highly-sensitive-far-IR-KIDs-for-PRIMA--optical-characterization/10.1117/12.3020228.full (visited on 04/15/2025).

[20] Adalyn Fyhrie et al. "Responsivity boosting in FIR TiN LEKIDs using phonon recycling: simulations and array design". In: 9914 (July 2016). Conference Name: Millimeter, Submillimeter, and Far-Infrared Detectors and Instrumentation for Astronomy VIII ADS Bibcode: 2016SPIE.9914E..2BF, 99142B. DOI: 10.1117/12.2231476. URL: https://ui.adsabs.harvard.edu/abs/2016SPIE.9914E..2BF (visited on 01/14/2025).

[21] Steven Hailey-Dunsheath et al. "Characterization of a Far-Infrared Kinetic Inductance Detector Prototype for PRIMA". In: *arXiv e-prints*, arXiv:2311.03586 (Nov. 2023), arXiv:2311.03586. DOI: 10.48550/arXiv.2311.03586. arXiv: 2311.03586 [astro-ph.IM].

[22] Steven Hailey-Dunsheath et al. "Characterization of a Far-Infrared Kinetic Inductance Detector Prototype for PRIMA". In: *IEEE Transactions on Terahertz Science and Technology* (2025), pp. 1–12. ISSN: 2156-342X, 2156-3446. DOI: 10.1109/TTHZ.2024.3454436. URL: https://ieeexplore.ieee.org/document/10999059/ (visited on 05/14/2025).

[23] Reinier M. J. Janssen et al. "High optical efficiency and photon noise limited sensitivity of microwave kinetic inductance detectors using phase readout". In: *Applied Physics Letters* 103.20, 203503 (Nov. 2013), p. 203503. DOI: 10.1063/1.4829657. arXiv: 1311.2429 [physics.ins-det].

[24] Elijah Kane et al. "Development of an ultra-sensitive 210-micron array of KIDs for far-IR astronomy". In: *Millimeter, Submillimeter, and Far-Infrared Detectors and Instrumentation for Astronomy XII*. Vol. 13102. SPIE, Aug. 2024, pp. 601–607. DOI: 10.1117/12.3020346. URL: https://www.spiedigitallibrary.org/conference-proceedings-of-spie/131

02/131021K/Development-of-an-ultra-sensitive-210-micron-array-of-KIDs/10.1117/12.3020346.full (visited on 01/06/2025).

[25] Elijah Kane et al. "Modeling of Cosmic Rays and Near-IR Photons in Aluminum KIDs". en. In: *Journal of Low Temperature Physics* 214.3-4 (Feb. 2024), pp. 238–246. ISSN: 0022-2291, 1573-7357. DOI: 10.1007/s10909-023-03044-3. URL: https://link.springer.com/10.1007/s10909-023-03044-3 (visited on 04/16/2025).

[26] Kenichi Karatsu et al. "Mitigation of cosmic ray effect on microwave kinetic inductance detector arrays". en. In: *Applied Physics Letters* 114.3 (Jan. 2019), p. 032601. ISSN: 0003-6951, 1077-3118. DOI: 10.1063/1.5052419. URL: https://pubs.aip.org/apl/article/114/3/032601/36747/Mitigation-of-cosmic-ray-effect-on-microwave (visited on 05/06/2025).

[27] Kirit S. Karkare et al. *Snowmass 2021 Cosmic Frontier White Paper: Cosmology with Millimeter-Wave Line Intensity Mapping*. Version Number: 1. 2022. DOI: 10.48550/ARXIV.2203.07258. URL: https://arxiv.org/abs/2203.07258 (visited on 05/04/2025).

[28] Alexander G. Kozorezov et al. "Quasiparticle-phonon downconversion in nonequilibrium superconductors". en. In: *Physical Review B* 61.17 (May 2000), pp. 11807–11819. ISSN: 0163-1829, 1095-3795. DOI: 10.1103/PhysRevB.61.11807. URL: https://link.aps.org/doi/10.1103/PhysRevB.61.11807 (visited on 05/04/2025).

[29] Lun-Jun Liu et al. "Cosmic Ray Susceptibility of the Terahertz Intensity Mapper Detector Arrays". en. In: *Journal of Low Temperature Physics* 216.1-2 (July 2024), pp. 195–207. ISSN: 0022-2291, 1573-7357. DOI: 10.1007/s10909-024-03123-z. URL: https://link.springer.com/10.1007/s10909-024-03123-z (visited on 04/19/2025).

[30] X. Liu et al. "Cryogenic LED pixel-to-frequency mapper for kinetic inductance detector arrays". en. In: *Journal of Applied Physics* 122.3 (July 2017), p. 034502. ISSN: 0021-8979, 1089-7550. DOI: 10.1063/1.4994170. URL: https://pubs.aip.org/jap/article/122/3/034502/154915/Cryogenic-LED-pixel-to-frequency-mapper-for (visited on 04/19/2025).

[31] X. Liu et al. "Superconducting micro-resonator arrays with ideal frequency spacing". In: *Applied Physics Letters* 111.25 (Dec. 2017), p. 252601. ISSN: 0003-6951, 1077-3118. DOI: 10.1063/1.5016190. URL: https://pubs.aip.org/apl/article/111/25/252601/904922/Superconducting-micro-resonator-arrays-with-ideal (visited on 10/27/2023).

[32] Daniel P. Marrone et al. "The terahertz intensity mapper: a balloon-borne imaging spectrometer for galaxy evolution". In: 12190 (Aug. 2022). Conference Name: Millimeter, Submillimeter, and Far-Infrared Detectors and Instrumentation for Astronomy XI ADS Bibcode: 2022SPIE12190E..08M,

p. 1219008. DOI: 10.1117/12.2630644. URL: https://ui.adsabs.harvard.edu/abs/2022SPIE12190E..08M (visited on 11/04/2024).

[33] Joshua Montgomery et al. "The CRS: a scalable full-stack control system for Microwave Kinetic Inductance Detectors". In: *Millimeter, Submillimeter, and Far-Infrared Detectors and Instrumentation for Astronomy XII*. Ed. by Jonas Zmuidzinas and Jian-Rong Gao. Yokohama, Japan: SPIE, Aug. 2024, p. 58. ISBN: 978-1-5106-7527-8 978-1-5106-7528-5. DOI: 10.1117/12.3019425. URL: https://www.spiedigitallibrary.org/conference-proceedings-of-spie/13102/3019425/The-CRS--a-scalable-full-stack-control-system-for/10.1117/12.3019425.full (visited on 04/02/2025).

[34] Aaron D. O'Connell et al. "Microwave dielectric loss at single photon energies and millikelvin temperatures". en. In: *Applied Physics Letters* 92.11 (Mar. 2008), p. 112903. ISSN: 0003-6951, 1077-3118. DOI: 10.1063/1.2898887. URL: https://pubs.aip.org/apl/article/92/11/112903/326064/Microwave-dielectric-loss-at-single-photon (visited on 04/26/2025).

[35] Matt Pyle et al. "Quasiparticle propagation in aluminum fins and tungsten TES dynamics in the CDMS ZIP detector". en. In: *Nuclear Instruments and Methods in Physics Research Section A: Accelerators, Spectrometers, Detectors and Associated Equipment* 559.2 (Apr. 2006), pp. 405–407. ISSN: 01689002. DOI: 10.1016/j.nima.2005.12.022. URL: https://linkinghub.elsevier.com/retrieve/pii/S0168900205024137 (visited on 07/28/2025).

[36] Jordan E. Shroyer et al. "A scalable cryogenic LED module for selectively illuminating kinetic inductance detector arrays". en. In: *Review of Scientific Instruments* 93.11 (Nov. 2022), p. 113107. ISSN: 0034-6748, 1089-7623. DOI: 10.1063/5.0103968. URL: https://pubs.aip.org/rsi/article/93/11/113107/2848890/A-scalable-cryogenic-LED-module-for-selectively (visited on 04/19/2025).

[37] Adrian Sinclair. *adriankaisinclair/primecam_gateware_design*. https://github.com/adriankaisinclair/prime cam_gateware_design. original-date: 2022-12-28T20:39:38Z. Jan. 2023. URL: https://github.com/adriankaisinclair/primecam%5C_gateware%5C_design (visited on 10/16/2023).

[38] Eve M. Vavagiakis et al. "CCAT-prime: design of the Mod-Cam receiver and 280 GHz MKID instrument module". In: *Millimeter, Submillimeter, and Far-Infrared Detectors and Instrumentation for Astronomy XI*. Ed. by Jonas Zmuidzinas and Jian-Rong Gao. Montréal, Canada: SPIE, Aug. 2022, p. 4. ISBN: 978-1-5106-5361-0 978-1-5106-5362-7. DOI: 10.1117/12.2630115. URL: https://www.spiedigitallibrary.org/conference-proceedings-of-spie/12190/2630115/CCAT-prime--design-of-the-

Mod-Cam-receiver-and/10.1117/12.2630115.full (visited on 04/19/2025).

[39] Stephen J. C. Yates et al. “Clean Beam Patterns with Low Crosstalk Using 850 GHz Microwave Kinetic Inductance Detectors”. en. In: *Journal of Low Temperature Physics* 176.5 (Sept. 2014), pp. 761–766. ISSN: 1573-7357. DOI: 10.1007/s10909-013-1034-z. URL: https://doi.org/10.1007/s10909-013-1034-z (visited on 12/04/2024).

[40] Nicholas Zobrist et al. “Membraneless Phonon Trapping and Resolution Enhancement in Optical Microwave Kinetic Inductance Detectors”. In: *Physical Review Letters* 129.1 (July 2022). Publisher: American Physical Society, p. 017701. DOI: 10.1103/PhysRevLett.129.017701. URL: https://link.aps.org/doi/10.1103/PhysRevLett.129.017701 (visited on 01/14/2025).

Chapter 5

SUMMARY AND DISCUSSION

The far-IR is a notoriously difficult portion of the electromagnetic spectrum to observe, yet it offers enormous discovery potential due to the orders-of-magnitude lower dust obscuration compared to shorter wavelengths. Earth's atmosphere provides significant emission and absorption in the far-IR, so observations must be performed from a space platform. Blackbody thermal emission at temperatures between 4 and 300 K peaks in the far-IR, so the full optical path of an instrument must be cooled to < 4 K. To take advantage of the low background provided by a 4 K telescope in space, high-sensitivity detectors are required. Furthermore, these detectors must have a high multiplex factor and low hardware complexity to be deployed in sufficient numbers in space. Large arrays of high-sensitivity far-IR detectors have therefore been a long sought-after goal for astrophysicists.

Several milestones for far-IR detector development were reached in the last few years. The preceding decade saw significant development of far-IR TESs. Following recent successes, KIDs have emerged as the leading technology for far-IR space missions. In Chapter 3, the culmination of JPL and Caltech's contribution to far-IR TES work is described. KIDs are the clear path forward for far-IR astrophysics space missions, with sufficient demonstrations now in place to build confidence that they will satisfy all the requirements for far-IR space spectroscopy. High-sensitivity KID designs that cover the full far-IR band are discussed in Section 4.2. Challenges that were overcome to achieve high-sensitivity are discussed in Section 4.3. Measurements of the long- and short-wavelength limits of the far-IR band are presented in Sections 4.5. These detectors meet the following detector requirements: (1) $\mathrm{NEP}^{0}_{\mathrm{abs}}$, the detector sensitivity with $P_{\mathrm{abs}} = 0$. (2) P_{max}, the saturation power. (3) τ, the detector time constant. (4) ν_{min}, the minimum readout frequency at which the NEP requirement is met. (5) ϵ_{CR}, the cosmic ray temporal efficiency. These requirements were satisfied on array formats (~1,000 pixels per array) that are sufficient for probe class space missions. The remaining requirement to demonstrate is the measurement yield of ~ 870 / 1,000 pixels. In Subsection 4.5.4, a measurement yield of 766 is achieved through the use of the automated tuning algorithm discussed in Appendix E combined with manual tuning, and it is argued that expected future progress on tuning and array frequency scheduling will increase the measurement yield to satisfy

the requirement.

Though these arrays have satisfied the minimum requirements for far-IR spectroscopy in space, some engineering challenges remain. The following are the most significant challenges PRIMA is facing.

1. LED mapping is a crucial step of the FIRESS detector characterization. One array has been successfully mapped with an initial mapping setup, and a new setup that re-images the LED array onto the detectors is in development. The LED mapping process must be consistently successful and standardized for the PRIMA detector development plan.

2. Improvements to frequency scheduling will increase the measurement yield, and improve the overall ease of measurement. Current plans involve changing the placement of arrays on the wafer and reorganizing the unit cell design to reduce bunching.

3. In addition to frequency scheduling improvements, laser trimming of capacitors could be used to separate overlapping resonators. Initial tests of the laser trimming process have been completed at JPL, but future work is necessary to demonstrate that this procedure will be successful for our devices.

4. Models and measurements of similar detectors suggest that we can achieve the crosstalk requirement for FIRESS with the addition of bridges across the feedlines, but this has not yet been demonstrated for our arrays. New arrays have been fabricated with bridges and testing is underway. This measurement will go hand-in-hand with NEP characterization, and should be performed with each dataset to track the crosstalk as array designs continue to develop.

5. The Al aging is a significant problem that must be controlled. Efforts are underway to further characterize this effect. Mitigation strategies will be tested to ensure that the aging can be kept under control during instrument assembly.

6. In order to achieve the measurement yield required for FIRESS, further development of the tuning algorithm is required. Proper frequency scheduling, successful laser trimming, and better control of quality factors (e.g. through the use of bridges across the feedline) will increase the measurement yield. The measurement of 766 resonators presented in Subsection 4.5.4 required

a significant time commitment for manual tuning, so improvements to the automated tuning code and manual tuning procedure will be helpful.

Looking forward, the next step for far-IR would be a flagship class space telescope with a ~6 m mirror and orders-of-magnitude more pixels (100,000–1,000,000), such as the Origins space telescope.[2] The photon-counting capabilities of these arrays would be of high interest for the faintest sources, but the sensitivity must be pushed even lower to detect individual photons at the long-wavelength end of the far-IR band. This sensitivity has been achieved in QCDs.[1] QCDs have two major limitations: the dynamic range is low and the accurate fabrication of large numbers of Josephson Junctions (JJ) is difficult. The first limitation may be overcome through the use of a QCD-KID hybrid, which is an active area of research. The JJ fabrication issue is also present in the field of superconducting quantum computing, where significant efforts are underway to improve the fabrication consistency of JJs. The investment in consistent JJ fabrication in the quantum computing field may provide advancements for QCD research.

The pixel count of 100,000-1,000,000 would require 100-1,000 coaxial lines with current multiplex factors and 100-1,000 readout channels, which is not practical in space. A new idea will be necessary to push far-IR detectors to these array sizes. A selling factor for KIDs has been that the fabrication and hardware complexity is simple, which is necessary in academic fabrication facilities. An analogous problem is faced by superconducting qubit researchers, who need to exponentially increase the number of qubits in a single cryostat to create a universal quantum computer. Several companies are attempting to solve this problem by increasing complexity on the chips to decrease the number of readout lines and the readout complexity (e.g. cat qubits). Far-IR detector researchers should follow this research closely, as the large-scale investment in quantum computing may prove to be fruitful for our field.

The work presented in this thesis is the culmination of decades of work by researchers at many institutions around the world. If PRIMA is selected as the next NASA probe mission, it will open up a new regime of astrophysics research, which will help unravel the story of how galaxies, stars, and habitable planets formed. The work presented in this thesis demonstrates that KIDs can satisfy the requirements for PRIMA, with expected future engineering efforts. With PRIMA's recent selection by NASA for a phase A study and exploration of new detector technologies in progress, an exciting new era of far-IR astrophysics is approaching!

References

[1] Pierre M. Echternach et al. “Large Array of Single-Photon Counting Quantum Capacitance Detectors”. en. In: *IEEE Transactions on Terahertz Science and Technology* 12.2 (Mar. 2022), pp. 211–216. ISSN: 2156-342X, 2156-3446. DOI: 10.1109/TTHZ.2021.3126542. URL: https://ieeexplore.ieee.org/document/9612726/ (visited on 10/25/2023).

[2] Margaret Meixner et al. *Origins Space Telescope Mission Concept Study Report*. 2019. DOI: 10.48550/ARXIV.1912.06213. URL: https://arxiv.org/abs/1912.06213.

Appendix A

TELESCOPE SENSITIVITY CALCULATION

Assuming the instrument noise is dominated by detector noise, the total noise equivalent power (NEP) of the instrument can be written as

$$\mathrm{NEP}^2_{\mathrm{total}} = \mathrm{NEP}^2_{\mathrm{photon}} + \mathrm{NEP}^2_{\mathrm{detector}}, \tag{A.1}$$

where $\mathrm{NEP}_{\mathrm{detector}}$ is detector noise and $\mathrm{NEP}_{\mathrm{photon}}$ is given in Equation 2.1. $\mathrm{NEP}_{\mathrm{detector}}$ can be treated as a constant in the low-loading limit. The number of modes is given by $N_{\mathrm{modes}} = N_{\mathrm{pol}} A\Omega/\lambda^2$, where N_{pol} is the number of polarizations, A is the telescope area and Ω is the solid angle on the sky that couples to each pixel. Assuming that the detector couples to a single spatial mode of radiation, such as a waveguide feed or a pixel with size $f\lambda$, $A\Omega = \lambda^2$, so $N_{\mathrm{modes}} = 2$ for two polarizations. The absorbed occupation number is the number of photons per mode per second per Hz of bandwidth, and can be expressed as $n = n_0\eta_{\mathrm{inst}}$, where η_{inst} is the instrument efficiency. The occupation number n_0 corresponding to the annual average background toward the north ecliptic pole, as viewed from an Earth-Sun L2 orbit, is derived from a sky model developed at the Infrared Processing and Analysis Center (IPAC) by Bill Reach and Bidushi Batticharya in 2006.[1] The minimum detectable flux MDF is given by

$$\mathrm{MDF} = \frac{\mathrm{SNR} \times \mathrm{NEP}_{\mathrm{total}}}{\sqrt{2t_{\mathrm{int}}}\eta_{\mathrm{inst}}\eta_{\mathrm{tel}} A \eta_{\mathrm{pixel}} \sqrt{\epsilon_{\mathrm{chop}}\epsilon_{\mathrm{CR}}}}, \tag{A.2}$$

where SNR is the desired signal-to-noise ratio, t_{int} is the integration time, η_{tel} is the telescope geometry and diffraction efficiency, and η_{pixel} is the pixel efficiency factor, which includes the effect of the Airy pattern and/or the spectral response function of the instrument. ϵ_{chop} is the temporal efficiency with which the chopping mirror maps the source onto a desired pixel for integration and ϵ_{CR} is the temporal efficiency remaining after cosmic ray strikes are excised from the data. The calculation for Figure 1.10 uses the parameter estimates given in Table A.1, corresponding to a typical 2 m space telescope with a spectral resolving power of 100.

Parameter	Description	Value
SNR	Signal-to-noise ratio	5
$\mathrm{NEP}_{\mathrm{detector}}$	Total NEP at Detector	1×10^{-19} W/$\sqrt{\mathrm{Hz}}$
t_{int}	Integration time	1 hr
η_{inst}	Instrument efficiency factor	0.17
η_{tel}	Telescope geometry and diffraction efficiency	0.79
η_{pixel}	Pixel efficiency	0.36
ϵ_{chop}	Chopping efficiency	0.88
ϵ_{CR}	Cosmic ray observing efficiency	0.9

Table A.1: Parameters for the MDF calculation for a 2 m telescope with a spectral resolving power of 100.

Appendix B

KINETIC INDUCTANCE DETECTOR RESONATORS

Figure 2.1 is a schematic of the Kinetic Inductance Detector (KID) resonant circuit. The resonator is represented by the impedance Z and the coupling capacitor is C_c. The resonator is typically an absorber (for which the impedance is derived in Section 2.4) in parallel with a capacitor. Sometimes, an additional capacitor to ground is included. The complex forward transmission S_{21} is measured from port 1 to port 2.

B.0.1 Basic Resonance Model

The basic formula for the transmission S_{21} through the resonant circuit is derived in many sources.[3,5,6] The transmission is

$$S_{21} = 1 - \frac{Q_r}{Q_c} \frac{1}{1 + 2jy}, \tag{B.1}$$

where Q_r is the total quality factor and Q_c is the coupling quality factor. The fractional spacing between the tone frequency f and the resonant frequency f_r is given by

$$x = \frac{f - f_r}{f_r}, \tag{B.2}$$

such that the number of line widths between the tone frequency and the resonant frequency is $y = Q_r x$. The total resonator quality factor is related to the coupling quality factor and the internal quality factor Q_i through

$$\frac{1}{Q_r} = \frac{1}{Q_c} + \frac{1}{Q_i}. \tag{B.3}$$

An example of the basic resonance model is plotted in Figure B.1.

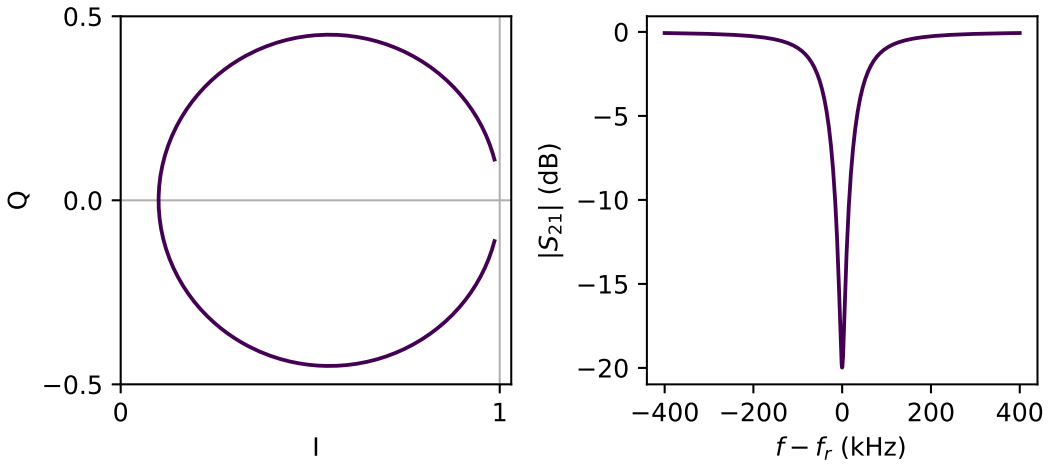

Figure B.1: Example of the basic resonance curve. (Left) imaginary (Q) versus real (I) component of the transmission. The resonance traces a circle with diameter Q_r/Q_c. (Right) transmission magnitude versus frequency. The resonance dip is centered on f_r and the FWHM is $\sqrt{3}f_r/Q_r$.

B.0.2 Impedance Mismatch

A mismatch in the impedance of the input and output lines can be modelled by introducing an imaginary component to the coupling quality factor through the angular parameter ϕ. The modification to the resonator transmission was calculated in Khalil et al. 2012.[4] The resonator transmission becomes

$$S_{21} = 1 - \frac{Q_r e^{j\phi}}{Q_c \cos\phi} \frac{1}{1 + 2jy}. \tag{B.4}$$

An example of the shift in the resonance caused by the impedance mismatch is plotted in Figure B.2.

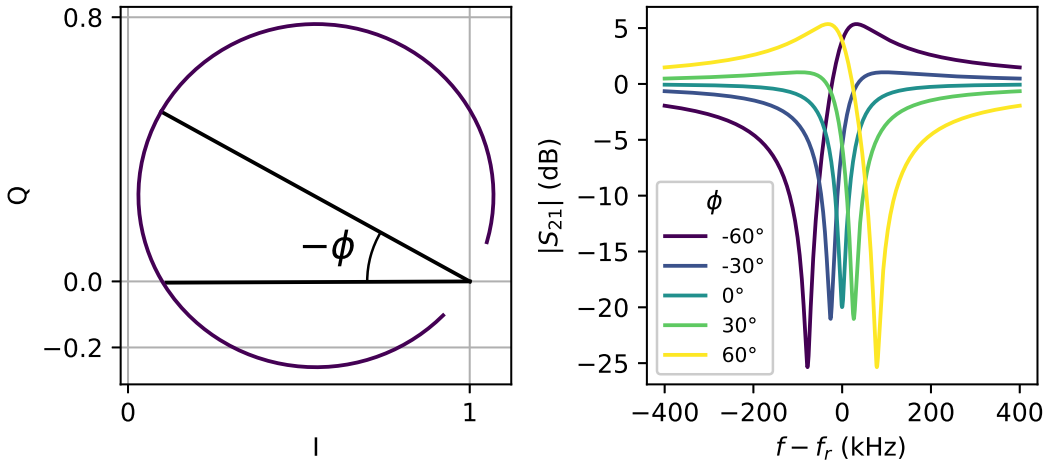

Figure B.2: Example of the shift in the resonance caused by an impedance mismatch. (Left) Q versus I. The angle ϕ determines the angle between the real axis and the location of the resonant frequency. (Right) transmission magnitude versus frequency for several values of ϕ.

B.0.3 Nonlinear Inductance

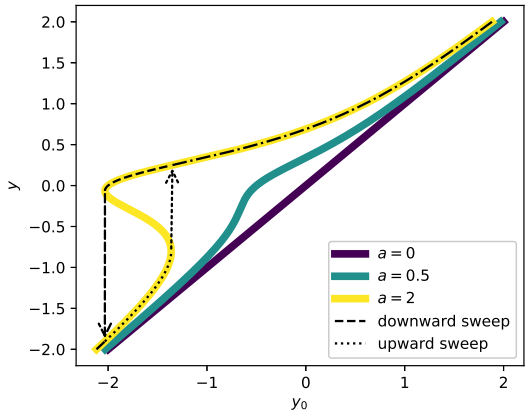

Figure B.3: y versus y_0, with paths drawn for upward and downward sweeps on the bifurcated curve.

The kinetic inductance is nonlinear, and microwave QP generation creates an additional nonlinearity. The nonlinear inductance can be modelled as the series

$$L(I) = L(I = 0)\left(1 + \frac{I^2}{I_2^2} + \cdots\right), \tag{B.5}$$

where odd powers of I vanish due to symmetry constraints and I_2 sets the scaling of the nonlinear effect. I_2 is on the order of the ratio of the inductive energy to the

pairing energy.[8] The modification to S_{21} due to the nonlinear inductance is derived in Swenson et al. 2013.[7] The power in the resonator will change as a tone with constant power is swept in frequency. This behavior manifests as a modification to y in Equation B.4, where y becomes the solution to

$$y - \frac{a_{\mathrm{nl}}}{1+4y^2} = y_0 = Q_r \frac{f - f_{r,0}}{f_{r,0}}, \tag{B.6}$$

where the nonlinearity parameter a_{nl} is given by

$$a_{\mathrm{nl}} = \frac{2Q_r^3}{Q_c} \frac{P_{\mu\mathrm{W}}}{2\pi f_r E_\star}, \tag{B.7}$$

where $P_{\mu\mathrm{W}}$ is the microwave power and $E_\star \propto L_k I_2^2/\alpha^2$, where $\alpha = L_k/L_{\mathrm{total}}$ is the kinetic inductance fraction. This equation can be solved for y, and it reaches a critical value at $a_{\mathrm{nl}}^{\mathrm{bif}} = 4\sqrt{3}/9 \approx 0.77$. For $a_{\mathrm{nl}} \leq a_{\mathrm{nl}}^{\mathrm{bif}}$, only one real solution exists for all values of y_0. For $a_{\mathrm{nl}} > a_{\mathrm{nl}}^{\mathrm{bif}}$, a range of y_0 values produce three real solutions. Two of these three solutions are stable (the largest and smallest stored energy states), so the resonator is said to have undergone bifurcation. Bifurcation is a hysteretic effect: as the probe tone is swept from low to high frequency the resonance is pulled towards the tone until it reaches the single-solution regime and quickly jumps to the left, or as the probe tone is swept from right to left the resonance is pushed away from the tone until they overlap and the resonance quickly jumps to the right. Figure B.3 is a plot of the value of y versus the value of y_0. y can be thought of as the spacing between the tone frequency and the actual resonant frequency, in number of line widths. Similarly, y_0 can be thought of as the spacing between the tone frequency and the resonant frequency with $P_{\mu\mathrm{W}} = 0$, in number of line widths.

This nonlinear behavior makes KID readout impractical above bifurcation. In practice, KIDs are typically read out around $a_{nl} = 0.5$, where the power is as high as reasonably possible to improve clearance above amplifier noise without reaching bifurcation. An example of the effect of the nonlinear kinetic inductance on the resonance shape is plotted in Figure B.4.

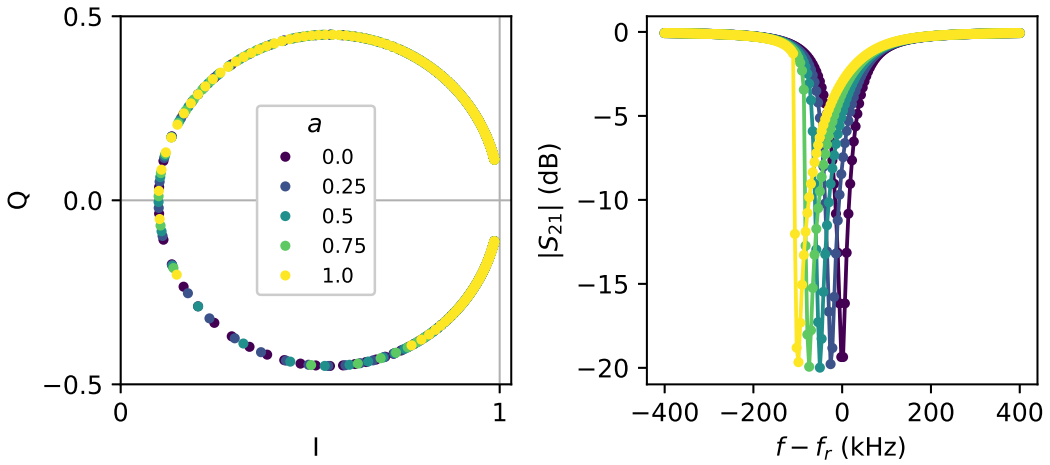

Figure B.4: Effect of the nonlinear kinetic inductance on resonance shape for a range of values of the nonlinearity parameter a_{nl}. (Left) Q versus I. (Right) transmission magnitude versus frequency.

B.0.4 Readout Circuit

The readout circuit gain can be written as

$$S_{21}^{\mathrm{readout}} = A(f)e^{-j2\pi f\tau_{\mathrm{cable}}+j\delta_0}, \tag{B.8}$$

where $A(f)$ is the frequency-dependent gain amplitude, τ_{cable} is the cable delay, and δ_0 is the phase offset.

B.1 Fitting

The resonance fitting routine is available in the `citkid` Python package,[2] which uses the Trust Region Reflective algorithm for fitting. Resonance data can be fit to the following equation:

$$S_{21} = A(f)e^{-j2\pi f\tau+j\delta}\left[1 - \frac{1}{1+2jy}\frac{Q_r}{Q_c\cos\phi}e^{j\phi}\right]. \tag{B.9}$$

In practice, the gain amplitude and phase are first removed from the data through polynomial fits to the data on either side of the resonance. A second-order polynomial fit is used for the gain amplitude, and a first-order fit is used for the gain phase (the cable delay and phase offset). After removing the gain amplitude and phase, the multiplicative complex parameter $z_0 = i_0 + jq_0$ and cable delay are kept in the

fitting equation for fine-tuning. The fitting equation is

$$S_{21} = (i_0 + jq_0)e^{-j2\pi f\tau}\left[1 - \frac{1}{1+2jy}\frac{Q_r}{Q_c\cos\phi}e^{j\phi}\right], \tag{B.10}$$

where the eight parameters to fit are

f_r : resonant frequency

Q_r : resonant quality factor

A : Q_r/Q_c

ϕ : impedance mismatch angle

a_{nl} : nonlinearity parameter

i_0 : real component of gain

q_0 : imaginary component of gain

τ : residual cable delay.

B.1.1 Guessing Function

Parameter	Lower range	Upper range
f_r	10 MHz	10 GHz
Q_r	10^3	10^6
A	10^{-3}	$1 - 10^{-5}$
ϕ	$-\pi/2$	$\pi/2$
a_{nl}	0	1
$i_0,\ q_0$	-10	10

Table B.1: Simulated resonance data parameter ranges.

Robust resonance fitting requires a parameter initial guess function that performs well over a wide range of parameters. To assess the capability of the non-linear fitting algorithm, 100,000 model resonances were generated and fit. The ranges of the model parameters used in the simulation are given in Table B.1. Gaussian noise was added to each data point with randomized amplitudes for each resonance. The resulting simulated data sets are of the form $\{f, z\}$, where f is the frequency data in Hz and z is the complex S_{21} data. From the resulting data, the parameter guessing function was created. The following procedures are used to determine the initial guess.

1. z_0: the mean of the two lowest frequency and two highest frequency points in the sweep.

2. τ: 0. The cable delay should be close to 0 if the gain phase is removed properly.

3. ϕ: the IQ data is fit to a circle, and the angle of the vector from z_0 to the center of the circle is the guess for ϕ (see Figure B.2 (left)).

4. A: the guess for A is given by $A = 2R|\cos(\phi)|/|z_0|$, where R is the radius from the circle fit.

5. Q_r: First, ϕ and A are removed from the data through a rotation and the absolute value is taken to get

$$|z_{\text{rot}}| = \left| \left(1 - \frac{z}{z_0}\right) \frac{e^{-j\phi}\cos\phi}{A} \right|. \tag{B.11}$$

   A Gaussian filter is applied to $|z_{\text{rot}}|$, and the full width at half maximum (FWHM) is extracted using a simple peak and width finding algorithm. The FWHM divided by the frequency of the peak is used to extract Q_r. A logarithmically-weighted linear fit to the logarithm of the Q_r and FWHM$/f_0$ data is performed to extract the Q_r guess, as plotted in Figure B.5 (left).

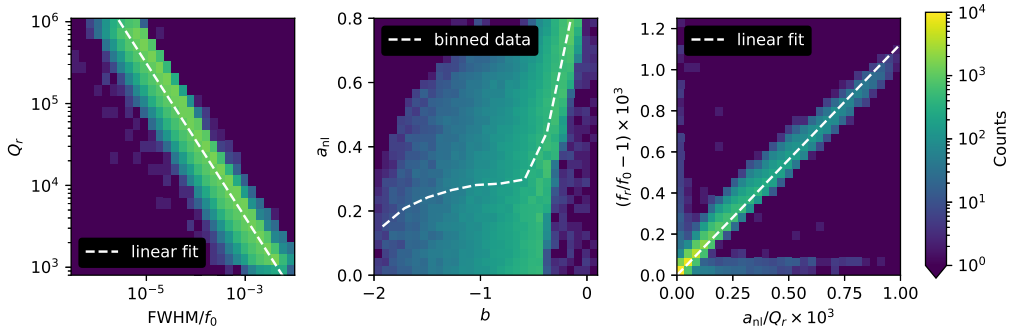

Figure B.5: (Left) Histogram of Q_r versus FWHM$/f_0$, where f_0 is the frequency at the peak. The linear fit is over-plotted. (Center): Histogram of a_{nl} versus b with binned data. (Right) Histogram of f_r versus a_{nl}/Q_r with linear fit.

6. a_{nl}: First, the data is rotated via Equation B.11. The quantity b is defined by

$$b = \left|\Delta z_{\text{rot}}^{\text{peak}}\right| \frac{f^{\text{peak}}}{\Delta f}, \tag{B.12}$$

where $\left|\Delta z_{\text{rot}}^{\text{peak}}\right|$ is the maximum spacing between adjacent points in IQ space, Δf is the frequency spacing (frequencies are assumed to be linearly spaced), and f^{peak} is the frequency corresponding to $\left|\Delta z_{\text{rot}}^{\text{peak}}\right|$. The resulting data is binned to create an array of data for interpolating from b to a_{nl}. a_{nl} versus b and the binned data are plotted in Figure B.5 (center). Resonators were generated up to $a_{\text{nl}} = 2$ and found to follow a near-vertical line with respect to b, so the upper cutoff of $a_{\text{nl}} = 1$ was chosen for the fitter.

7. f_r: f^{peak} is modified by a linear fit to f_r versus a/Q_r. The simulated data with a linear fit is plotted in Figure B.5 (right).

B.1.2 Bounds

The bounds for the fitting procedure are given in Table B.2.

Parameter	Lower bound	Upper bound
f_r	$\min f$	$\max f$
Q_r	$Q_r^{\text{guess}}/10$	$Q_r^{\text{guess}} \times 10$
A	10^{-3}	$1 - 10^{-6}$
ϕ	$-\pi/2$	$\pi/2$
a_{nl}	0	1
i_0	$i_0^{\text{guess}}/10$	$i_0^{\text{guess}} \times 10$
q_0	$q_0^{\text{guess}}/10$	$q_0^{\text{guess}} \times 10$
τ	-10^{-6}	10^{-6}

Table B.2: Bounds for the resonance fitting procedure, where f is the frequency data.

B.1.3 Evaluation of the Fit

The residuals from the fit to Equation B.10 are defined as

$$\text{res} = \frac{1}{N}\sqrt{\sum_i^N \left|z_i - z_i^{\text{fit}}\right|^2}, \tag{B.13}$$

where z_i is the data at index i, z_i^{fit} is the value of Equation B.10 at index i using the optimal fit parameters, and N is the total length of the data. Note that this definition of the residuals assumes that the gain is removed, and therefore (i_0, q_0) is close to

$(1, 0)$, such that the residuals of different datasets are comparable. Figure B.6 is a histogram of the residuals of fits to the simulated data. A threshold of 6×10^{-4} is defined to indicate poor fits.

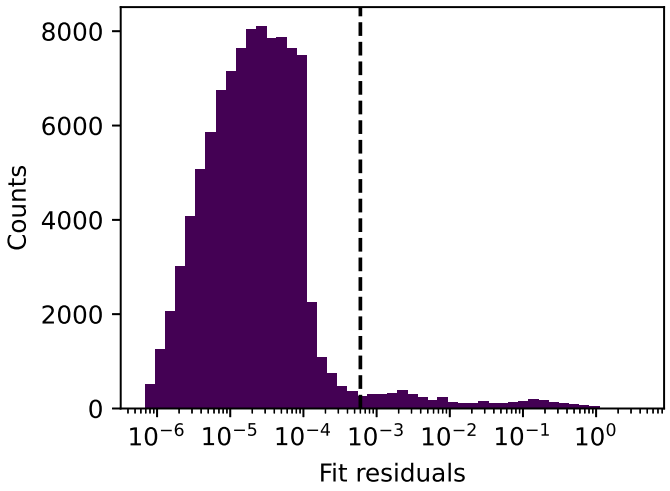

Figure B.6: Histogram of the residuals from fits to the simulated data. The median residual is 2×10^{-5}. The dashed black line indicates the threshold for poor fits.

A corner plot of the percentage of failed fits as a function of the five resonance fit parameters is plotted in Figure B.7. Overall, 95% of the fits were successful. Significant correlations between parameter values and failed fits are: $Q_r > 300,000$ (15% of failed fits), and $|\phi| > 0.9\pi/2$ (9% of failed fits). The remainder of the failed fits are distributed evenly throughout the parameter space.

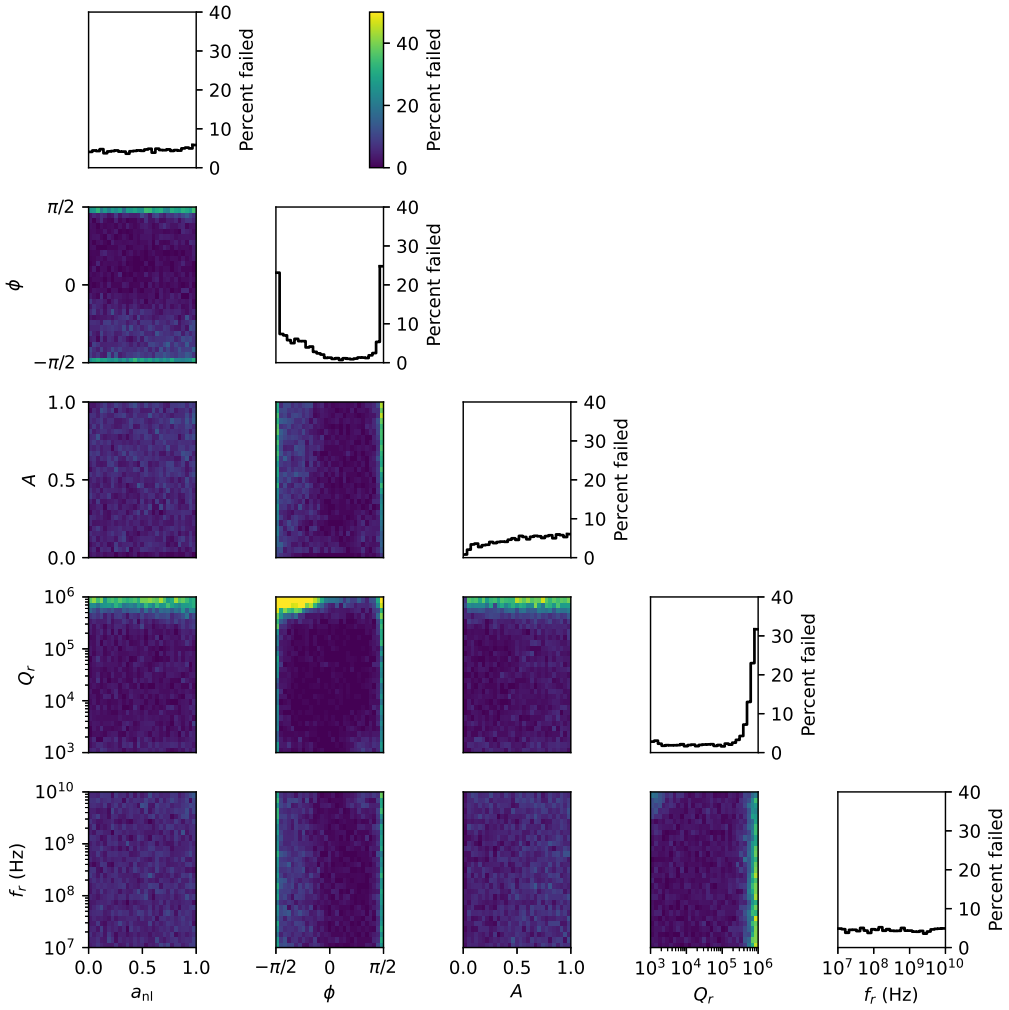

Figure B.7: Corner plot of failed fits versus parameter values. The histograms tally the percent of failed fits that fall into each bin.

Appendix C

FABRICATION OPTIMIZATION

In order to improve the fabrication reliability of the Al lift-off absorbers, the fabrication processes were optimized. The original fabrication process is labelled "A", and the optimized process is labelled "B". QP lifetimes of arrays using both processes are listed in Table 4.1. Two wafers were coated and baked for 5 minutes at 170C: one with MMA (8.5)/MAA (6) copolymer and the other with ZEP520A diluted 1:1 in anisole. The thickness of the copolymer was approximately 270 nm, while that of the ZEP520A was roughly 230 nm. Electron-beam lithography was used to pattern a series of squares with linearly increasing electron dose. After these wafers were written with e-beam, the ZEP520A wafer was developed in p-xylenes for 35 seconds, while the copolymer was developed in a mixture of MIBK:IPA of 1:3 for 2 minutes. Subsequently, the depth of the pattern for each dose was measured using a Dektak XT stylus profiler.

The depth versus dose for each material was then fed into Layout Beamer software by GenISys to determine the proper proximity effect correction (PEC) to write the desired absorber/inductor patterns. The proximity correction module used was called 3D E-beam Edge PEC. A legacy model of calculating the PEC (the Threshold Model), as well as a newer PEC calculation (the Development Rate Model) were both output. The legacy method was more reliable.

A test wafer was then coated with the copolymer prepared as above followed by the ZEP520A prepared as above to make a bilayer stack. A dose array near the optimal dose and PEC was written using e-beam, and the bilayer was developed using p-xylenes as above followed by MIBK:IPA as above. Al was then e-beam deposited and the optimal dose was chosen to be the one that produced the width of Al wire closest to the as-designed width and with the cleanest edges, as imaged in an SEM. The actual widths that were written were larger than the nominal width of 200 nm. A subsequent e-beam dose test was then run with an offset factored into the e-beam written pattern to yield the desired 200 nm wide Al wire feature sizes.

The PEC corrections and dose testing led to more reliable absorber writes for subsequent die fabrication. The optimal dose drifts over time, so the width of the wires is measured using SEM for each fabricated die and subsequent wafers are

adjusted accordingly. This optimized fabrication process yields devices with ~1 ms QP lifetimes. Our hypothesis for this increase in QP lifetime is that some portion of process A introduced non-uniformities into the Al which are not present in process B.

Appendix D

CORRELATED NOISE REMOVAL ALGORITHM

Start with a set of N timestreams of length T labelled x_{kt}, where k is the timestream index and t is the time index. Suppose each timestream can be written as

$$x_{kt} = \sum_c a_{kc} A_{ct} + n_{kt}, \tag{D.1}$$

where n_{kt} are the uncorrelated white timestreams, A_{ct} are a set of C common mode timestreams with index c, and the weights a_{kc} provide the scaling from A_{ct} to x_{kt}. The correlated white noise has a correlation function

$$\langle n_{kt} n_{k't'} \rangle = \sigma_k^2 \delta_{kk'} \delta_{tt'}. \tag{D.2}$$

The likelihood function is given by

$$\mathcal{L}(A, a, \sigma | x) = \frac{1}{(2\pi)^{NT/2} \prod_{k=0}^{N-1} \sigma_k^T} \exp\left[- \sum_{k=0}^{N-1} \sum_{t=0}^{T-1} \frac{\left[x_{kt} - \sum_c a_{kc} A_{ct}\right]^2}{2\sigma_k^2} \right]. \tag{D.3}$$

Maximizing the log likelihood with respect to σ_k yields

$$\frac{\partial \ln \mathcal{L}}{\partial \sigma_k} = \sum_t \frac{\left[x_{kt} - \sum_c a_{kc} A_{ct}\right]^2}{\sigma_k^3} - \frac{T}{\sigma_k} = 0 \tag{D.4}$$

$$\sigma_k^2 = \frac{1}{T} \sum_t \left[x_{kt} - \sum_c a_{kc} A_{ct} \right]^2. \tag{D.5}$$

Maximizing the likelihood with respect to a_{kc} yields

$$\frac{\partial \ln \mathcal{L}}{\partial a_{kc}} = \sum_t \frac{\left[x_{kt} - a_{kc} A_{ct}\right] A_{ct}}{\sigma_k^2} = 0 \tag{D.6}$$

$$a_{kc} = \left[\sum_t A_{ct}^2 \right]^{-1} \sum_t A_{ct} x_{kt}. \tag{D.7}$$

Maximizing the likelihood with respect to A_{ct} yields

$$\frac{\partial \ln \mathcal{L}}{\partial A_{ct}} = \sum_k \frac{\left[x_{kt} - a_{kc} A_{ct}\right] a_{kc}}{\sigma_k^2} = 0 \tag{D.8}$$

$$A_{ct} = \left[\sum_k \frac{a_{kc}^2}{\sigma_k^2} \right]^{-1} \sum_k \frac{x_{kt} a_{kc}}{\sigma_k^2}. \tag{D.9}$$

Substituting Equation D.9 into Equation D.7 yields

$$a_{kc} = \left[\sum_t \left(\sum_h \frac{x_{ht}a_{hc}}{\sigma_h^2}\right)^2\right]^{-1} \sum_g \left[\sum_t \frac{x_{kt}x_{gt}}{\sigma_g^2} a_{gc}\right] \tag{D.10}$$

$$\frac{a_{kc}}{\sigma_k} = \left[\sum_t \left(\sum_h \frac{x_{ht}a_{hc}}{\sigma_h^2}\right)^2\right]^{-1} \sum_g \left[\sum_t \frac{x_{kt}x_{gt}}{\sigma_g\sigma_k}\right] \frac{a_{gc}}{\sigma_g}. \tag{D.11}$$

Therefore, the vector

$$v_{kc} = \frac{a_{kc}}{\sigma_k} \tag{D.12}$$

is an eigenvalue of the matrix

$$C_{kg} = \sum_t \frac{x_{kt}x_{gt}}{\sigma_k\sigma_g}. \tag{D.13}$$

To determine v_{kc}, the matrix C_{kg} can be calculated and diagonalized. The C largest eigenvalues determine the vectors v_{kc} associated with the C largest common modes. A normalization condition is imposed on v_{kc} such that

$$\sum_k v_{kc} = \sum_k \frac{a_{kc}^2}{\sigma_k^2} = 1. \tag{D.14}$$

Equation D.9 then becomes

$$A_{ct} = \sum_k \frac{x_{kt}a_{kc}}{\sigma_k^2}. \tag{D.15}$$

The problem is now reduced to finding σ_k, which can be done iteratively. A practical implementation of the algorithm requires extra care for two reasons: (1) The derivations assume that the uncorrelated noise is white. For noise that is not white, a whitening algorithm can be applied. In the case of 1/f noise that reaches a white floor, a high-pass filter can be applied to the timestreams x_{kt} when calculating σ_k and a_{kc}, but not when calculating A_{ct}. (2) The algorithm will tend to drive a single value of σ_k to 0, thereby driving the weighting to infinity and finding A_{ct} that is equal to that timestream. To rectify this, a low-pass filter can be applied to A_{ct} to ensure that σ_k cannot be driven to zero. This method will fail to remove correlated noise above the filter cutoff.

In summary, the algorithm is:

1. Optionally apply a whitening filter or a high-pass filter to x_{kt} to get x'_{kt}.

2. Calculate the initial value for σ_k with

$$\sigma_k = \sum_t (x'_{kt})^2. \tag{D.16}$$

3. Calculate the matrix M with

$$M_{kg} = \sum_t \frac{x'_{kt} x'_{gt}}{\sigma_k \sigma_g}. \tag{D.17}$$

4. Find the eigenvectors v_{kc} corresponding to the C largest eigenvalues of M_{kg}, and normalize them to $v_{ck} v_{kc} = 1$.

5. Calculate the weights a_{kc} with

$$a_{kc} = \sigma_k v_{kc}. \tag{D.18}$$

6. Calculate the common timestreams A_{ct} with

$$A_{ct} = \sum_k \frac{x_{kt} a_{kc}}{\sigma_k^2}. \tag{D.19}$$

   Optionally apply a filter (low-pass or otherwise) to A_{ct} to get A'_{ct} in order to stabilize the algorithm.

7. Recalculate σ_k with

$$\sigma_k = \sum_t \left[x'_{kt} - \sum_c a_{kc} A'_{ct} \right]^2. \tag{D.20}$$

   If a whitening filter was constructed from x_{kt} and applied in Step 1, reconstruct the filter using $x_{kt} - \sum_c a_{kc} A'_{ct}$.

8. Return to Step 3 and iterate.

Steps 2–6 can be recognized as the standard principal component analysis (PCA) algorithm, weighted by σ_k. The algorithm deviates from the PCA in Step 1, where the whitening filter is applied, and in Steps 7-8, where σ_k is iteratively updated to ensure that it is not dominated by correlated noise. In practice, the algorithm typically converges in about five iterations.

The correlated noise removal algorithm can also be implemented to remove correlated noise from off-resonance tones or dark detectors (detectors that do not see

light). Suppose x_{kt} are the detector timestreams and y_{gt} are the separate timestreams for removal. For the case of off-resonance tones, the phase and amplitude directions of the complex timestreams can be treated separately. For the case of dark resonators, the timestreams are first converted to fractional frequency. The data may be grouped in resonant frequency bins before running the algorithm. The detector timestream can be written as

$$x_{kt} = \sum_c a_{kc} A_{ct} + x'_{kt}, \tag{D.21}$$

where now A_{ct} is found by running the above algorithm on y_{gt} and x'_{kt} are the detector timestreams after removing A_{ct}. The scaling factors a_{kc} are found by minimizing

$$\sum_t (x_{kt} - a_{kc} A_{ct})^2, \tag{D.22}$$

which yields

$$a_{kc} = \frac{\sum_t x_{kt} A_{ct}}{\sum_t [A_{ct}]^2}. \tag{D.23}$$

For datasets with off-resonance tones and dark resonators, the full procedure is as follows:

1. Calculate A_{ct} for the off-resonance tones in the phase and amplitude directions using the iterative procedure. Then, calculate a_{kc} using Equation D.23 and remove the correlated noise. Apply this correction to the optically-coupled and dark detectors.

2. Convert the data to fractional frequency timestreams. An offset may be required to ensure that the data falls on the IQ loop.

3. Calculate A_{ct} for the dark detectors using the iterative procedure. Then, calculate a_{kc} using Equation D.23 and remove the correlated noise from the optically-coupled detectors.

4. Calculate A_{ct} and a_{kc} for the optically-coupled detectors using the iterative procedure and remove the correlated noise.

If the dataset does not have dark detectors, skip Step 3. If the data has a correlated signal that must be maintained, skip Step 4 or filter A_{ct} in Step 4 to ensure that the signal will not be removed.

Appendix E

TUNING

Tuning a KID consists of choosing the optimal tone power $P_{\mu W}$ and frequency f_{tone} to minimize $\text{NEP}^0_{\text{abs}}$ while ensuring that the detector NEP will remain photon noise limited up to P_{max}. The tone power should be maximized to minimize the amplifier noise contribution S^{amp}_{xx}, because $S^{\text{amp}}_{xx} \propto 1/P_{\mu W}$ (see Equation 2.115). Bifurcation places an upper limit on the practical readout power. The Far-InfraRed Enhanced Survey Spectrometer (FIRESS) detectors have a relatively low bifurcation power (∼-110 dBm), narrowing the range of acceptable power significantly compared to our higher-volume devices. Due to the low bifurcation power, the measurements in this thesis use low-noise commercially-available High-Electron-Mobility Transistor amplifiers (HEMTs) (T_n ∼1.4 K).

A tone power corresponding to a nonlinearity parameter of ∼ 0.5 is typically targeted to approach, but not exceed, bifurcation. In the cases where the resonance cannot be fit to determine the nonlinearity parameter, manual intervention is required. The power is chosen manually by plotting the clearance over amplifier noise as a function of power and the S_{21} versus frequency data as a function of power, then choosing the power that maximizes the amplifier noise clearance without bifurcating. A more sophisticated algorithm could be developed to automate this procedure.

To aid in the understanding of frequency tuning, resonance were simulated with a variety of parameters and the amplifier contribution to the noise was calculated using Equation 2.115. Ignoring the microwave power contribution the quasiparticle (QP) density, S^{QP}_{xx} will remain the same regardless of bias power and frequency, so S^{amp}_{xx} is a direct probe of the amplifier contribution to the total noise. A simulated sweep over frequency of S_{21} is performed to obtain $\{f, z\}$, where f is the frequency data and z is the complex S_{21} data. From $\{f, z\}$, new bias frequencies were calculated using the following three methods:

1. minS21: the frequency corresponding to the minimum of $|z|$.
2. spacing: the frequency corresponding to the maximum of $|z_{i+1} - z_i|$.
3. distance: the frequency corresponding to the maximum of $|z - z_{\text{off}}|$, where

z_{off} is the off-resonance data point calculated from the mean of the first and last few points in z.

The ideal bias point is also determined for the simulated data by choosing the frequency corresponding to the minimum of S_{xx}^{amp}. The following was observed:

1. The spacing method always corresponds to the ideal bias point.
2. Changing Q_i or Q_c changes the overall level of the amplifier noise, but does not change any relevant behavior for tuning.
3. Increasing a_{nl} causes the minS21 method and the distance method to overestimate the ideal bias frequency, leading to a potentially orders-of-magnitude increase in the amplifier noise contribution.
4. Positive ϕ causes minS21 to overestimate the ideal bias frequency and negative ϕ causes minS21 to underestimate the bias frequency, leading to a potentially order-of-magnitude increase in the amplifier noise contribution.

Although the ideal bias frequency is found using the spacing method, this method is not robust to noisy data or glitches, which are often present when using the multi-tone systems. The majority of the multi-tone measurements presented in this thesis used the distance method, which was found to be more robust, while single-tone measurements primarily used the spacing method without issue: the single-tone systems are more robust to data glitches, and manual intervention is easy when measuring a single resonance. The multitone measurements presented in this thesis were performed with readout systems in the development stage. As the readout systems mature to improve data quality, the spacing method should be used to increase the measurement yield.

E.1 Tuning at High Absorbed Power

The tuning discussion thus far has focused on the lowest loadings. As the loading is increased, the resonant frequency will shift and the internal quality factor will degrade. For the simplest tuning scheme, the tone frequency and power are chosen at the lowest loading and remain static for every observation. At high loadings, the tone will be substantially detuned from the resonant frequency, but the photon noise will also be higher. Figure E.1 is a plot of the simulated QP noise and amplifier noise as a function of absorbed power at 100 µm, for nominal FIRESS KID parameters.

The amplifier noise is plotted for the static tone frequency and power case, and for the optimal tuning case (where the frequency and power are chosen perfectly for each P_{abs}). The amplifier noise becomes comparable to the QP noise at the highest loadings when the tone is kept static, while it remains two orders of magnitude below the QP noise when tuned optimally. A simple scheme where the tone is tuned to lower frequency than the resonant frequency with a sacrifice to low-loading amplifier noise is possible, but the effectiveness is limited. Therefore, some form of feedback will be necessary for FIRESS, though it may be as simple as changing the tone frequency to a new static placement before observing the brightest sources.

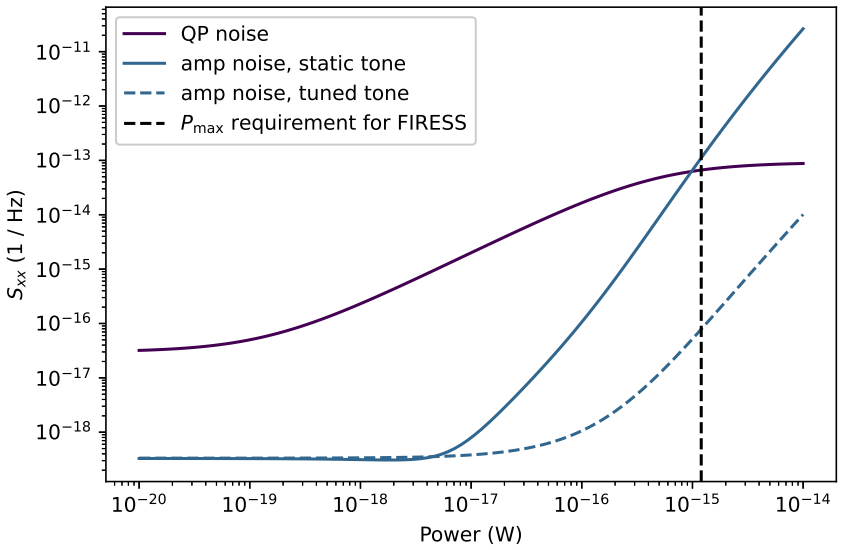

Figure E.1: QP noise and amplifier noise versus absorbed power for 110 µm light. The amplifier noise is given for both a static tone and an optimally tuned tone. The KID parameters used in this simulation are: $f_r(P_{\text{abs}} = 0) = 1$ GHz, $Q_c = 30{,}000$, $Q_i(P_{\text{abs}} = 0) = 400{,}000$, and $a_{\text{nl}}(P_{\text{abs}} = 0) = 0.5$.

References

[1] Charles Matt Bradford. *Annual average background toward the north ecliptic pole, as viewed from an Earth-Sun L2 orbit, deriving from a sky model developed at IPAC by Bill Reach and Bidushi Batticharya in 2006*. Personal Communication. Dec. 2024.

[2] Logan Foote. *citkid*. original-date: 2024-03-01T17:58:06Z. Feb. 2025. URL: https://github.com/loganfoote/citkid (visited on 04/02/2025).

[3] Jiansong Gao. "The Physics of Superconducting Microwave Resonators". en. phd. California Institute of Technology, 2008. DOI: 10.7907/RAT0-VM75.

URL: https://resolver.caltech.edu/CaltechETD:etd-06092008-235549 (visited on 12/02/2024).

[4] Moe S. Khalil et al. "An analysis method for asymmetric resonator transmission applied to superconducting devices". In: *Journal of Applied Physics* 111.5 (Mar. 2012), p. 054510. ISSN: 0021-8979. DOI: 10.1063/1.3692073. URL: https://doi.org/10.1063/1.3692073 (visited on 03/04/2024).

[5] Benjamin A. Mazin. "Microwave Kinetic Inductance Detectors". en. phd. California Institute of Technology, 2005. DOI: 10.7907/GZ72-V784. URL: https://resolver.caltech.edu/CaltechETD:etd-10042004-120707 (visited on 12/02/2024).

[6] Omid Noroozian. "Superconducting Microwave Resonator Arrays for Submillimeter / Far-infrared Imaging". en. phd. California Institute of Technology, 2012. DOI: 10.7907/8MG2-NB23. URL: https://resolver.caltech.edu/CaltechTHESIS:06122012-091920562 (visited on 12/02/2024).

[7] Loren J. Swenson et al. "Operation of a titanium nitride superconducting microresonator detector in the nonlinear regime". In: *Journal of Applied Physics* 113.10 (Mar. 2013), p. 104501. ISSN: 0021-8979. DOI: 10.1063/1.4794808. URL: https://doi.org/10.1063/1.4794808 (visited on 12/01/2024).

[8] Jonas Zmuidzinas. "Superconducting Microresonators: Physics and Applications". en. In: *Annual Review of Condensed Matter Physics* 3.1 (Mar. 2012), pp. 169–214. ISSN: 1947-5454, 1947-5462. DOI: 10.1146/annurev-conmatphys-020911-125022. URL: https://www.annualreviews.org/doi/10.1146/annurev-conmatphys-020911-125022 (visited on 09/06/2023).